



UNIVERSITY OF STRATHCLYDE

DOCTORAL THESIS

**Heterogeneous integration of diamond
with non-native substrates**

Author:

Paul HILL

Supervisors:

Dr. Michael STRAIN

& Dr. Erdan GU

*A thesis submitted in fulfillment of the requirements
for the degree of Doctor of Philosophy*

in the

**Integrated Optics Group
Institute of Photonics**

August 9, 2019

Declaration of Authorship

I, Paul HILL, declare that this thesis titled, "Heterogeneous integration of diamond with non-native substrates" and the work presented in it are my own. I confirm that:

- This thesis is the result of the author's original research. It has been composed by the author and has not been previously submitted for examination which has led to the award of a degree.
- The copyright of this thesis belongs to the author under the terms of the United Kingdom Copyright Acts as qualified by University of Strathclyde Regulation 3.50. Due acknowledgement must always be made of the use of any material contained in, or derived from, this thesis.

Signed:

Date:

“There are two types of PhD thesis: perfect, and submitted.”

Author Unknown

UNIVERSITY OF STRATHCLYDE

Abstract

Physics

Institute of Photonics

Doctor of Philosophy

Heterogeneous integration of diamond with non-native substrates

by Paul HILL

This thesis addresses the challenges with utilising diamond for integrated optical devices; a platform where its impressive material properties can be exploited. The major objective was to develop a process by which diamond could be heterogeneously integrated with non-native device platforms, to overcome its limited geometry. A process was developed for fabrication, handling, and hybrid integration of ultra thin diamond membranes. Plasma-etch chemistries were developed, that enabled such processing, and provided sub-nm r.m.s. roughness. Two sets of monolithic diamond structures were fabricated and transfer printed with a thickness down to ~ 10 nm. For thickness characterisation, diamond platelets, finding a low local-variation across typical device geometries. Diamond resonator devices were also fabricated and when integrated with SOI waveguides they showed high Q-factors as large as 1.8×10^5 . Thermo-optic tuning of these devices by > 450 pm at low mW powers was demonstrated, which has great significance to all integrated optical fields where resonant frequency of a cavity is important. The techniques developed are independent of integration platforms and are of wide reaching relevance to the optics community.

Acknowledgements

Doing a PhD has been one of the most rewarding experiences I have had and comes second only to parenthood in making me grow so much as a person. Part of what has made my PhD such a positive experience, is the help and interactions I have had with the people I need to thank here! I would firstly like to express my very great appreciation to Dr Michael Strain for his supervision, constructive suggestions, general support, and his generously spent time in helping me complete my PhD. It is without question something I will always value. The PhD would also not have been possible without the funding provided from EPSRC [EP/P013597/1], the National Quantum Information Technology Hub [EP/M013243/1], and Fraunhofer UK [EP/L015315/1].

I would also like to thank Dr Erdan Gu, my second supervisor, for all his help and support throughout my tenure - you provided great insight, thank you.

My research would have been much more difficult if not for the guidance and knowledge of several senior members of staff that I'd like to heartily thank here. Dr Ross Leyman, for your support and training with my now standard toolkit of diamond processing - thank you. Dr Benoit Guilhabert you have always been available for discussions on overcoming a wide range of research challenges. The scope of problems you have assisted me with speaks to the volume of your knowledge and experience - thank you for all of your help. Also dungeons and dragons!

I need to of course extend deep gratitude to James Sweeney whose expertise with each tool in the cleanroom has helped me often and greatly! Sharon Kelly and Lorraine Annand you have been a constant source of knowledge and support with so many of the problems researchers have to face every day and for that I would like to thank you both very much.

My PhD would not have been half as enjoyable without the peers I have completed it with. John McPhillimy thanks for lending an ear when I have had to vent and for giving me many a laugh throughout! I am very grateful we got to do our PhDs together. Dimitars Jevtics, thanks for the chess games! Dr Caroline Foucher, you were a source of much amusement and support - thank you! I would also like to thank you Dr Katherine Rae, I had a great time quizzing with you and basking in your trivia knowledge - you are truly impressive. Cruciverbalists!

Finally I would like to thank my family for all the support they have provided throughout my education and in general - I made it!

Contents

Declaration of Authorship	i
Abstract	iv
Acknowledgements	v
1 Single crystal diamond for integrated optical applications	1
1.1 Introduction	1
1.2 Background and Motivation	1
1.3 Synthesis of diamond	5
1.3.1 High pressure high temperature	5
1.3.2 Chemical vapour deposition	7
1.4 Integrated Optics	9
1.4.1 Background	9
1.4.2 Planar waveguide and resonator structures	9
1.5 Challenges to using diamond for integrated optics	13
1.5.1 Diamond-Silicon integrated optics	15
1.6 Current diamond technologies	16
1.6.1 Gallium Phosphide membranes on bulk diamond	16
1.6.2 Diamond patterned on insulator	18
1.6.3 Suspended uniform thickness diamond windows	20
1.6.4 Other works	21
1.7 Thesis outline	23

2	Ultra-thin diamond membrane fabrication & characterisation	25
2.1	Ultra-thin diamond membrane fabrication	27
2.1.1	Diamond etch chemistries	29
2.2	Diamond membrane handling	30
2.3	Thickness and surface morphology measurements	31
2.3.1	Vertical scanning interferometry and stylus profileometry	31
2.3.2	Atomic Force Microscopy	37
2.4	Results and Discussion	39
2.4.1	Diamond material sourcing and preparation	39
2.4.2	Global thinning and characterisation	40
3	Bonding of thin film diamond membranes to integrated optical devices for evanescent field coupling	44
3.1	Device design and simulation	45
3.1.1	Silicon resonator devices for hybrid integration with diamond	45
3.1.2	Simulation of modal confinement	48
3.1.3	1 μm Diamond Membranes	51
3.2	Liquid assisted bonding of diamond with Si devices	52
3.3	Measurements and characterisation	52
3.3.1	Deformation of the membrane	52
3.3.2	Optical probe measurements	56
3.3.3	Added losses	62
3.4	Discussion and Conclusion	64
4	Fabrication and micro-assembly of monolithic diamond optical resonators coupled to silicon-on-insulator waveguides	66
4.1	Motivation	67
4.2	Tessellated diamond membrane fabrication for thickness characterisation	68

4.2.1	Device design and transfer printing	68
4.2.2	Fabrication and thickness characterisation of ultra-thin diamond platelets	71
4.3	Diamond disk resonators heterogeneously integrated with a SOI platform	74
4.3.1	Device design, fabrication and motivation	74
4.3.2	One- and two- dimensional mode solving for design of diamond resonators	77
4.3.3	Optical transmission measurements of a hybrid diamond-silicon resonator	81
4.4	Conclusion	85
5	Thermally tuneable diamond micro-disk resonators	86
5.1	Introduction	86
5.2	Background and Theory	88
5.2.1	Optical bistability	88
5.2.2	Power enhancement in a micro-ring resonator	89
5.2.3	Power dependent shift in refractive index	90
5.3	Results	94
5.3.1	Low power thermal tuning	94
5.3.2	Demonstration of separable thermal tuning and cold cavity transmission sweeps	97
5.4	Conclusion	101
6	Conclusion and Outlook	102
6.1	Conclusion	102
6.2	Future Work	105
6.2.1	Hybridisation with visible-light transparent platforms for quantum applications	105

6.2.2	Photoluminescent measurement automation, alignment, and scalability	106
6.2.3	Efficient development of spin maintaining diamond etch processing	106
6.2.4	Grayscale photolithographic reduction of material wedge . . .	107
6.2.5	Final remark	108
	Bibliography	109
	List of Publications	131

List of Figures

1.1	A table showing the Mohs and Vickers hardness values for some common gems and other materials.	2
1.2	a) A picture of a standard drill head used in the oil and gas industry where the black cylindrical components are made of polycrystalline diamond compacts [4].	3
1.3	A depiction of four methods by which natural diamond formation is likely to have occurred. 1) Within the Earth's mantle, delivered by eruptions, 2) subduction zones, 3) asteroid impacts, 4) Extraterrestrial asteroid impacts forming diamonds on meteorites that have then fallen to Earth [22].	6
1.4	A schematic of a belt press used to synthesise high pressure high temperature diamond.	6
1.5	a) and b) show two processes for CVD growth of diamond, hot filament and microwave plasma respectively - figure taken from Ashfold et al. 1994 [27].	7
1.6	a) A slab, b) channel, and c) rib waveguide geometry. In each of these examples the wave propagation is in the z-axis (into the page) with the electric or magnetic field components transverse to this direction. The refractive index n_2 is $< n_1$ and n_3 might be equal to or less than n_1 . For clarity the geometries are also shown in 3D.	11

1.7	An example of a resonant peak measured from a transmission sweep through a bus waveguide which has coupled to a ring resonator. . . .	12
1.8	a) The material stack of diamond grown on a Si carrier wafer and b) a scanning electron micrograph of the material stack [49].	14
1.9	A process flow showing the cloning and tiled growth of single crystal diamond using a mosaic seed array [50].	15
1.10	A micrograph of a GaP device patterned on a diamond substrate with over etching into the diamond for increased mode confinement [56].	17
1.11	Top: A false colour SEM image depicting Raman lasing being initiated within a diamond microring resonator. Bot: An SEM showing other fabricated devices with a 500 nm coupling gap and visible polymer tapers [63].	19
1.12	A process flow for fabrication of high-quality, ultra-thin, single crystal diamond membrane windows suspended in a diamond frame for handling [34].	21
1.13	A diamond racetrack resonator that was fabricated by angled etching. It is suspended above the bulk material it was fabricated from by two anchor points on the coupling sections of the resonator. The scale bar depicts a 10 μm length [72].	22
1.14	A diamond photonic crystal fabricated using focused ion beam milling [75].	22
2.1	A process flow showing the steps taken for fabrication of a thin free-standing diamond membrane.	27
2.2	A schematic of ICP-RIE showing the locations of RF coils, platen, and gas inlets [86].	29

2.3	A fractured diamond piece showcasing the dangers of micro-manipulation of thin membranes. The diamond is bonded onto a piece of silicon and fringing can be seen due to variations in thickness and separation between the diamond and substrate.	30
2.4	The integrated optics assembly of a Wyko NT1100 optical profiler with labels detailing key components [90].	32
2.5	A schematic of a white light interferometer for optically profiling samples.	33
2.6	A 3-dimensional optical profile measurement showing the varying thickness of a diamond chip.	34
2.7	A depiction of white light coherence length showing different wavelengths of light adding together to form a pulse envelope [92]. .	35
2.8	A schematic showing two pulse envelopes overlapping on a thin transparent substrate [92].	35
2.9	A Dektak stylus profileometer with main components labelled. . . .	36
2.10	London Dispersion forces arise due to the instantaneous formation of temporary dipoles, shown here for two nonpolar diatomic molecules.	38
2.11	A schematic of the AFM tool used in this work [102].	39
2.12	A schematic showing the dimensions along which each diamond was laser cut and polished into 8 individual platelets.	40
2.13	The thickness profile of a single crystal diamond chip throughout several hours of thinning by argon-chlorine ICP.	41
2.14	A schematic showing lateral reduction in the size of a nominal diamond membrane if over etched.	42

2.15 a) An AFM measurement on a $10 \mu\text{m}^2$ area for an as received diamond chip post-CVD growth, and mechanical polishing - r.m.s. roughness of 1.8 nm. b) Shows the same diamond after 3 hours of Ar-Cl ₂ plasma thinning with an r.m.s. roughness reduced to 0.4 nm over a similar $10 \mu\text{m}^2$ area.	43
3.1 A schematic showing the layer stack of an SOI wafer ready to be etched for fabrication of 500 nm wide waveguides.	46
3.2 A schematic showing how transmission spectra would vary as the injected wavelength becomes resonant with a nearby ring cavity. . .	47
3.3 Schematic of a racetrack resonator showing power cross coupling, transmission, and loss parameters.	48
3.4 Cross-sectional mode simulations showing the modes' power distribution for the three cases of: Si device alone, Si device with diamond bonded and a buffering cap, and Si device with diamond bonded and the buffering cap removed through RIE.	50
3.5 Simulated group index values for the three device geometries of Si-HSQ, Si-HSQ-Diamond, Si-Diamond.	51
3.6 a) & b) Schematics of the diamond membrane bonding procedure onto a processed silicon photonic chip, from a top and side view respectively. Bonding of the materials is facilitated by capillary action bringing the surfaces into contact. c) A cross sectional schematic of how the diamond membrane conforms over and bonds with the target Si device.	53

3.7	An oblique-view SEM image showing the bonding of a 1 μm diamond membrane to a Si bus waveguide; it can be seen that the diamond conforms back to and contacts with the substrate within a few micrometres. <i>Inset</i> : Enlarged image at the site of the interface showing the gap between the membrane and substrate.	54
3.8	Schematic showing how optical interference fringes are created by an optical flat [112].	55
3.9	a) An optical image of a diamond membrane bonded over a Si resonator device showing interference fringes, a contacted region, and waveguides. b) Optical image showing the line profile on which fringe analysis was conducted to calculate the height profile over the Si device, where A and B point to either end of the waveguide resonator. c) A height profile calculated from the fringe intensity over the line profile as shown in b) with the black lines signifying the waveguide positions of the racetrack labelled again as A and B.	57
3.10	A schematic of the end-fire rig used to optically measure the silicon devices before and after the bonding of thin diamond membranes. A tunable laser through some polarisation maintaining fibre is coupled to the end facet of a device and the emissions collected from the exit facet using an objective. The collected light is focused through a polariser onto a photodetector and infrared camera via a beam splitter.	58
3.11	The normalised transmission spectra for a) the as-fabricated Si device and when bonded with the diamond pre- b) and post- c) removal of the HSQ mask cap.	59

3.12	Extracted (circles), and simulated (dashed lines) group index values for the Si ring resonator alone, and when bonded with the 1 μm diamond membrane with and without an HSQ cap. The measured results show a group index shift and gradient in agreement with the simulated values.	60
3.13	A cross-sectional mode simulation showing the TE modal power distribution at a wavelength of 1.535 μm for a diamond membrane 70 nm above a Si waveguide with no HSQ cap.	61
3.14	Cross coupling coefficients for the cases of, as fabricated Si device, and bonded to a diamond membrane with and without the HSQ cap used to pattern the device.	62
3.15	a) A top scattering image of a 1 μm diamond membrane bonded to a Si ring resonator off resonance. The red dashed line marks where the edge of the diamond is, and the red box highlights the scattering at this edge. b) The resonator was tuned into resonance, and again with the red lines and box highlighting the edge of the diamond and scattering respectively.	63
3.16	Loaded Q-Factor values for the cases of a silicon device alone, and bonded with diamond with and without the HSQ cap used to pattern the device. The solid lines show the general trend of the data.	64
4.1	a) A 3D schematic showing an example of what a wedged diamond membrane might look like & b) how devices of tailored thicknesses could be fabricated from such a membrane.	67
4.2	a) A schematic showing an example mask pattern aligned with the direction of greatest thickness variation, shown by a black arrow. b) A mask pattern aligned with the cleave axes of a diamond piece for maximising device number.	69

4.3	a) A 3D schematic of the PDMS stamp used in the printing of diamond platelets and disk resonators for this work, b) and also in 2D.	70
4.4	a) The stage is brought towards PDMS stamp, b) the pyramidal features are compressed with the device in full contact with the PDMS, c) the greater adhesion between stamp over substrate allows for removal of the diamond. Decompression of the stamp features allows printing elsewhere due to reduced contact area and thus adhesion to the PDMS.	71
4.5	A schematic showing the process flow of fabricating tessellated square diamond membranes.	72
4.6	a) A 45 deg tilted-view, SEM micrograph, of 4 membranes that were printed for AFM measurements shown in bottom figure - black arrow across membrane indicates the direction of height profiles. b) Height profiles of the 4 printed membranes shown in the SEM image with thickness differences (y) labelled on each.	73
4.7	a) A 45 deg tilted-view, SEM micrograph, of 4 thicker diamond membranes printed for thickness characterisation. b) A plot showing the fine and coarse thickness selection from an array of diamond tessellated platelets.	75
4.8	a) A 3D schematic of a transfer printed diamond device on a SOI waveguide platform b) as well as a 2D representation for clarity. . . .	76
4.9	One dimensional mode solutions, numerically calculated, for a diamond membrane of different thickness values, bonded on a SiO ₂ lower cladding. The dashed line at 1800 nm shows the target thickness, with the shaded box showing the variation in thickness due to material wedge.	78

4.10 a) The power distributions of the first three whispering gallery modes of a diamond disk resonator with 1800 nm thickness on an insulator substrate. b) A plot of the percentage of power present in the location of a waveguide as a function of lateral position offset, x , from the disk edge.	79
4.11 The group index values for the first three order TM modes calculated from effective index simulations across a wavelength range of 1530-1620.	80
4.12 The free spectral range values for the first three order TM modes calculated from group index values across a wavelength range of 1530-1620.	81
4.13 45 and 25 μm radius diamond disks printed onto silicon waveguides. Inset: A diamond disk being printed using a PDMS stamp onto a HSQ clad Si waveguide. Scale bars are 90 μm	82
4.14 A normalised intensity transmission sweep from 1520 - 1630 nm at 100 μW for a hybrid diamond-silicon resonator device assembled through transfer printing. Three sets of modes are identified and their free spectral ranges labelled.	83
4.15 a) A representative resonance centred around 1549.25 nm with a calculated Q-factor of $\sim 3.2 \times 10^4$. b) A stand out resonance centered around 1587.60 nm with a high Q-factor of $\sim 8.2 \times 10^4$	84
4.16 Power cross coupling coefficients (red) and distributed losses (black) are plotted versus Q-factor.	84
5.1 A micro-electro-mechanical device used for the tuning of resonant wavelengths [134].	87
5.2 Hysteresis curve showing, feedback-dependent, multivalued intensity output for a range of intensity inputs [137].	89

5.3	A resonance position shifting as an increasing percentage of the injection power is coupled into the disk. The solid blue and red lines are the cold-cavity and maximally detuned resonant peak respectively. The dashed lines depict a non-disturbing, low-power probe measurement of the peak at different red-shifted positions.	92
5.4	Absorption in diamond as a function of wavelength [140].	94
5.5	Power dependent transmission spectrum showing a resonance centred around 1545.13 nm red shifted with increasing powers up to 45 pm. The dashed lines are fits to the data with an estimated input power-dependent shift in effective index of $8 \times 10^{-3} \text{W}^{-1}$	95
5.6	Power dependent transmission spectrum showing minimal shift in a resonant peak centred at 1522.23 nm, 10 pm. The dashed lines are fits to the data with an estimated input power-dependent shift in effective index of $2.2 \times 10^{-3} \text{W}^{-1}$	96
5.7	The coefficient $\delta n / \delta P$ is plotted against distributed losses for each peak showing a correlation between increase in loss and increase in absorption, thus effective index shift.	97
5.8	The optical setup used for the measurement of power dependent refractive index change.	98
5.9	Probe measured wavelength shift of a resonance centred at ~1545 nm for different pump powers at 1563 resonance. Inset: Probe measurement of the shifted peak showing an undisturbed profile - background noise has changed slightly due to non-polarisation-maintaining amplification.	99
5.10	A false colour image taken using a thermal camera of the SOI device chip integrated with diamond disks. Red arrows point to 4 disks that were printed onto the chip.	99

5.11 An intensity difference image between two thermal camera measurements at zero injected power and the highest on-chip power achieved - approximated at 4mW. 100

6.1 a) An optical microscope image of a grayscale patterned slope of photoresist. b) A dektak thickness measurement of the same photoresist. 107

List of Tables

1.1	Parameter recipes used in the plasma etching of diamond.	4
2.1	Parameter recipes used in the plasma etching of diamond.	30

List of Abbreviations

SOI	Silicon-On-Insulator
SC	Single Crystal
SCD	Single Crystal Diamond
eV	electron Volt
UV	Ultra Violet
IR	InfraRed
NV	Nitrogen Vacancy
SiV	Silicon Vacancy
HPHT	High-Pressure-High-Temperature
CVD	Chemical Vapour Deposition
TE	Transverse Electric
TM	Transverse Magnetic
FWHM	Full Width Half Maximum
ZPL	Zero Phonon Line
HSQ	Hydrogen SilseQuioxane
RIE	Reactive Ion Etching
ICP	Inductively Coupled Plasma
SEM	Scanning Electron M icroscopy
FIB	Focused Ion B eam
RF	Radio Frequency
IPA	IsoPropyl Alcohol
CCD	Charge Coupled Device

VSI	Vertical Scanning Interferometry
AFM	Atomic Force Microscopy
PD	PhotoDiode
ppb	parts per billion
FDE	Finite Difference Eigenmode
FSR	Free Spectral Range
EDFA	Erbium Doped Fibre Amplifier
OSA	Optical Spectral Analyser

For Erika

Chapter 1

Single crystal diamond for integrated optical applications

1.1 Introduction

In this chapter, the motivation behind using diamond for integrated optical applications is detailed. A general background into integrated optics and waveguide theory is given to aid the understanding of concepts discussed throughout the document. The background of electronic-grade single-crystal diamond synthesis is presented, and the challenges that have impeded its wider utilisation are discussed. Notable works that address these issues are reviewed and their findings are used to detail the approach that is taken in this work. Finally the chapter concludes with a short breakdown of what each subsequent chapter will contain thus providing a narrative of the thesis at a glance.

1.2 Background and Motivation

Diamond was first used as a tool with which to polish stone axes and has long been an attractive material to humankind [1]. For approximately the last eighty years diamond has been prized as the gemstone with which to show one's commitment [2]. Now, in recent years, it is emerging as a promising candidate for

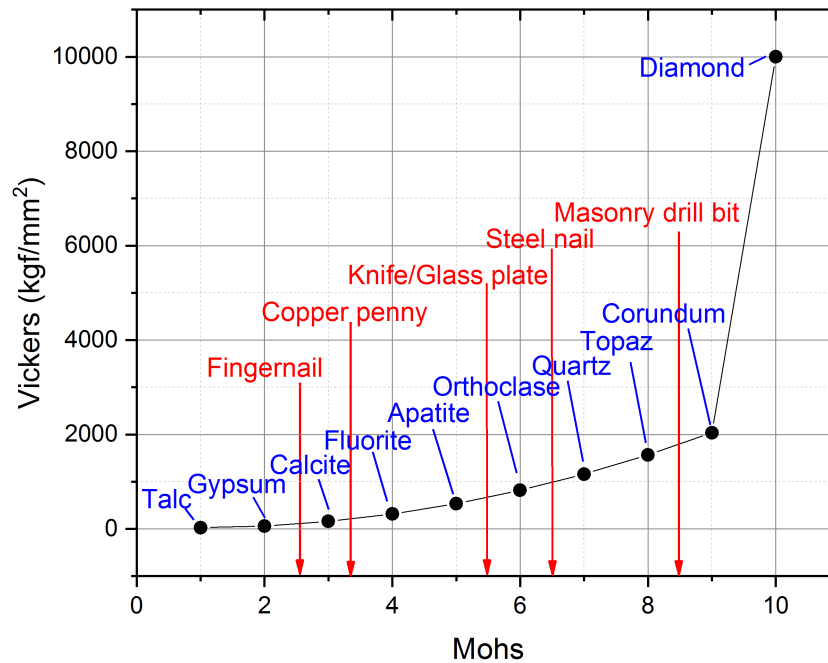


FIGURE 1.1: A table showing the Mohs and Vickers hardness values for some common gems and other materials.

quantum cryptography and information processing [1]. As far as materials go, diamond is indeed impressive. It is harder than almost all other known materials, four to five times more so than the next nearest gemstones - rubies and sapphires (corundum) [3]. The Mohs and Vickers hardness values of some common materials can be seen in Figure 1.1, a qualitative ordinal scale characterising scratch resistance, and a quantitative measure of a materials resistance to plastic deformation respectively. This incredible hardness sees diamond used ubiquitously in the oil and gas industry, to prolong drill bit lifetimes and increase drilling speeds - where any unplanned downtime can be very costly. Figure 1.2 shows such a drill head where the black cylindrical features are polycrystalline diamond compacts. Diamond is also chemically inert [5], bio-inert [6], and has the highest thermal conductivity of any solid at room temperature [7]. These



FIGURE 1.2: a) A picture of a standard drill head used in the oil and gas industry where the black cylindrical components are made of polycrystalline diamond compacts [4].

attributes make diamond stand out as a material which could be used in many extreme applications, such as radiation detection [8], heat sinks [9], and optical windows in corrosive environments [10]. In some of these extreme environments, only diamond could be used, where other materials would be damaged or diminished in the properties that made them attractive to begin with.

The primary focus of this research however is on the appealing optical properties of diamond. It has a large bandgap of 5.5 eV, preventing thermally generated charge carriers [1]. It also boasts a broadband transparency wavelength range, which covers from the deep UV to the infrared [1], enabling multispectral optical applications on a single platform. The nitrogen vacancy (NV) used in quantum applications for example, could be excited at 532 nm and have its 637 nm emission collected through the same integrated diamond platform [11]. It also exhibits attractive Raman properties, with a large - narrow linewidth - shift, centred at 1332 cm^{-1} . This allows for efficient Raman shifted lasing at exotic

Semiconductor optical properties					
Material	Bandgap (eV)	Refractive Index	Transparency range (μm)	Kerr coefficient (m^2/W)	Thermal Conductivity ($\text{W}/\text{m}\cdot\text{K}$)
Diamond	5.5	2.39	0.23-20+	1×10^{-5}	2300
Silicon Carbide	2.61	2.55	0.37-5.6	1×10^{-5}	375
Gallium Nitride	3.4	2.32	0.5-7	7×10^{-5}	200
Silicon	1.14	3.48	1.1-15	1.8×10^{-4}	150

TABLE 1.1: Parameter recipes used in the plasma etching of diamond.

wavelengths, with both the pump and shifted wavelengths - again - guided on the same platform. The large Raman gain of $\sim 10\text{cm}/\text{GW}$ at $1\ \mu\text{m}$, combined with diamond's aforementioned thermal and transparent properties, enables efficient, high-power bench-top systems - which can be developed with unprecedented average power and wavelength ranges [12, 13]. Diamond has a small thermo-optic coefficient of $\sim 10^{-6}\text{K}^{-1}$ [14], thus the effective index of a diamond device will stay relatively stable across a range of thermal changes. It exhibits a relatively large Kerr non-linearity ($n_2 = 1.3\times 10^{-15}\ \text{cm}^2/\text{W}$) [15], allowing for tuning of the refractive index relative to the square of an applied electric field. It has a high refractive index of ~ 2.4 for waveguiding, and it plays host to over 500 defect centres [1] - some of which, like the nitrogen and silicon vacancies (SiV), have shown great promise as optically accessible spin registers for quantum information processing applications [16, 17, 18, 19].

This array of impressive properties make diamond attractive for planar optics and a comparison with other relevant semiconductor materials is shown in Table 1.1. Naturally occurring diamonds however are rare, expensive, and variable in optical quality. In the next section, techniques used in the fabrication of synthetic high quality diamond are discussed.

1.3 Synthesis of diamond

1.3.1 High pressure high temperature

Diamond can be synthesised through simulating the high-pressures and high-temperatures (HPHT) that resulted in the formation of natural gems to begin with, ~60 GPa and 1000-1600 °C [20, 21]. The four scenarios diamond is thought to have been created from are:

- within the Earth's mantle, delivered to the surface by deep-source eruptions;
- at subduction zones, where movements of the tectonic plates cause one to be forced under another - the descending plate being exposed to increasing temperatures and pressures;
- at the site of asteroid impacts with the earth's surface, hitting with large forces that generate great pressures and temperatures;
- formed in space in some meteorites.

This information is shown pictorially in Figure 1.3. To mimic these conditions, a cell filled with a mixture of metals; a high purity carbon source; and some diamond seed crystals; can be placed between two anvils with a belt press used to maintain radial pressure as shown in Figure 1.4. The internal temperature is raised to 1500 °C which dissolves the carbon source into the solvent metal where it is transported by a local temperature gradient to the seed crystals - forming a large synthetic diamond crystal [23, 24]. Diamond growth occurs preferentially as, in the hotter region of the molten metal, it has a higher solubility compared with graphite. This provides a concentration gradient, with net flow of carbon atoms from the hot source to cool diamond seed crystal sink [25]. Solvent metals are typically group VIII metals and their alloys [26], with preferential growth of particular crystal faces occurring depending on the combination.

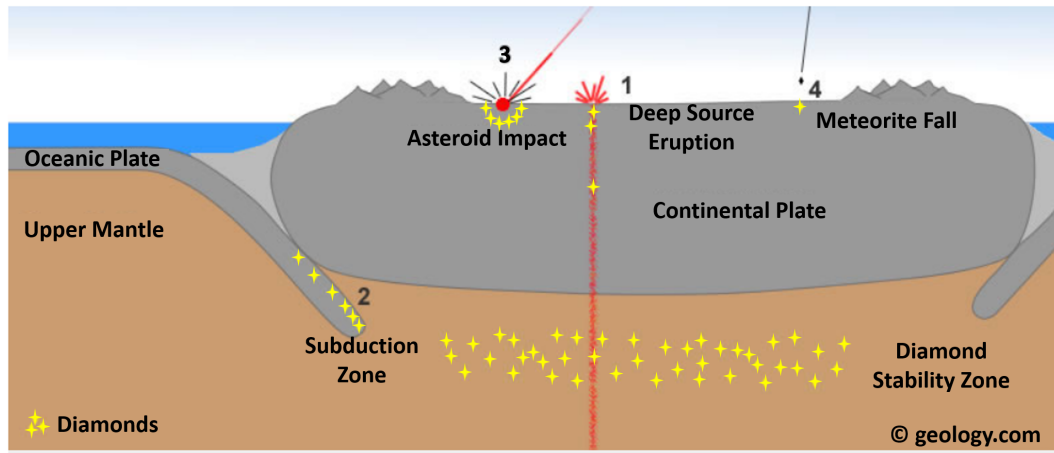


FIGURE 1.3: A depiction of four methods by which natural diamond formation is likely to have occurred. 1) Within the Earth’s mantle, delivered by eruptions, 2) subduction zones, 3) asteroid impacts, 4) Extraterrestrial asteroid impacts forming diamonds on meteorites that have then fallen to Earth [22].

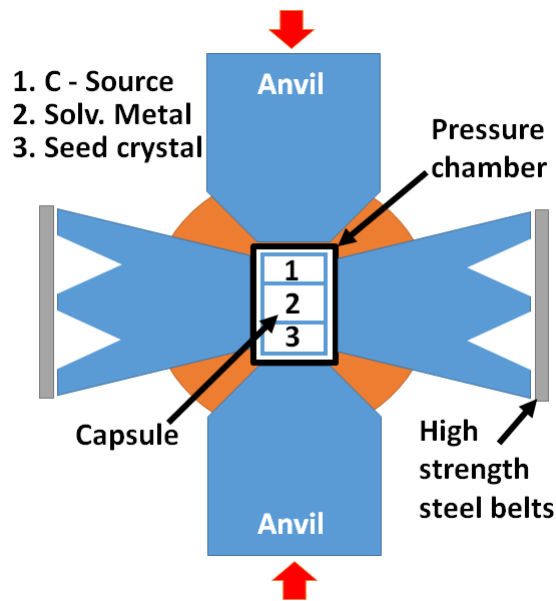


FIGURE 1.4: A schematic of a belt press used to synthesise high pressure high temperature diamond.

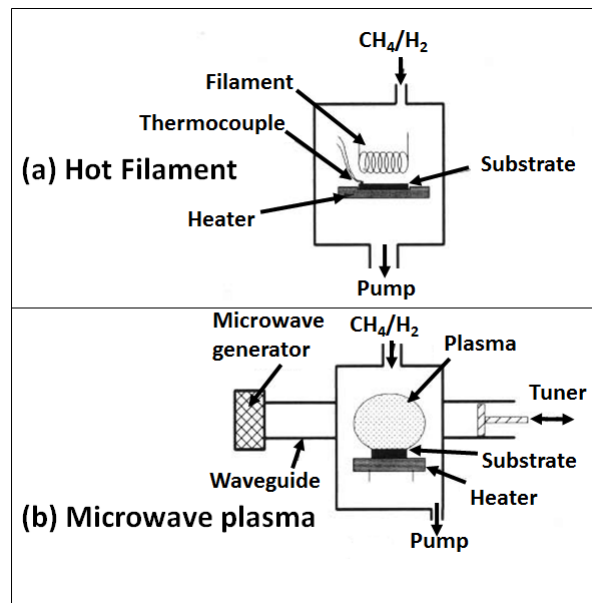


FIGURE 1.5: a) and b) show two processes for CVD growth of diamond, hot filament and microwave plasma respectively - figure taken from Ashfold et al. 1994 [27].

Despite it being possible to fabricate single crystal diamond by this process, the control over dopant levels is minimally flexible and so optical-grade diamond is usually fabricated by chemical vapour deposition [1]. HPHT finds regular usage however as an abrasive, such as in the aforementioned drill bit, or as a heat sink - making use of its large thermal conductivity [27].

1.3.2 Chemical vapour deposition

High optical-grade diamond is controllably and repeatedly grown by chemical vapour deposition (CVD) from single crystal diamond seeds. Two approaches to this process are outlined in Figure 1.5 which involves hydrogen gas with small % amounts of methane (or other hydrocarbons) being activated by hot filament or microwave-enhanced plasma [27]. The reactants are transported through the chamber by diffusion and convection towards the deposition surface. A complex combination of adsorption, diffusion, and desorption of various species occurs -

largely dominated by the nucleation of diamond particles and the suppression of sp² (graphitic) carbon. This process is carefully controlled by the mixture of gas and the substrate temperature [28, 27, 29, 30, 31].

This technique, despite providing a method of synthetically fabricating diamond with a carefully controlled purity, is inherently limited to growing chips of a similar scale to that of the seed crystal [32]. To reuse diamond seeds multiple times, the chip can either be laser cut, or ion-implanted, creating a damaged layer between the newly grown material and the growth plate - the damaged layer can then be preferentially etched [33]. Laser cutting requires multiple beam passes, a process where it is difficult to maintain beam parallelism, thus highly wedged samples need to be cut thicker - such that they can be mechanically polished afterwards. Ion implantation creates internal strain to the diamond and thus if too thin a diamond membrane is removed, bowing or fracturing can occur [34, 35]. For this reason, as well as an increased robustness to mechanical polishing, CVD grown diamond is nominally grown to a thickness of several tens to hundreds of micrometres before it is harvested from the seed crystal. Diamond's incredible hardness leads to difficulties in material processing and so regularly, chemical mechanical polishing is used to smooth its surface by placing it under pressure beneath an iron scaife and spinning with a diamond grit in an olive oil binder [36, 37]. By this method root-mean-square surface-roughness values of ~200 pm have been shown - but so too has an induced sub-surface damage that requires plasma etching to remove[37].

The attractive diamond optical properties and how an appropriate grade of crystal might be sourced have now been discussed. In the next section a background and introduction to integrated optical devices is given and how this optical platform might be used to exploit diamond is described.

1.4 Integrated Optics

1.4.1 Background

Diamond's optical properties can be made use of through free-space optics: such as by depositing high reflectivity coatings on mm thick diamond chips and pumping with pulsed lasers to induce Raman lasing [38]. Emissions from diamond defect centres can also be enhanced and collected, by placing defect containing diamond membranes or nanodiamonds into open-access optical microcavities with $>10\,000$ Q-factors [39, 40]. As with all optical materials and their applications however, many benefits exist from moving to an integrated optical platform. For example, small component sizes with the potential of scalability, are possible through standardised lithography and plasma etching techniques. Devices are robust to vibration, requiring no alignment as they are solid-state structures, and a greatly reduced mode volume facilitates higher optical interaction with the material. This benefits the optical properties of diamond by reducing the threshold power for effects such as Raman lasing, also by increasing defect enhancement, and increasing defect emission-collection efficiencies. Raman lasing is a stimulated inelastic phonon scattering that absorbs and re-emits a photon at lower energy, giving access to a wide range of exotic wavelengths. Another potential benefit of waveguiding structures within diamond, is that the interaction between two NV defects, for entanglement say, occurs on-chip without requiring extraction of the photons from the host material first.

1.4.2 Planar waveguide and resonator structures

Waveguiding is made possible by utilising a contrast in two or more material's refractive indices, with light being confined to the higher index region of the structure. A simplified ray optics view of this - for fibre optical cables - is that

beyond some critical incident angle, the light is totally internally reflected within the structure. In highly confining structures, such as those in integrated optics, the confinement of the wave needs to be more precisely described using Maxwell's equations and their boundary conditions. Analytical solutions to these problems do not exist and as such software packages using finite difference eigenmode approximations are used to numerically determine the mode supporting properties of certain structures. The technique works by solving Maxwell's equations on a cross-sectional mesh of waveguide and then formulating an eigenvalue problem which can be solved using sparse matrix techniques[41].

Several of these different waveguide geometries, depicting the refractive index contrasts that would lead to light confinement, are shown in Figure 1.6. A one-dimensionally confining slab (a), a channel waveguide surrounded by a lower index cladding (b) and a shallow etched rib waveguide (c). The different geometries are utilised based on application or material constraints, for example a rib waveguide might be used to guide on the upper surface of a bulk material that has difficulty being thinned to wavelength scale dimensions. A channel waveguide however offers less coupling to radiative modes and higher confinement with more optical intensity. Modes of a dielectric waveguide are defined in terms of the electric field components of the propagating electromagnetic wave. An electromagnetic wave consists of, as the name would suggest, electric and magnetic field components - which are perpendicular to one another. For modes defined as transverse electric (TE): the electric field is transverse to, and the magnetic field component normal to, the direction of wave propagation. Transverse magnetic (TM) modes have the magnetic field transverse to; and the electric field normal to, the direction of propagation. The direction of propagation with reference to Figure 1.6, would be along the z axis. The primary relevance of these concepts to the work presented, is that TE waves have more modal extension laterally and TM modes have more vertically - this is an

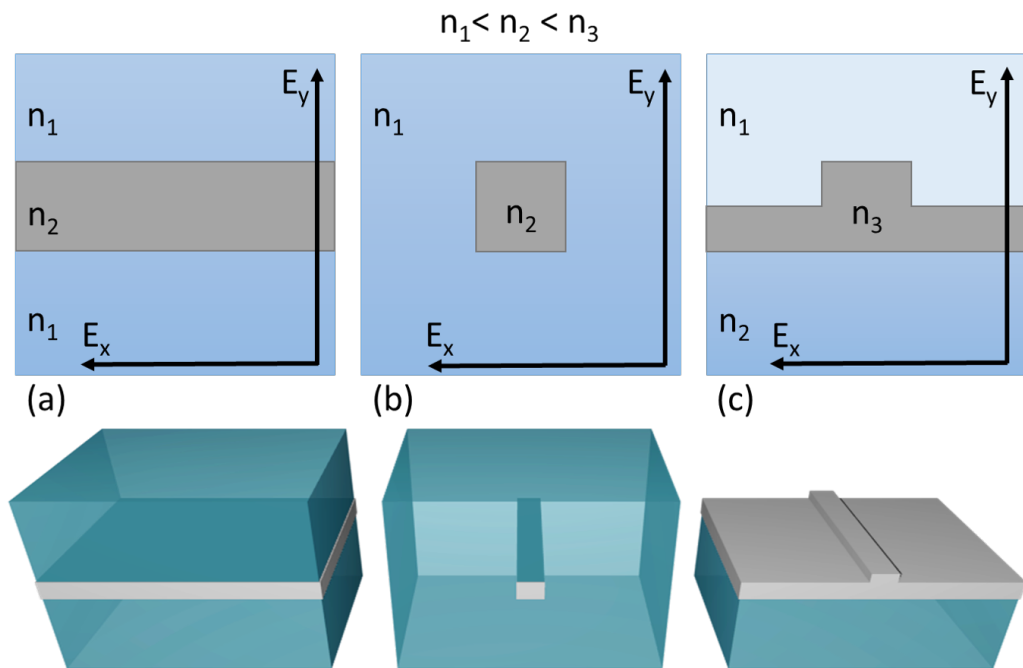


FIGURE 1.6: a) A slab, b) channel, and c) rib waveguide geometry. In each of these examples the wave propagation is in the z -axis (into the page) with the electric or magnetic field components transverse to this direction. The refractive index n_2 is $< n_1$ and n_3 might be equal to or less than n_1 . For clarity the geometries are also shown in 3D.

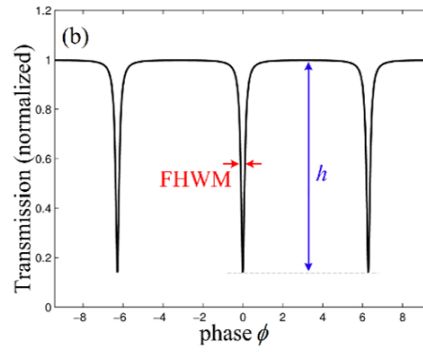


FIGURE 1.7: An example of a resonant peak measured from a transmission sweep through a bus waveguide which has coupled to a ring resonator.

important consideration depending on the coupling schemes used.

The device structures used in this work are fabricated from a waveguide which has formed a closed gate, such as in a ring, racetrack, or disk geometry. Light is coupled into the ring from a bus waveguide, by having the device fabricated or micro-assembled in close proximity to the waveguide. Travelling light within the cavity destructively interferes for all wavelengths whose phase change is not an integer multiple of 2π . The resonant wavelength condition is thus given as:

$$\lambda_r = \frac{2\pi R n_{eff}}{m} \quad (1.1)$$

where R is the radius of the ring or disk, n_{eff} is the effective index experienced by the mode, and m is an integer number. When the resonance condition is met the light couples into and propagates around the ring - resulting in a drop of intensity detected at the output facet of the coupling waveguide. Several useful properties can be extracted from the transmission of such a resonator by looking at the extinction, full-width-half-maximum (FWHM), and wavelength position of the resonant wavelengths, shown in Figure 1.7. A full description of the waveguiding properties and transmission spectra of ring resonators are given in Chapter 3.

A consequence of coupling only specific wavelengths into the resonators, is

that they can be used to filter light. With multiple cascaded resonators, higher-order optical filters are possible. The filters are tuneable by a variety of methods that change the length or effective index, and thus solutions to the resonant wave condition. This results in a measurable shift in the resonant wavelengths of a transmission sweep [42]. This tuneable difference in resonant peaks allows for a resonator to be used as a sensor, for example in changes of mechanical strain [43], or biological and chemical environment [44], and also temperature change [45]. Additionally micro-ring resonators have potential as all-optical switches for fast binary switching at low power [42]. Cavities, such as ring resonators, can also act to alter the available optical density of states and thus increase or decrease the spontaneous emission rates of energy level relaxations - used for example to enhance the zero phonon line (ZPL) emissions and suppress the phonon sideband of the diamond NV centre.

The benefits to using integrated optics for diamond photonics has been discussed and a brief introduction to the terms and concepts of waveguiding has been given. In the following section the challenges that need to be addressed to realise diamond integrated optics is discussed.

1.5 Challenges to using diamond for integrated optics

Integrated optical components are usually fabricated using template wafers where a thin film of high index material is sputtered, CVD grown, or thermally oxidised on a lower index substrate. Through lithography and plasma-etching, planar waveguides that are single mode supporting at target wavelengths can easily be fabricated. For meeting the single mode criterion of waveguiding, the film thickness needs to be approximately on the order of wavelength to be guided, divided by the refractive index of the material it is to be guided in [46]. The thickness of an as-grown CVD diamond is much larger than that of the single

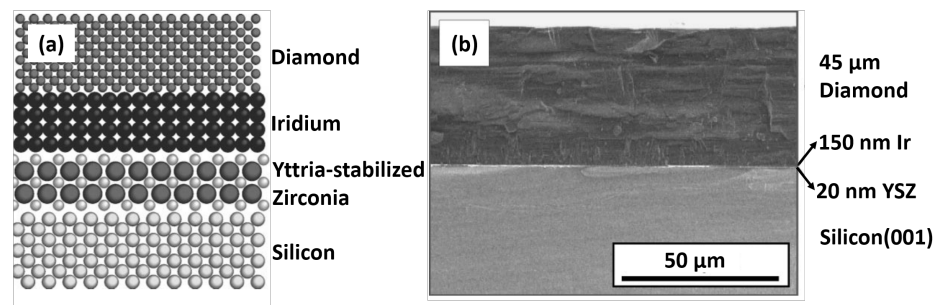


FIGURE 1.8: a) The material stack of diamond grown on a Si carrier wafer and b) a scanning electron micrograph of the material stack [49].

mode guiding criterion and requires the chip to first be thinned. Rib geometries can relax this thickness requirement, and have been demonstrated in diamond [47, 5], but these will suffer from large amounts of bending losses due to lower confinement and coupling to radiative modes [46]. Ideally, a template-wafer analogous to SOI for diamond would be used however this is not yet possible. Research in this field has shown some promise, with diamond growth on mono-crystalline iridium buffer layers however these have to be grown to $> 30 \mu\text{m}$ thickness before dissolution of grain boundaries occur, this is shown in Figure 1.8 [48, 49]. Instead, CVD grown single crystal chips are usually purchased commercially with $200\text{-}500 \mu\text{m}$ thickness. They are then thinned using plasma etching to some target thickness for single mode operation at a chosen wavelength.

Not only limited in thickness, diamond is also severely limited in lateral dimensions, with at most $4\text{-}10 \text{ mm}^2$ areas - starkly smaller than current integrated optical chips. Methods of overcoming this, such as through CVD growth using several seed crystals as a mosaic base for growing larger crystals has been utilised, as shown in Figure 1.9. The separate crystals amalgamate throughout the growth process with the resulting monolithic chip used as a new larger seed crystal. Unfortunately a high defect density builds up at the connection lines which

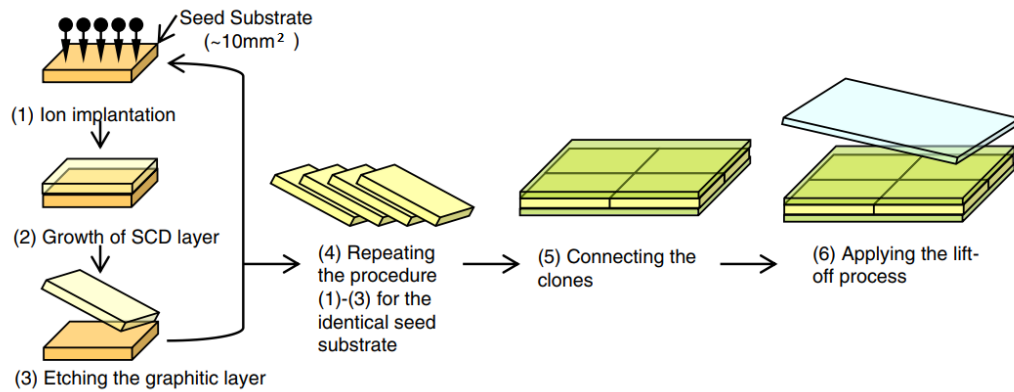


FIGURE 1.9: A process flow showing the cloning and tiled growth of single crystal diamond using a mosaic seed array [50].

propagate through all future crystal growth and thus these areas could not be used for optical devices [33].

Plasma-thinned diamond membranes, of a few mm^2 dimensions, are not ideal for large scale integrated optics. To overcome this, hybrid integration of passive and active components, fabricated from different material platforms, are of great interest. By combining different materials, attractive properties from each can be brought together into a single device. Hybridising materials by this approach, requires careful consideration of the optical properties - such as the wavelength transparency ranges of each. The refractive indices and thickness of each candidate must also be considered, such that waveguiding is not disturbed unfavourably where they meet.

1.5.1 Diamond-Silicon integrated optics

Of the potential material platforms that diamond could be integrated with, silicon is particularly attractive. Firstly, it is used regularly for integrated optical devices and has the potential to combine optical, optoelectronic, and electronic components on a single substrate[51]. Due to its ubiquity, the infrastructure surrounding wafer fabrication and processing techniques are well-developed and

the costs are low. Silicon and diamond are both transparent at the near, to far-infrared wavelengths, which could be utilised for non-linear diamond processes. For example, Raman emissions could be cascaded and guided on a single chip. Silicon is also a well understood platform, which reduces ambiguity in qualifying the optical properties of a hybrid diamond-silicon device. For these reasons the remaining chapters dealing with the hybrid integration of diamond will use Silicon as the target platform.

In the next section of this chapter however, a brief overview of several other works detailing some other methods by which diamond can be utilised in photonic integrated circuitry are discussed.

1.6 Current diamond technologies

Below are some of the key demonstrations in the field of diamond integrated optics.

1.6.1 Gallium Phosphide membranes on bulk diamond

Two of the three issues highlighted in Section 1.5 were, that optical grade single crystal diamond nominally has a larger than desirable thickness, and that the thickness itself is wedged. Recent publications have shown that both these challenges can be addressed by using other material platforms as the wave confining structure and interacting evanescently with the diamond substrate. This pre-empts the need for large amounts of diamond material to be removed and also provides a uniform penetration depth into the diamond irrespective of wedge.

One such material, GaP, exhibits low optical absorption with a bandgap of 2.3 eV [52] and a large refractive index that can be used for guiding NV emissions. The works of Fu et al., of the University of Washington [52, 53, 54, 55], have shown that GaP membranes of approximately 100 – 200 nm can be transferred onto a diamond substrate and subsequently patterned into hybrid-material devices with

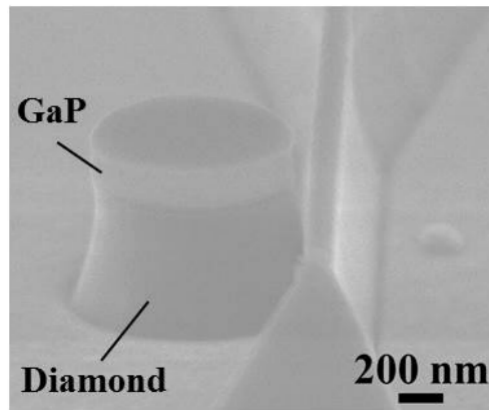


FIGURE 1.10: A micrograph of a GaP device patterned on a diamond substrate with over etching into the diamond for increased mode confinement [56].

light interaction into the diamond. The GaP membranes are grown on a sacrificial $\text{Al}_{0.8}\text{Ga}_{0.2}\text{P}$ layer, which itself was epitaxially grown on a GaP substrate. Using a 1.5 % hydrofluoric acid solution the membrane can be released and transferred onto the diamond. At this stage electron beam lithography of a hydrogen silsesquioxane (HSQ) negative resist and subsequent reactive ion etching (RIE) using a $\text{Cl}_2/\text{N}_2/\text{Ar}$ recipe can transfer device patterns into the GaP. Finally an O_2 RIE to etch partially into the diamond gives an enhanced optical confinement by lowering the effective refractive index of the nanocavities underlying substrate. An example of such hybrid devices is shown in Figure 1.10.

By fabricating hybrid resonator devices in this manner, diamond chips with NV centres close to its surface can have their emission enhanced into useful ZPL decay paths through the Purcell effect. The effect details the increase or decrease in spontaneous emission rate of a quantum system by its environment changing the optical density of states. A GaP-Diamond resonator as described, showed Q-factors of 5100 for an overcoupled resonance, the simulated field distribution for this mode with an ideally oriented NV, 20 nm below the diamond surface, would give a Purcell enhancement factor of 24 – the magnitude by which the optical density of states has been increased [52]. The enhancement scales as a

function of the resonator Q-factor and inversely with the mode volume. For many applications this weak evanescent coupling gives a poor modal overlap with the emitter and is a limiting factor. Also, NVs this close to the surface are often fabricated using an ion implantation and annealing procedure which can see the defect emissions suffer from spectral diffusion - limiting efficient readout of spin and spin-photon entanglement [11, 57]. It is also well-known that surface termination can have a negative effect on favourable properties of near-surface emitters, such as NV⁻ luminescence [58, 59, 60]. To address these issues, a similar fabrication approach but with a material of lower index than GaP, would provide a greater modal overlap with the defect emitter, or less stringent requirements on depth of NVs. Incorporation of the NV centres during the growth of thin epitaxial layers have also been shown to have better optical properties and could benefit the approach [61].

1.6.2 Diamond patterned on insulator

Alternatively, there have also been several publications that use diamond as the waveguiding material itself [62, 12, 52]. Loncar et al. for example, have shown that diamond optical devices can be fabricated by thinning the diamond into membranes and then bonding them to SiO₂ substrates. The waveguide and resonator structures are then fabricated using electron-beam lithography and plasma etching. By this approach a much larger (or complete) modal overlap into the diamond is possible – a vital consideration for the efficiency of enhancing defect emissions - or as these works show, Raman lasing. An example of a fabricated device and a false colour image depicting the Raman process are shown in Figure 1.11.

In this process the diamond is globally thinned first, using inductively coupled reactive ion etching (ICP-RIE), from 20 μm to $\sim 1\mu\text{m}$. Once at the target thickness the membranes are bonded to an O₂ plasma-activated silica substrate. The device

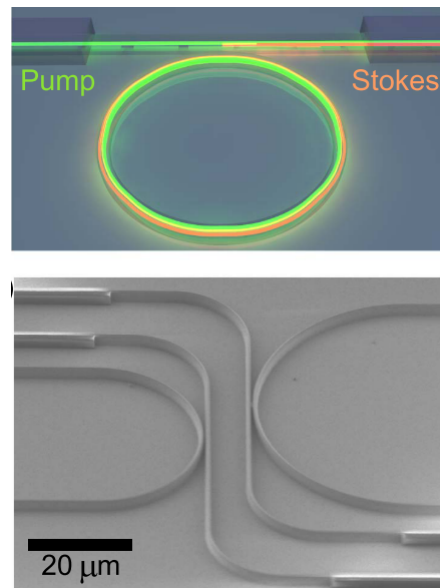


FIGURE 1.11: Top: A false colour SEM image depicting Raman lasing being initiated within a diamond microring resonator. Bot: An SEM showing other fabricated devices with a 500 nm coupling gap and visible polymer tapers [63].

structures are then patterned using electron beam lithography and dry etching, with tapered in- and out- coupling pads consisting of SU-8 patterned in a second e-beam lithography stage - extending the diamond waveguides to the end of the substrate[64, 12, 62, 65, 15]. Care is taken to align device patterns along the lowest gradient height-variation. Q-factors of larger than 300 000 have been demonstrated as well as Raman lasing with a threshold power as low as 20 mW[12, 64]. Diamond is able to support more circulating power without any negative thermal effects, and thus higher stoke shifted output powers allowing for cascaded Raman lasing towards longer wavelengths. The absorption of the silica in these devices hinders such an application where an all-diamond platform would be beneficial. This could be achieved by using angled etching techniques to fabricate suspended diamond resonator structures[66].

1.6.3 Suspended uniform thickness diamond windows

Addressing both the issues of non-uniformity in the diamond thickness, and an excess of diamond material to be removed, suspended diamond membranes within a diamond frame have been demonstrated [34, 67]. This technique builds on the approach of ion implantation and lift-off, to create free-standing diamond membranes with uniform thickness - a by product of the implantation ion's stopping distance. The process however leaves residual damage, which results in the membrane having strain in that region, degrading its optical quality. The membranes also tend to bow or crack after lift-off, limiting their usage [34]. To address this, CVD overgrowth can be used to create a high-quality single-crystal diamond layer with the damaged region removed afterwards using plasma-etching [68]. A remaining limitation which Praver et al. have addressed is the handling of such membranes. By suspending the membranes through overgrowth into a diamond frame, a method of fabricating robust, ultra-thin, uniform, and high-optical quality diamond membranes is possible.

The step-by-step process is as follows: ion implantation is used to create a damaged layer 1.7 μm beneath the surface, which upon annealing becomes graphitic. The upper layer of the diamond is then overgrown by CVD and then placed onto a bulk diamond frame, further CVD growth sees the two fused together. The graphitic layer is then selectively etched to remove the diamond frame and fused single-crystal layer from the bulk diamond. Etching by ICP-RIE on both the top and bottom of the stack is used to remove the damaged ion-implantation region and also thins the diamond within the frame. The entire process flow is shown in Figure 1.12.

The suspended diamond membranes were measured to be of a high-optical quality using Raman spectroscopy. An array of different photonic components were fabricated which could be used as building blocks for nanophotonic circuits.

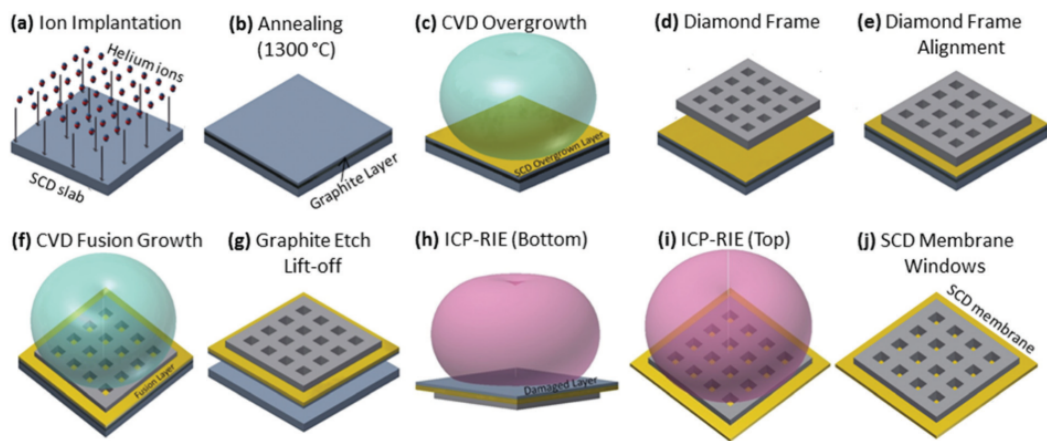


FIGURE 1.12: A process flow for fabrication of high-quality, ultra-thin, single crystal diamond membrane windows suspended in a diamond frame for handling [34].

One optical ring resonator with monolithic grating couplers was reported, showing loaded Q-factors of 66 000 and were coupled to using monolithic grating couplers.

1.6.4 Other works

There have also been many other notable works, such as the fabrication of photonic crystals with high Q-factors ($>10^5$) and high-efficiency fibre-optical interfaces, increasing collection of single photons for use in quantum information processing [69, 66]. Diamond nanowires address the issue of photon out-coupling from the high index bulk diamond devices by producing a ten times greater flux with ten times less power [70, 71]. Suspended diamond structures have also been demonstrated using Faraday-cage angled etching with high Q-factors of 286 000 as the racetrack resonator shown in Figure 1.13 [72, 73, 74]. This technique shows, that in the absence of a template wafer - where a thin film is heteroepitaxially grown on another material substrate - single mode device structures can still be fabricated in bulk materials.

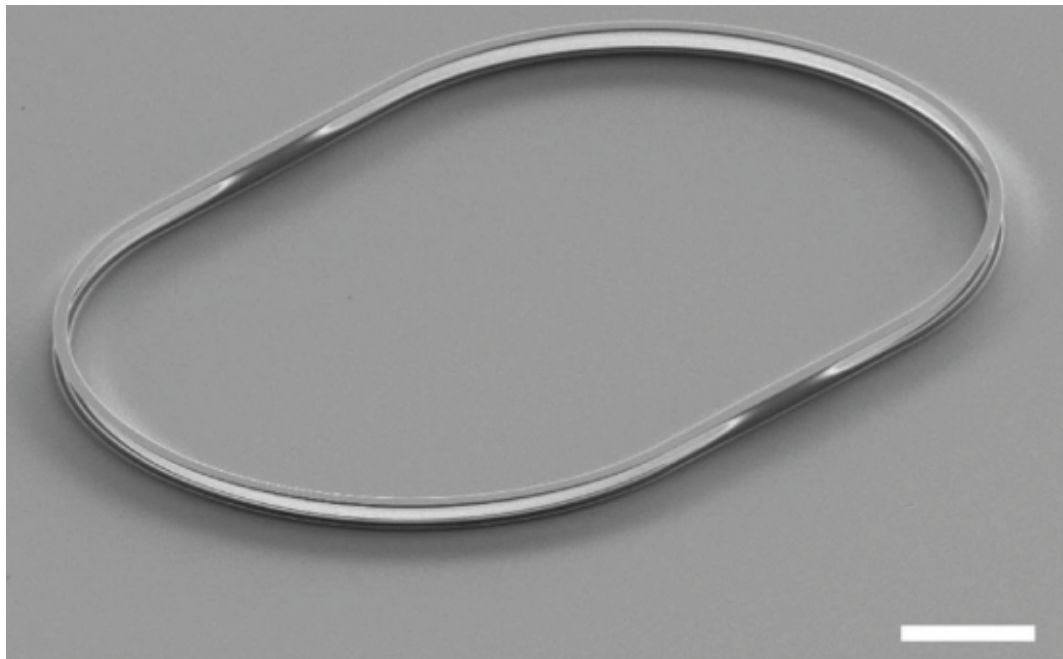


FIGURE 1.13: A diamond racetrack resonator that was fabricated by angled etching. It is suspended above the bulk material it was fabricated from by two anchor points on the coupling sections of the resonator. The scale bar depicts a $10\ \mu\text{m}$ length [72].

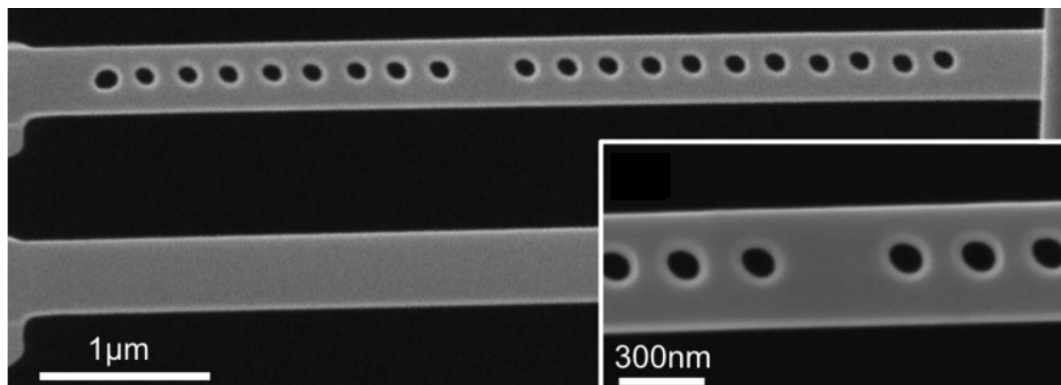


FIGURE 1.14: A diamond photonic crystal fabricated using focused ion beam milling [75].

1.7 Thesis outline

Many of the techniques presented have shown great promise in diamond optics, though many are still limited. Some in the dimensions of possible devices, due to the restricted geometry of the diamond, or some in the efficiency which the diamond can couple to other platforms for wider integration.

The intention of this thesis is to show that: by utilising already existing photonic platforms and heterogeneously integrating the diamond with them, its exciting properties can be made use of on-demand and without sacrificing chip size. Addressed are, the challenges of a non-uniform thickness in diamond chips; the reduction in material thickness from large 10s of micrometres diamond down to a single mode regime; overcoming limited chip sizes by integrating ultra-thin membranes with wafer size optical platforms; the issues of small mode overlap into the diamond by fabrication and integration of monolithic diamond disk resonators; and finally the possible misalignment of cavity resonances, with respect to a targeted wavelength, using thermal tuning of diamond resonator modes.

Chapter 2 will detail the methodology and tools used in the fabrication of ultra-thin membranes as well as the techniques used in the characterisation and handling of the platelets, such as atomic force microscopy and vertical scanning interferometry. Thin diamond films help satisfy not only concerns of the single mode criterion but are also simple to bond without need of adhesives.

Chapter 3 discusses, in detail, this capillary-assisted intermolecular bonding and how a membrane of reduced thickness can deform more readily, aiding in bonding. The integration of thin diamond with silicon resonator devices is demonstrated. The modal overlap into the diamond which directs potential applications was investigated using finite element simulations, as well as the quality of the interface investigated both mechanically and optically using SEM,

fringe analysis, and optical transmission spectra.

Building on those exciting results, a means by which to systematically bond devices is demonstrated in Chapter 4. Individual devices were fabricated from a thin diamond membrane with the wedged thickness mitigated over local device geometries. Polymer elastomeric stamps are used to pick-up and transfer diamond devices to non-native substrates. Specifically, both an array of tessellated square membranes and disk resonators were fabricated and printed. Typical thickness variations of ~ 230 nm across local device dimensions of ~ 70 μm were found and the optical quality of hybrid diamond devices were found to have high-average Q-factors of 1.8×10^5 .

Chapter 5, using the process flow developed in the previous chapter, demonstrates a thermally tuneable hybrid diamond-silicon micro-disk resonator. Tuning across > 450 pm was demonstrated and a separable control over tuning and probe was shown with great promise for tuning resonances to match defect emissions for example.

Chapter 6 summarises the findings of this work and looks to the predicted future of the research.

Chapter 2

Ultra-thin diamond membrane fabrication & characterisation

As detailed in Chapter 1, high optical-quality, thin diamond would facilitate many photonic applications and technologies due to its impressive array of properties. Several key challenges exist however, that must be overcome to utilise these properties effectively. Contrary to silicon photonic foundries, optical grade wafer-scale templates for diamond are currently unavailable. Some work on growing wafer scale diamond on monocrystalline-iridium has been done, but currently these diamond layers need to be $> 30 \mu\text{m}$ before dissolution of networked grain boundaries begins to occur, and as such are unsuitable for planar optical devices [48]. Optical grade single crystal diamond is CVD grown from seed crystals and are nominally a few mm^2 in size. The diamond is then removed from the seed crystal through high energy implantation, and annealing to create a sub-surface damaged layer that will etch more readily than the non-damaged diamond. To prevent the membrane curling or cracking during lift-off, due to induced strain from this process, CVD overgrowth of more diamond material is used to provide mechanical stability. This consequently leads to chips that are thicker than single-mode visible-wavelength compatibility [76, 77]. Membranes of appropriate thickness are thus regularly fabricated in a "top-down" approach by

laser cutting, mechanically polishing, and plasma thinning the diamond chips obtained through CVD [63, 78]. Nominally however, fabrication of diamond membranes by this technique result in a non-uniform thickness - with wedges ranging from 300 nm to several micrometres height difference across a few millimetre sample length [78, 12, 79, 15, 80, 81]. The variation of thickness adds a further layer of complexity, limiting device design along the lowest thickness gradient of the diamond to mitigate the difference [82, 79, 15]. Alternatively, suspended diamond windows have been fabricated within a thicker diamond frame - also using ion implantation and CVD overgrowth [80] - however membranes of lesser thickness can be achieved as the frame provides the mechanical support to prevent curling. Preclusion of laser cutting and mechanical polishing results in very uniform thin membranes, however the lateral dimensions are still severely limited. Another approach is to avoid fabricating devices within the diamond at all, which can instead be interacted with evanescently. It has been demonstrated that thin GaP membranes can be fabricated, bonded to diamond, and subsequently patterned into devices - with guided modes in the GaP overlapping into the bulk diamond [52, 53, 54, 55]. The chip geometry of the GaP is however limited again by the dimensions of the diamond. It is demonstrated in this Chapter, that the optical issues of a wedged thickness; and the limitations of small-size optical grade diamond; are addressed if thin diamond membranes are fabricated, and integrated with devices engineered from established wafer-scale technologies. This method, as well as handling, measurement, and characterisation techniques that were utilised throughout the process, are discussed in the following chapter. Membranes of sub-micrometre thickness were fabricated with 0.4 nm r.m.s. roughness and a $\sim 4 \mu\text{m}$ wedge across a 2 mm length.

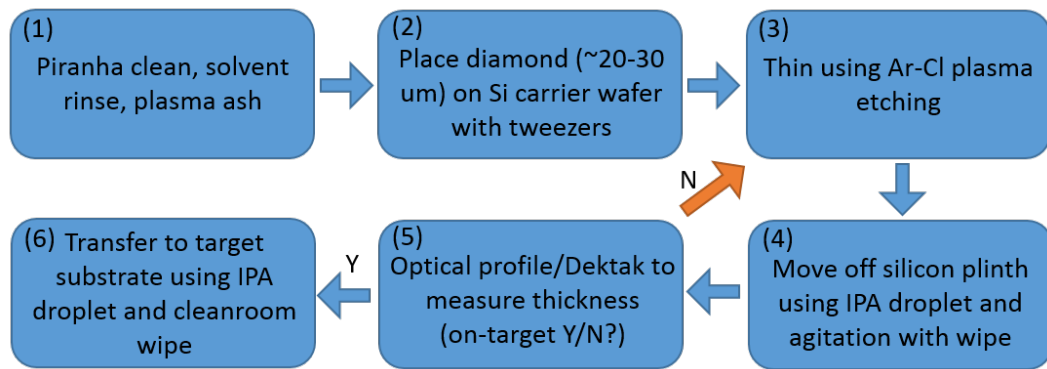


FIGURE 2.1: A process flow showing the steps taken for fabrication of a thin free-standing diamond membrane.

2.1 Ultra-thin diamond membrane fabrication

Single crystal electronic grade diamond chips of a few mm^2 can be commercially sourced, and from these readily available chips thin membranes can be fabricated. Diamond however, is chemically inert and poses a significant challenge in accurately etching monolithic photonic structures [1]. For this reason, techniques such as laser ablation [83]; ion-implantation and lift-off [84]; focused ion beam milling (FIB) [76]; and reactive ion etching (RIE) [85] have been used to fabricate devices in diamond. From these techniques RIE also provides a uniform etch across an entire diamond chip which can be used to fabricate diamond membranes. CVD fabricated diamond however, as previously noted in the introduction, is overgrown for mechanical stability and as such is first laser diced, and mechanically polished into smaller diamond platlets to reduce etch time. This introduces sub-surface damage, but that can also be removed during the RIE stages.

The process flow of a diamond membrane fabrication is shown in Figure 2.1. Each plate after the laser cutting and polishing stages is cleaned of any organic contaminants using $\text{H}_2\text{SO}_4:\text{H}_2\text{O}_2$ in a ratio of 3:1 (Piranha); a solvent rinse of acetone, followed by IPA; and a 250 °C pure oxygen plasma ash (1). The plates are

placed without adhesive in the centre of a Si carrier wafer (2), chosen for its low cost and ubiquity. The diamond and the carrier wafer were globally etched in an inductively coupled plasma reactive ion etch (ICP-RIE). After thinning, the diamond is re-positioned off the underlying silicon plinth (4), resulting from the plasma etching of surrounding carrier wafer unmasked by the diamond during the process. This allows direct measurement of the diamond thickness using vertical light interferometry and stylus profileometry (5). The thinning and measurement stages are repeated until a target thickness has been reached. Integration of the diamond with a non-native substrate can then be achieved using capillary-assisted bonding (6).

For this type of bonding thinned diamond is necessary, as the attractive forces that keep it in place drop off dramatically beyond a few nanometres from the surface of the substrate - resulting in difficulties with achieving intimate contact. The proximity can be more readily achieved if the membrane can deform over surface features like the devices it is to be integrated with. In order to deform sufficiently, the stress, which is dictated by an applied force on the cross-sectional area of the material, must be great enough. As the film decreases in thickness, assuming the applied force and stiffness of the film remain constant, this stress is more readily achieved allowing better contact between the film and the substrate, and thus a stronger bond.

The ICP-RIE tool used in the thinning process is shown schematically in Figure 2.2. The plasma is initiated by alternating the magnetic field via a radial coil around the etch chamber, labelled ICP power, which induces an RF electromagnetic field that strips the gas molecules of their electrons and creates a plasma. An alternating bias is applied to the platen stage, labelled Table bias, beneath the sample's carrier wafer controlling the acceleration with which ion bombardment occurs. This differs from standard RIE which relies on the RF platen power to generate the plasma, thus control of ion acceleration and plasma density

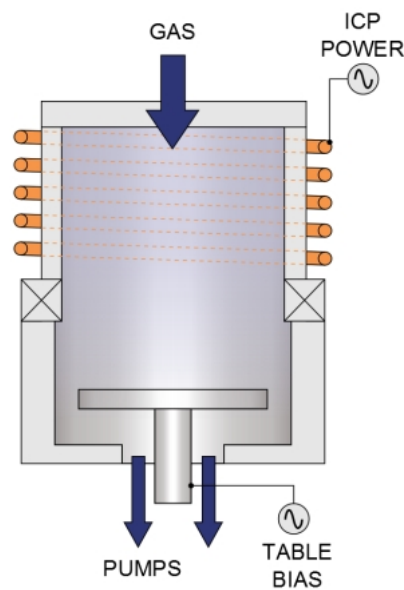


FIGURE 2.2: A schematic of ICP-RIE showing the locations of RF coils, platen, and gas inlets [86].

are not mutually exclusive.

2.1.1 Diamond etch chemistries

The diamond etching in this thesis was primarily by two different etch chemistries. The first, and the recipe used for the fabrication of diamond membranes, was a mixture of Argon-Chlorine. The etch parameters of which are shown in the first entry of Table 2.1 and can be associated with the schematic in Figure 2.2. It has previously been reported that this recipe has a smoothing effect on diamond, showing a reduction in r.m.s roughness from 0.53 nm to 0.19 nm after 10 mins [87]. The second etch recipe was used for the work presented in Chapter 3 and has been shown to give near-vertical sidewalls for diamond structures using a SiO₂ etch mask [88]. During and after the membrane fabrication process, several techniques are used for handling and characterisation of the diamond, which is discussed in the following sections.

Diamond etch recipes				
Gas 1 - flow rate (sccm)	Gas 2 - flow rate (sccm)	Platen power (W)	Coil power (W)	Chamber pressure (mTorr)[REF]
Ar - 25	Cl ₂ - 40	100	400	5[87]
Ar - 15	O ₂ - 40	300	800	5[88]

TABLE 2.1: Parameter recipes used in the plasma etching of diamond.

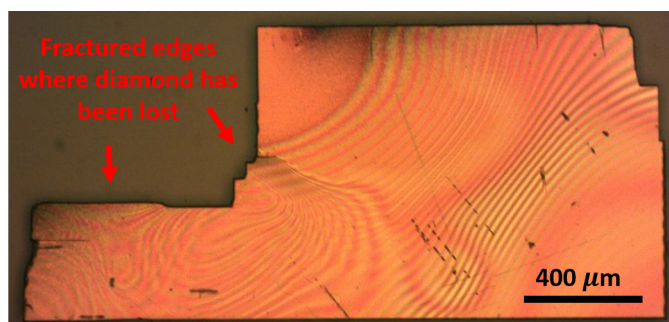


FIGURE 2.3: A fractured diamond piece showcasing the dangers of micro-manipulation of thin membranes. The diamond is bonded onto a piece of silicon and fringing can be seen due to variations in thickness and separation between the diamond and substrate.

2.2 Diamond membrane handling

Handling of the diamond at the beginning stages of membrane fabrication is possible with the use of tweezers. As the thinning progresses however, and fracturing of the material becomes a concern with an example of this shown in Figure 2.3, manipulation is instead achieved by means of interaction with a cleanroom wipe. The absorbent cloth is wetted with some drops of IPA, as is the membrane itself, and through gentle agitation using the wipe, the diamond can be positioned to a target location. The wetting helps reduce friction between the membrane and the carrier wafer as well as aiding in the membrane's initial delamination - permeating between the diamond-silicon interface and pushing the two apart. On completion of the membrane's fabrication and for further processing of the diamond, it might also be necessary to transfer the material from

one substrate to another. To achieve this, the same method is used to bring the diamond over the edge of its current substrate, where the (light-weight) membrane is drawn towards the wetted wipe, as opposed to dropping over the edge, due to the cohesive and adhesive properties of liquids. The wipe is then brought into contact with a target substrate using a lightly applied pressure, and additional solvent wetting; a greater attractive force is experienced with the smooth substrate than the porous wipe resulting in sample transfer. The following sections discuss the details of measurement and characterisation techniques that are employed during the fabrication.

2.3 Thickness and surface morphology measurements

Characterisation of diamond thickness throughout the thinning process is critical in achieving the single mode criterion of the vertical axis, as well as to prevent mode cut-off or a reduction in lateral dimensions through over etching. So too is the monitoring of surface roughness for improved bonding with other materials [89]. Several techniques are employed in these characterisations which are, vertical scanning interferometry, stylus profilometry, and atomic force microscopy - with each discussed in the following subsections.

2.3.1 Vertical scanning interferometry and stylus profilometry

A Wyko NT1100 optical profiler was used for all vertical scanning interferometric (VSI) measurements presented in this thesis and a labelled picture of the tool can be seen in Figure 2.4. The technique relies on a classical interferometer setup, i.e. one light source is directed through a beam splitter onto two reflective materials (nominally mirrors), but with each arm having a different optical path length - so upon recombination of the beams, interference occurs. For the optical profiler, one of the beam paths is directed onto an ultra smooth mirror component within the

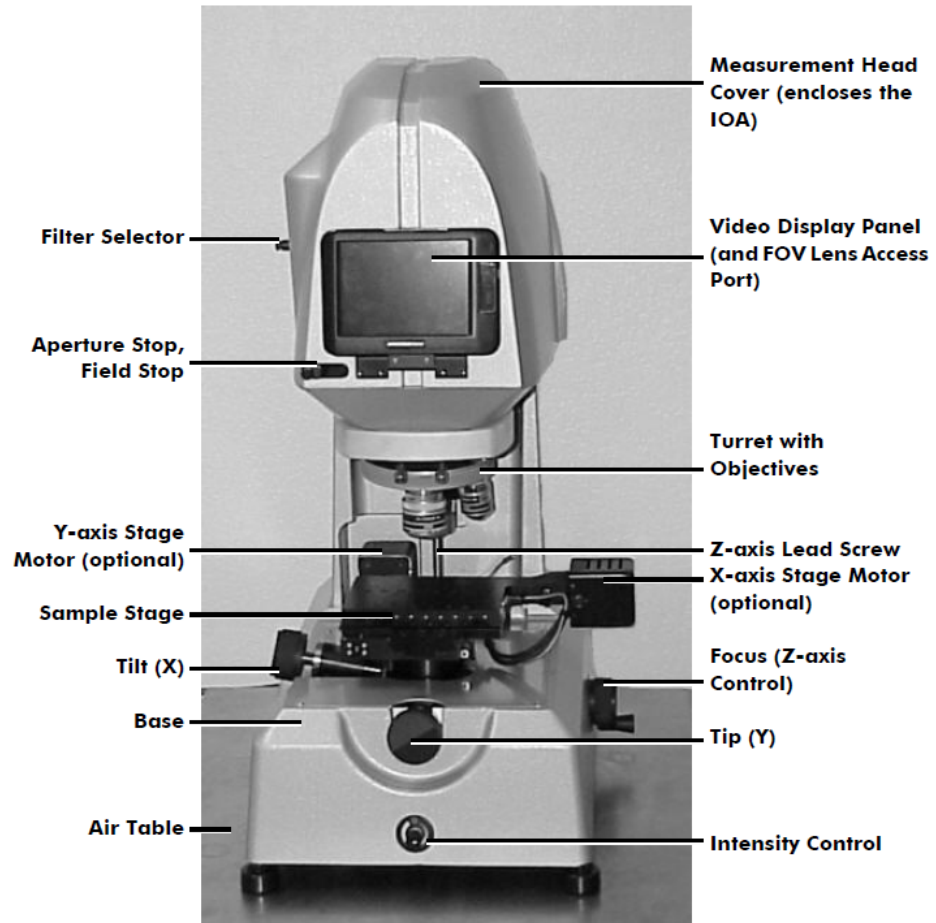


FIGURE 2.4: The integrated optics assembly of a Wyko NT1100 optical profiler with labels detailing key components [90].

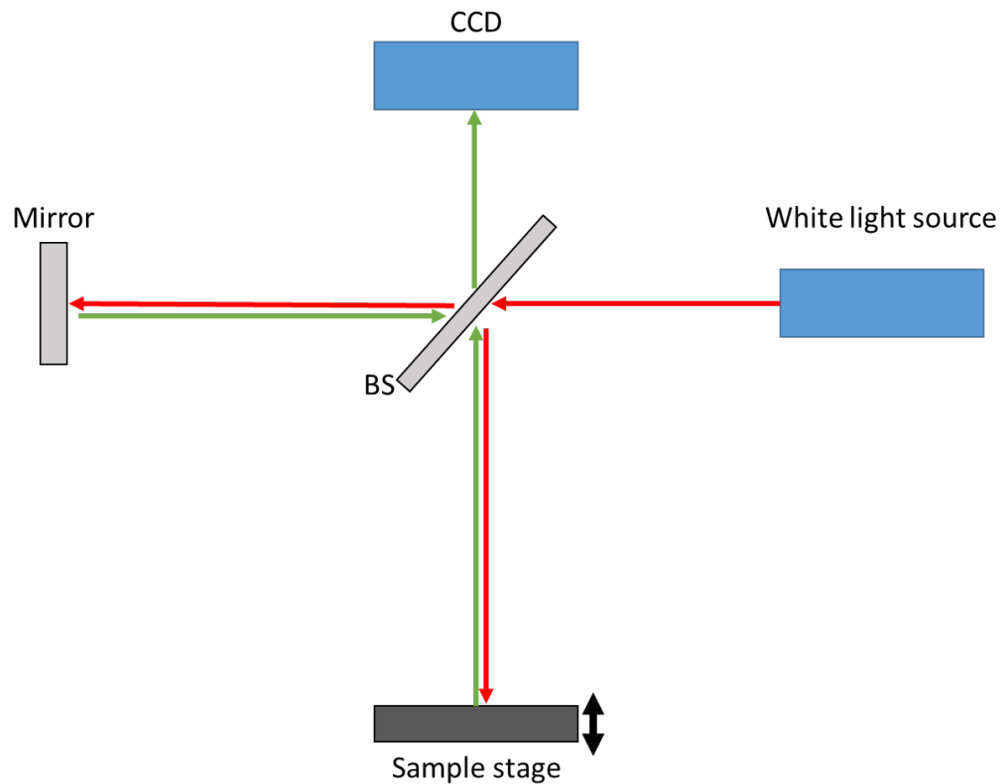


FIGURE 2.5: A schematic of a white light interferometer for optically profiling samples.

integrated optical assembly and reflects back to a charge coupled device (CCD) camera - to be used as a reference beam. The other beam path is directed towards a sample and then reflected back towards the camera. The sample stage is moved through the z-axis and as the sample comes into focus the two beam paths recombine to form interference patterns. For clarity a schematic is shown in Figure 2.5. These dark and bright fringes will reach a maximum contrast and then taper off as the translator stage passes through the focal point. The position of the stage is recorded for the point of maximum intensity of each CCD pixel resulting in a 3D profile of sample height. A white light source is used for its short coherence length which results in the highest fringe contrast at approximately the correct focal length, falling off rapidly away from focus [91].

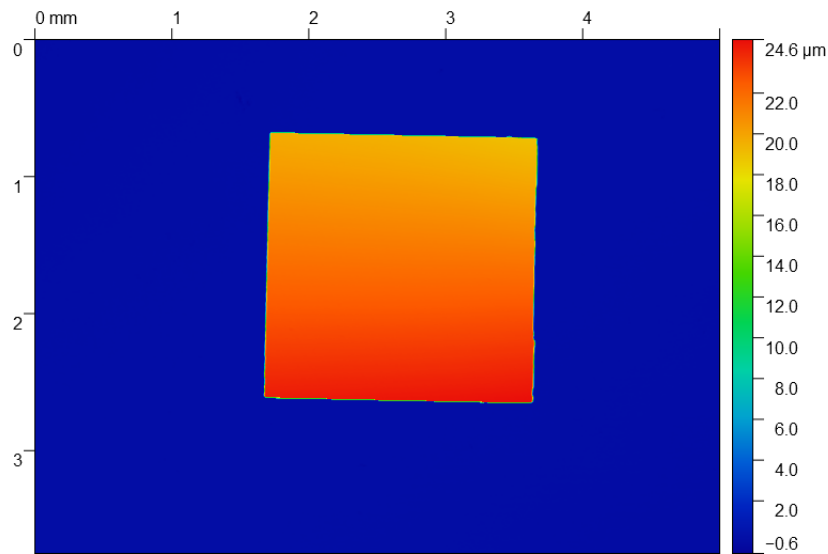


FIGURE 2.6: A 3-dimensional optical profile measurement showing the varying thickness of a diamond chip.

Using this method, regular measurements of the diamond thickness are taken between each etch of the thinning process. Nominally, before and after each etch, the diamond is repositioned off its underlying silicon plinth and measured, as is the plinth itself. This allows for monitoring of how the etch rates differ between each material for a given etch-chemistry, i.e. the selectivity. An example of such a 3 dimensional (3D) height map is shown in Figure 2.6.

Measurements using VSI are restricted to target thickness of $> 2 \mu\text{m}$, due to a limitation of the technique with thin materials. The coherence length, i.e. the pulse envelope in which the different wavelengths of white light do not destructively interfere - is approximately $2 \mu\text{m}$. This is demonstrated pictorially in Figure 2.7.

As such, for films of a thickness $< 2 \mu\text{m}$, the pulse envelopes at the focus of the diamond surface, and the surrounding silicon substrate, result in artefacts [93, 94]. As the diamond material is also transparent over the visible wavelengths, similar complex effects can occur across the whole sample as demonstrated in Figure 2.8. Software packages can be used for measuring such thin and transparent films, that deconvolve these overlapping envelopes by calibrating to a reference sample of the

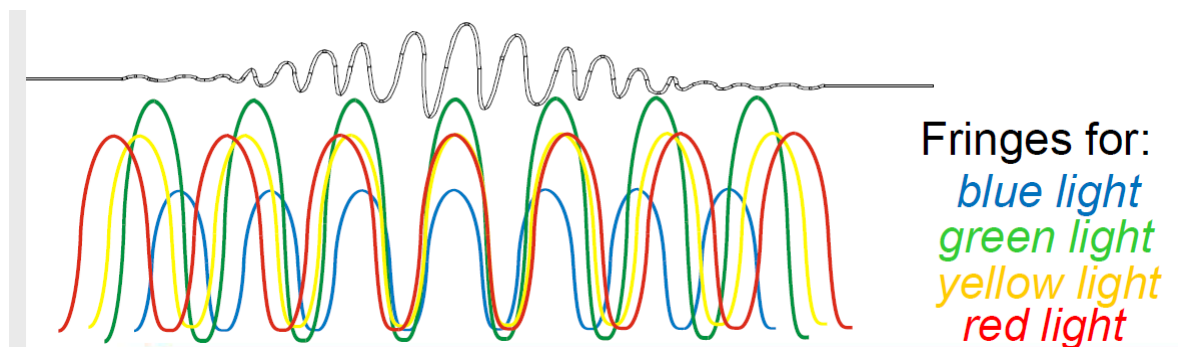


FIGURE 2.7: A depiction of white light coherence length showing different wavelengths of light adding together to form a pulse envelope [92].

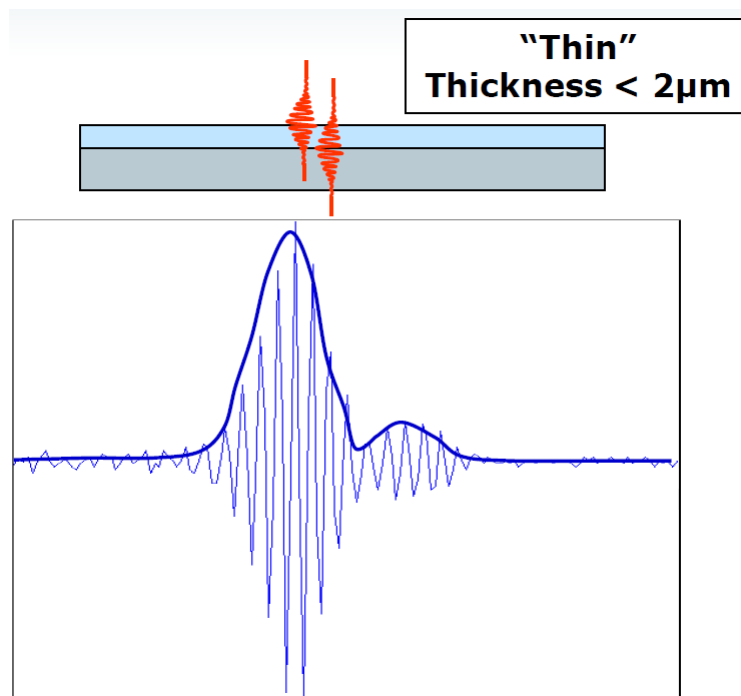


FIGURE 2.8: A schematic showing two pulse envelopes overlapping on a thin transparent substrate [92].

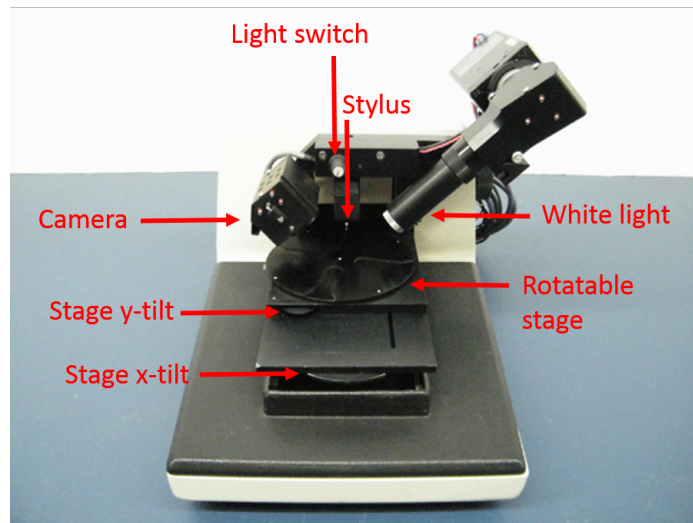


FIGURE 2.9: A Dektak stylus profileometer with main components labelled.

same material, on the same substrate - the reference sample must have a known thickness and tolerance. In the absence of this however, an alternative means of thickness measurement can be used - such as stylus profileometry. A Dektak stylus profileometer is shown, labelled in Figure 2.9. Simply, a white light source is used to illuminate a sample on a rotatable, tiltable, stage and observed with a camera connected to a computer for positioning. The stylus is then brought down onto the sample within a range of force between 0 - 300 μN , to prevent damaging sample or stylus. The stylus is then moved along an axis where the force applied to the stylus from a varying surface morphology will result in the tip rising or falling. The variation in tip height is thus a direct measurement of the sample thickness, and by taking such measurements at each corner of a diamond chip, and assuming a planar wedge - the 3D thickness profile can be approximated without the need for optical profiling. The operating ranges of each are, $\sim 150 \mu\text{m}$ to $2 \mu\text{m}$, for vertical scanning interferometry - with the upper limit dictated by the practical operating range of the z-scanner - and $2 \mu\text{m}$ to $< 10 \text{ nm}$ for the Dektak. The operators manual states a 10 \AA vertical resolution for the Dektak IIa that is available.

2.3.2 Atomic Force Microscopy

Surface roughness of fabricated membranes is a vital consideration for heterogeneous integration and low optical losses in photonic applications. In the following chapters of this thesis, different device geometries will be discussed, such as diamond as a top cladding layer over waveguides and as a waveguide itself - each with respective considerations on surface roughness. Scattering loss in planar optical waveguides from surface roughness is a practical reality and several studies have been conducted to quantify this analytically [95, 96, 97]. Not only do the scattering points induce loss by causing the fundamental mode to couple with radiation modes, but the correlation length of the surface roughness, and thus effective index variation, complicates things by possibly increasing or lowering the loss also [95]. It is thus necessary to pick etch chemistries that minimise such roughness when fabricating diamond devices.

The surface roughness on the membrane faces themselves, also impede a non-adhesive-aided integration of the diamond, as in the case of the diamond clad devices. This is due to a decrease of the surface contacted area of the two bodies as discussed in Section 2.1. To elaborate on that detail: the integration of diamond in this work is likely dominated by van der Waals, and as between two non-polar surfaces, is best described by the London dispersion forces (LDF) [98, 99, 100]. Dispersion forces are a very weak attraction that occur due to momentary dipoles as the electron distribution between the materials becomes uneven, and a weak residual attraction to the nuclei in one material of the electrons from a neighbouring material occurs, this is clarified in Figure 2.10. These forces have both an attractive, and repulsive component, coming to equilibrium in a Lennard-Jones type potential - where the attractive component has an inverse relationship with separation, r^6 [89]. This amounts to van der Waals forces having unlikely significance between macroscopic bodies at separations that exceed a few

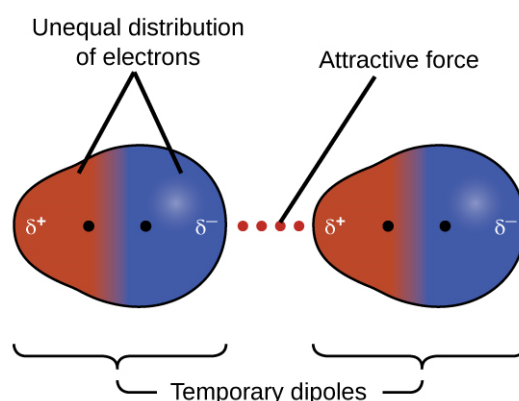


FIGURE 2.10: London Dispersion forces arise due to the instantaneous formation of temporary dipoles, shown here for two nonpolar diatomic molecules.

hundred angstroms [101]. In this case, other means of bonding would be required, such as by capillary action, or some adhesive. So in summary, an increase in surface roughness, even at the nanometre scale, is enough to separate regions of the macroscopic bodies such that they will not experience a large enough intermolecular attractive force to remain bonded.

To characterise the surface roughness of the membranes and devices fabricated in this thesis, the technique of atomic force microscopy (AFM) is used, where a typical tool schematic is shown in Figure 2.11. As can be seen, a laser is directed onto the back reflective surface of a spring microcantilever which directs the light onto a 4 quadrant photodiode (PD). The AFM measurements to be presented, are obtained using a constant force tapping mode, whereby the cantilever is oscillated close to its resonant frequency. When the tip of the cantilever is brought close to the sample surface, effects such as van der Waals, electrostatic forces, dipole-dipole interactions etc., cause this oscillation to change. Through electronic feedback of the PD, the cantilever oscillation frequency, defined by the user (set-point), is maintained by adjustment of the probe height. To obtain a measurement of surface roughness over a sample area then, the tip is brought into close contact and raster scanned across an area with the height of the probe

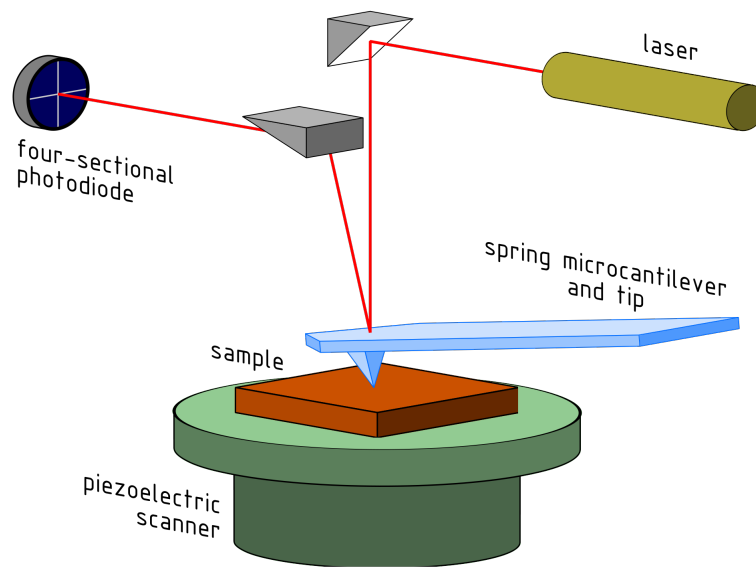


FIGURE 2.11: A schematic of the AFM tool used in this work [102].

monitored throughout.

2.4 Results and Discussion

2.4.1 Diamond material sourcing and preparation

CVD grown single crystal diamond chips were sourced commercially with dimensions of $4 \times 4 \text{ mm}^2$, and a thickness of 0.3 mm. These chips were of electronic grade and quoted as having low quantities of nitrogen and nitrogen vacancy centres - 5 ppb (often $< 1 \text{ ppb}$) and 0.03 ppb respectively. The crystals were grown in the $\{100\}$ face with $\langle 110 \rangle$ edge orientation. The chips, as received, have an average roughness of $< 5 \text{ nm}$.

Each diamond was laser cut through the short-axis midpoint once and the two halves cut again into 4 pieces - resulting in 8 diamond platelets per as-received chip, depicted in Figure 2.12. A frequency doubled Nd:YAG laser system with motion control is used for the diamond cutting and requires multiple passes. It is difficult to keep each cut perfectly aligned and the resulting chips can have

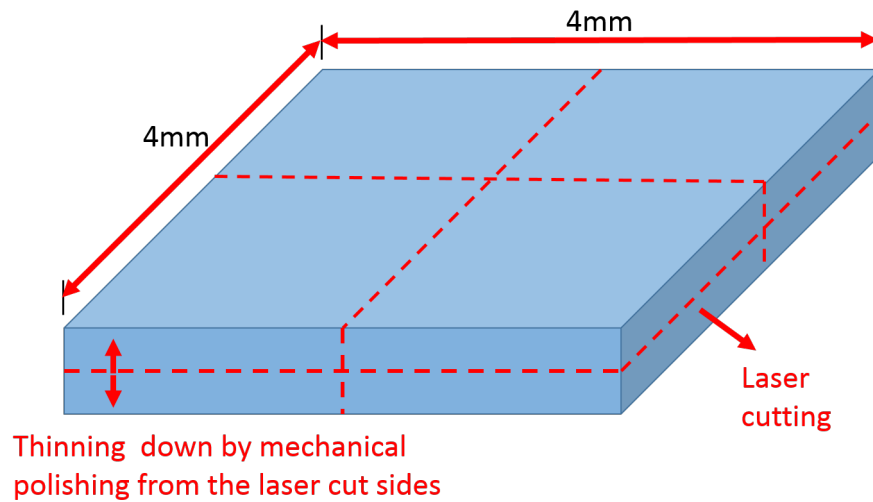


FIGURE 2.12: A schematic showing the dimensions along which each diamond was laser cut and polished into 8 individual platelets.

wedges as great as 40 - 50 μm across a 2 mm length. The 8 diamond platelets are mechanically polished and thinned from their laser cut faces to an approximate thickness of 30 μm and an r.m.s surface roughness of 1.8 nm over a 10 μm^2 . The mechanical polishing also reduces the wedge to a value less than 10 μm over the same 2 mm length.

2.4.2 Global thinning and characterisation

Diamond membranes of $< 1 \mu\text{m}$ were fabricated using the process flow as previously shown in Figure 2.1, and characterised using the different measurement techniques also described in the previous sections. Vertical scanning interferometry found a wedged thickness variation of 4 μm across the 2 mm sample length and a starting thickness of almost 20 μm - which will introduce mechanical difficulties during integration as detailed in Section 2.1 & 2.3.2. The thickness measurements of the fabricated membrane are plotted in Figure 2.13. This diamond membrane was used in the heterogeneous integration of a hybrid diamond-silicon planar waveguide device which is detailed in Chapter 3. It can be

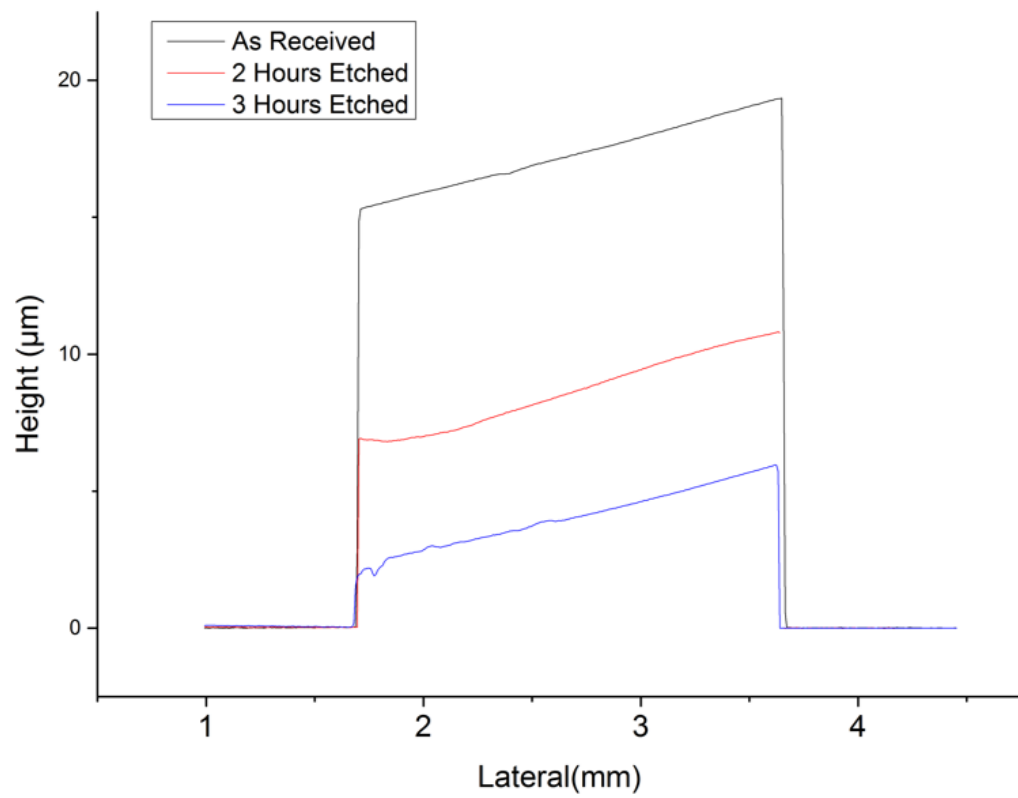


FIGURE 2.13: The thickness profile of a single crystal diamond chip throughout several hours of thinning by argon-chlorine ICP.

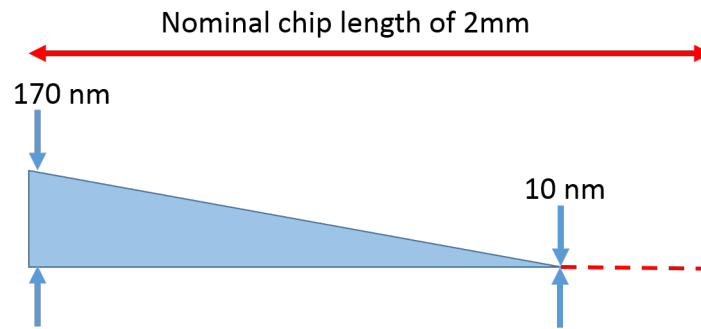


FIGURE 2.14: A schematic showing lateral reduction in the size of a nominal diamond membrane if over etched.

seen that the diamond profile has a wedged thickness of approximately $4 \mu\text{m}$ across a 2 mm length and a value of sub $1 \mu\text{m}$ on its thinnest corner. Wedges of this magnitude are typical of diamond prepared through CVD growth and mechanical polishing [103]. Membranes can be etched to $< 10 \text{ nm}$ thickness and transferred to other substrates as will be shown in Chapter 4. Continued etching will result in a lateral reduction of the membrane due to the wedged profile as demonstrated in Figure 2.14.

AFM measurements of the membrane's surface roughness were used to characterise the potential for integrating over planar optical devices without the need for inter-layer adhesives. An AFM tip with typical tip radius of 8 nm, resonant at 325 kHz, was used for these measurements and it was found that a reduction in the r.m.s. roughness, from an as received diamond chip to a thinned diamond membrane, of 1.8 nm to 0.4 nm was achieved - measured each time over a $10 \mu\text{m}^2$ area and shown in Figure 2.15.

In summary, this chapter has detailed a method by which successful fabrication, handling, characterisation, and integration, of thin diamond membranes with low surface roughness can be achieved. Membranes of down to $< 1 \mu\text{m}$ thickness were fabricated and shown to have a wedged profile of $\sim 4 \mu\text{m}$ across 2 mm. At this thickness, large areas of the diamond are thin enough to experience the necessary

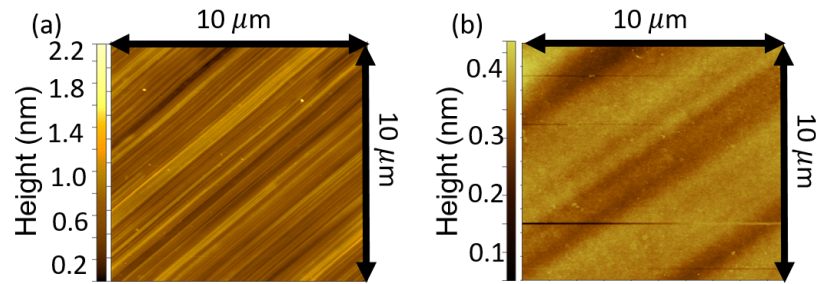


FIGURE 2.15: a) An AFM measurement on a $10 \mu\text{m}^2$ area for an as received diamond chip post-CVD growth, and mechanical polishing - r.m.s. roughness of 1.8 nm. b) Shows the same diamond after 3 hours of Ar-Cl₂ plasma thinning with an r.m.s. roughness reduced to 0.4 nm over a similar $10 \mu\text{m}^2$ area.

stresses for deformation over surface features, enabling integration with capillary-assisted (adhesive-free) bonding to a silicon on insulator device - discussed later. The lower thickness side of the diamond is also comfortably within the vertical criterion for single mode only support at telecommunication wavelengths. Low surface roughness values were also shown of 0.4 nm r.m.s. over $10 \mu\text{m}^2$ that will promote a large surface area of contact between the diamond and target substrate thus a large surface area of diamond experiencing the attractive forces required to bond the membrane non-adhesively.

Chapter 3

Bonding of thin film diamond membranes to integrated optical devices for evanescent field coupling

The hybrid integration of a single crystal diamond membrane with on-chip optical resonators is detailed in this chapter. Such a hybridised device has the potential to service many applications, spanning non-linear optics to quantum photonics using embedded colour centres. Electronic grade single crystal diamond is limited in dimensions by the size of the seed crystal that is used to grow it - nominally $\sim 4 \times 4 \text{ mm}^2$. This has impeded its use in large photonic integrated circuitry which calls for wafer size dimensions [33]. Several different methods have aimed to overcome this impediment, such as by patterning GaP membranes on diamond [52, 53, 54, 55], or fabricating diamond devices on SiO₂ [12, 62, 64, 79, 15] - with these techniques relying on polymer tapers extending the diamond waveguides; or vertical grating couplers as a means to couple light on and off the diamond. Other notable attempts to utilise diamond in photonics have included 2-dimensional photonic crystal structures [69, 66, 104, 105, 106], and diamond

nanopillars [75, 71]. All of these are impressive works, however by combining free-standing diamond membranes with established wafer-scale technologies, such as silicon, the desirable properties of diamond can be utilised whilst not limiting the chip size [78]. Further motivating this approach, is that the well known issue of SCD chips having a wedged thickness is irrelevant from an optical point of view - the devices can all be fabricated on established wafer template technologies and interact with the diamond evanescently. In this work a membrane is fabricated using the techniques described in Chapter 2 and is integrated with a silicon resonator device using a capillary-assisted bonding technique. The mechanical and optical properties of the diamond-silicon interface are characterised and compared with mode simulated results. A hybrid resonator device with a low added loss of 10 dB/cm was achieved and a group index dispersion dependent on the modal confinement within the diamond is shown.

3.1 Device design and simulation

3.1.1 Silicon resonator devices for hybrid integration with diamond

Diamond has a large transparency wavelength range due to its large bandgap, enabling its integration with guided wave applications on a number of different platforms [6]. The platform choice is driven by its corresponding wavelength transparency range and where on the spectrum a given application might be relevant, e.g. GaN is transparent in the visible wavelength range and has a refractive index similar to that of diamond - thus it might be used for interaction with NV defect centres which emit at 637 nm. Investigating the viability of hybrid devices assembled through capillary assisted bonding, the achievable optical quality of the bond was of the utmost of importance. For this reason silicon, a well established photonic foundry, was chosen as the target chip with which a thin diamond membrane would be integrated. Silicon provides a low loss well

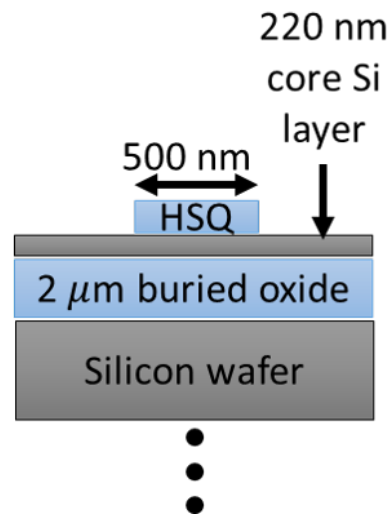


FIGURE 3.1: A schematic showing the layer stack of an SOI wafer ready to be etched for fabrication of 500 nm wide waveguides.

understood platform with which the effects of the bonded diamond would be easily identifiable and characterisable. It is also compatible with applications such as Raman lasing and non-linear photonics in the near to mid IR wavelength range, however the methods developed are applicable to other photonic platforms.

The silicon devices in this work were fabricated at Glasgow University using a commercially available silicon on insulator (SOI) wafer with a 220 nm core layer on a 2 μm buried oxide layer. The waveguides were designed to be 500 nm wide and were patterned using a 200 nm thick e-beam curable, silica-like, HSQ resist. A depiction of this is shown in Figure ???. SU8 photoresist was used for spot size conversion tapers between the guides and external injection fibre to reduce insertion losses [107]. All of the measurements reported were taken from an all-pass ring resonator geometry and over telecommunication wavelengths (1510 - 1560 nm) as these structures are favourable for characterising optical quality of devices. Wavelengths that are resonant with the cavity result in a drop of the transmission intensity measured from the output facet of the bus waveguide, as demonstrated by the schematic in Figure 3.2. It should be noted that a small

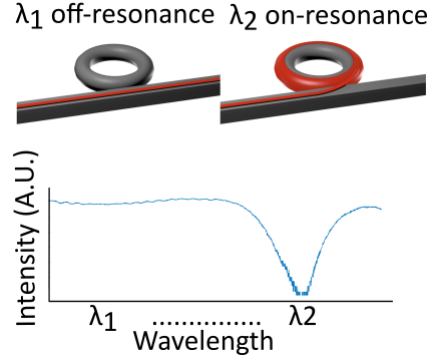


FIGURE 3.2: A schematic showing how transmission spectra would vary as the injected wavelength becomes resonant with a nearby ring cavity.

amount of light couples back from the resonator to the bus waveguide but for clarity in the schematic this has been omitted.

By a least squares method, each transmission peak is curve fitted to the analytical solution of an all-pass ring resonator [108]. From this, coupling coefficients, quality factors and distributed losses can be extracted - the power cross-coupling coefficient (κ) and power attenuation coefficient (α) are used as free parameters with their relationships detailed below. The group index ($n_g = n_{eff} - \lambda_0 \frac{dn}{d\lambda_0}$), and the Q factor ($Q = \frac{f_0}{\Delta f}$) are calculated using measured values of the central frequency and linewidth of cavity resonances and knowledge of the effective index of the mode, which can be estimated using mode simulations. The analytical expression which the measured data is fitted to is the power transmission intensity equation shown below [108, 78]:

$$T = \frac{I_{pass}}{I_{input}} = \frac{a^2 - 2ra \cos \phi + r^2}{1 - 2ar \cos \phi + (ra)^2} \quad (3.1)$$

where a is the single-pass amplitude transmission, and defined in terms of α for the mode as follows: $a^2 = \exp(-\alpha L)$. r is the amplitude self-coupling coefficient and its complimentary parameter is the amplitude cross-coupling coefficient defined as k . For a lossless system, $r^2 + k^2 = 1$ and $k^2 = \kappa$. The parameters of a , r , and k

are depicted in Figure 3.3. ϕ is the single-pass phase shift, which is the product of the propagation constant and round trip length, β and L respectively. The FSR

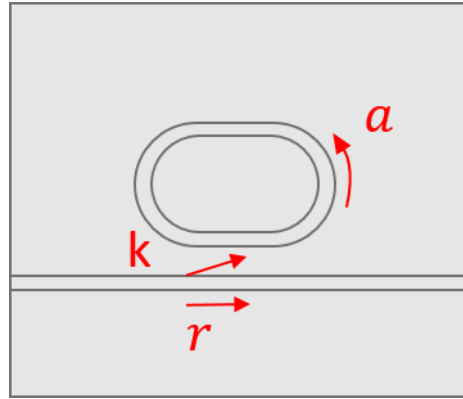


FIGURE 3.3: Schematic of a racetrack resonator showing power cross coupling, transmission, and loss parameters.

is the wavelength spacing between adjacent resonances and can be approximated as, $\frac{\lambda_0^2}{n_g L}$, where λ_0 is the wavelength of light, n_g is the group index, and L is the length for 1 round trip of the optical cavity - in this case $2\pi R + 2L_c$, where L_c is the straight coupling section of the racetrack. For the results presented in Section 3.3.2, the ring resonators were designed to have a bend radius of $50 \mu\text{m}$, in a racetrack geometry, with a straight coupling section of $41.2 \mu\text{m}$. Each racetrack can then be offset with their respective bus waveguide's coupling section allowing for variation of the coupling lengths of several nominally identical devices. An investigation into the required coupling length for the critical case of power cross coupling coefficient can thus be conducted [109].

3.1.2 Simulation of modal confinement

Three different device geometries were investigated to demonstrate the difference modal confinement would have on such things as the Q-factor, power cross coupling coefficient, and dispersion of the device. These three cases were (1) for the device alone, wherein the HSQ cap used to pattern the Si device was still

present; (2) diamond bonded onto that HSQ capped device; and finally (3) diamond bonded onto the silicon device after the HSQ cap had been removed. For the experimental measurements, the HSQ cap removal was achieved by treating the device using a CHF_3 reactive ion etch (RIE), which also etched the SiO_2 substrate and left the Si devices on a plinth of the substrate. The three cases are depicted by cross-sections of the simulations in Figure 3.4.

The electric field intensity present within the diamond from the guided modes of the silicon waveguide were investigated to form a reasonable estimate on whether or not there would be an experimentally measurable difference in the hybrid devices' optical properties. To achieve this, the solutions of a commercial-grade finite difference eigenmode (FDE) solver and propagator were used [110] to calculate the supported modes for the the silicon waveguide's cross-sectional geometry, and for the two separate cases of diamond membrane bonding - with and without the HSQ cap. The FDE method solves Maxwell's equations for the cross-sectional mesh of the simulation window calculating the spatial profile and frequency dependence of the supported modes. These solutions can give the mode's electric field and power profiles, effective index, and radiative loss. The power overlap from the guided silicon mode into the diamond were calculated and are shown in Figure 3.4, where it can be seen that the silicon waveguide nominally should have 71% of the power distributed within it, and when the diamond is bonded to the device, whilst the HSQ cap is in place, very little power enters the membrane. After removal of the HSQ cap and the simulation adjusted to have the diamond bonded directly to the silicon, there is an increase to 13 % of the modal power within the membrane.

Further information can be obtained from the simulations by finding the solutions for a range of wavelengths, the group index of the hybrid device can then be calculated and compared with the experimental measurements - showing how the dispersive properties of the device change as a result of the bonded

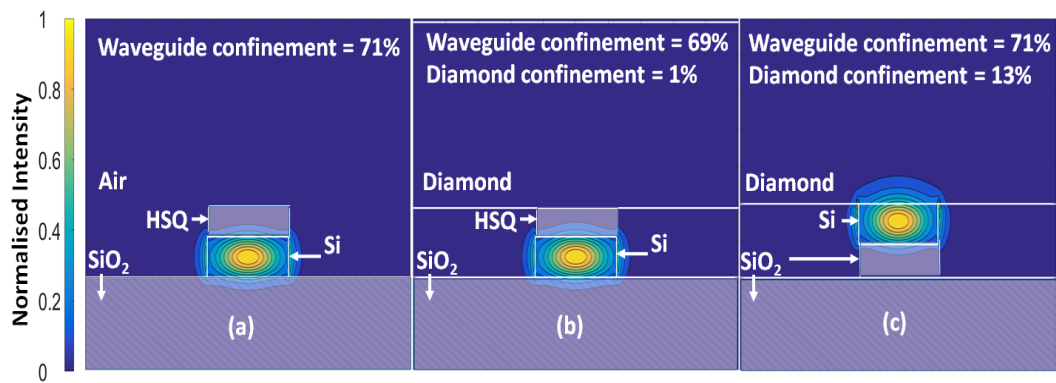


FIGURE 3.4: Cross-sectional mode simulations showing the modes' power distribution for the three cases of: Si device alone, Si device with diamond bonded and a buffering cap, and Si device with diamond bonded and the buffering cap removed through RIE.

diamond. For the same mode number there exists several wavelengths equally spaced, by the FSR, defined earlier in Section 3.1.1 as $\frac{\lambda_0^2}{n_g L}$. The FSR of a given mode however, is not exactly periodic due to its dependence on the material's dispersive properties, i.e. the group index, defined as $n(\lambda) + \lambda \frac{\delta n}{\delta \lambda}$. The group index changes for different wavelengths due to different frequency components of the pulse envelope having different phases. As the light propagating through the waveguide experiences a different effective index, e.g. by a diamond membrane being proximal to it, the dispersive properties will also change and lead to different values of group index. The simulated group indices for the three discussed device geometries are shown in Figure 3.5. It can be seen that the group index decreases from ~ 4.4 to ~ 4.3 when the diamond is contacted with the device; as the diamond changes the cladding of the nominal silicon-HSQ-air material stack. This in turn changes the distribution of the mode field, reducing overlap into the SiO_2 substrate and increasing slightly the overlap into the diamond. When the HSQ is removed from the silicon and the diamond is contacted once more, the simulations show an increase to the power present within the diamond up to 13 % and this is reflected by a further decrease in group index down to ~ 4.05 . In each case as the power of the mode profile overlapped more greatly into

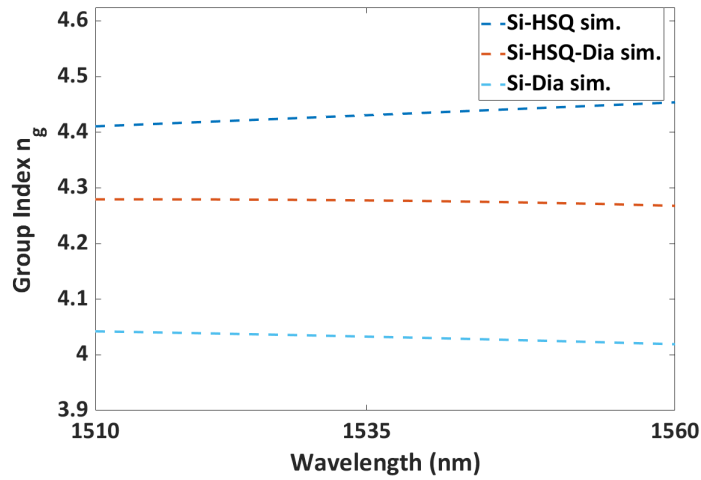


FIGURE 3.5: Simulated group index values for the three device geometries of Si-HSQ, Si-HSQ-Diamond, Si-Diamond.

the diamond a decrease in the gradient of the group index change was also found.

3.1.3 1 μm Diamond Membranes

Diamond membranes were prepared as detailed fully in the previous Chapter. Diamond chips were sourced commercially and laser diced and mechanically polished into separate smaller pieces of a few mm^2 and $\sim 30 \mu\text{m}$ thickness. Each platlet was cleaned of organic contaminants using piranha solution ($\text{H}_2\text{SO}_4:\text{H}_2\text{O}_2$ in a ratio of 3:1); and thinned down using an Ar- Cl_2 plasma etch chemistry. Using vertical scanning interferometry and stylus profileometry the thickness of the diamond was monitored until an approximate thickness of 1 μm was achieved. The thickness was chosen as a trade off between mechanical robustness and a membrane thin enough that the intermolecular forces between the target substrate and the diamond could apply enough stress to deform the membrane over surface roughness or detritus and increase the surface area of the materials in close contact. This increases the amount of diamond that would be close enough to

experience the attractive forces that fall off rapidly beyond a few 100 Angstroms [89, 111].

3.2 Liquid assisted bonding of diamond with Si devices

The diamond film was integrated with the target silicon devices by using a capillary-assisted bonding method. The target device was prepared with a droplet of isopropyl alcohol and the diamond brought into contact and transferred from a wetted corner of cleanroom wipe. Capillary forces form a liquid bridge between the two surfaces and as the liquid evaporates, assisted by a nitrogen gun, brings the membrane into close contact with the device promoting the adhesion from close intermolecular forces such as van der Waals [89, 111]. Having been pre-thinned to a target thickness of around 1 μm at its thinnest end, and with care in alignment, the diamond membrane deforms over the devices as shown schematically in Figure 3.6. Nothing other than the capillary forces detailed were used in adhering the diamond to the silicon device.

3.3 Measurements and characterisation

To determine the quality of the interface between diamond and the silicon device a number of complimentary techniques were used to investigate both the mechanical and optical properties of the hybrid device.

3.3.1 Deformation of the membrane

The physical deformation of the diamond can be directly observed using scanning electron microscopy (SEM) with a stage tilted view of the diamond edge bonded over a bus waveguide. A micrograph was taken, shown in Figure 3.7, where planar contact with the top of the silicon waveguide and the surrounding SiO_2

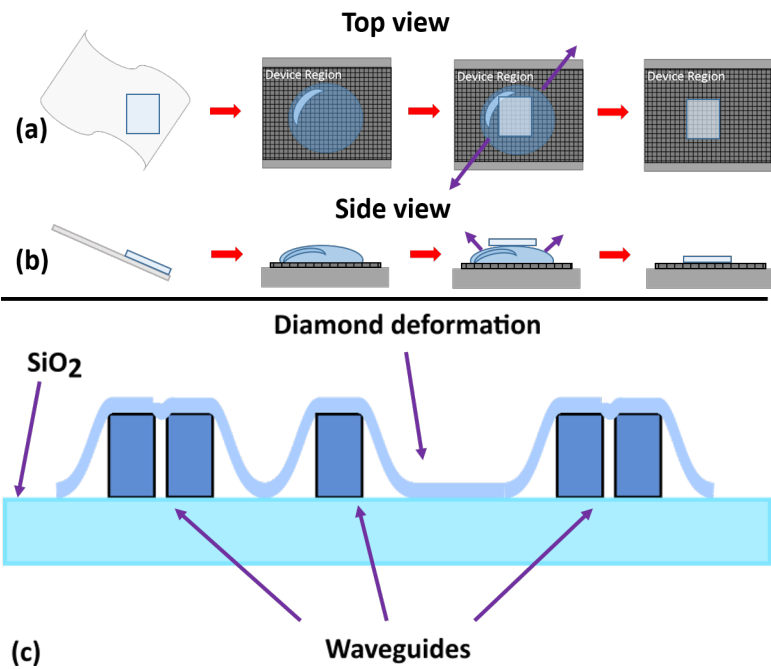


FIGURE 3.6: a) & b) Schematics of the diamond membrane bonding procedure onto a processed silicon photonic chip, from a top and side view respectively. Bonding of the materials is facilitated by capillary action bringing the surfaces into contact. c) A cross sectional schematic of how the diamond membrane conforms over and bonds with the target Si device.

substrate can be seen - a close distance of approximately $10\ \mu\text{m}$ either side of the device. This shows that, for a diamond membrane of $1\ \mu\text{m}$ deforming along one dimension over a $220\ \text{nm}$ ridge, that a good diamond-silicon interface is possible. A demonstrable pitch of devices is thus approximately greater than $20\ \mu\text{m}$ to allow for planar bonding on top of the devices and on the substrate in-between. SEM is

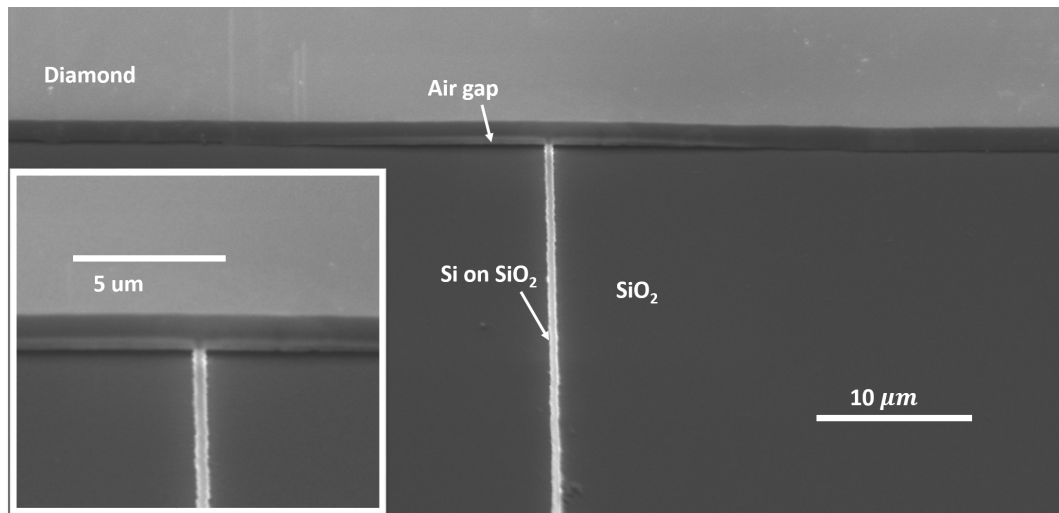


FIGURE 3.7: An oblique-view SEM image showing the bonding of a $1\ \mu\text{m}$ diamond membrane to a Si bus waveguide; it can be seen that the diamond conforms back to and contacts with the substrate within a few micrometres. *Inset*: Enlarged image at the site of the interface showing the gap between the membrane and substrate.

however unsuitable for investigating the interface of the two materials at the site of the resonator due to the opacity of diamond using this technique. For that reason an analysis of optical interference fringes using Newton's rings theory was also conducted. The diamond had visible on its surface dark and bright fringes, resulting from the reflected light between the two surfaces having different optical path lengths. Thus they have different phases which add together constructively or destructively. The bright and dark fringes can be correlated with odd or even multiples of $\lambda/2$ respectively as shown in Figure 3.8 - from this the heights of membrane separation can be inferred. A microscope image at 20x magnification shown in Figure 3.9 b was used to map the membrane height across the device. By

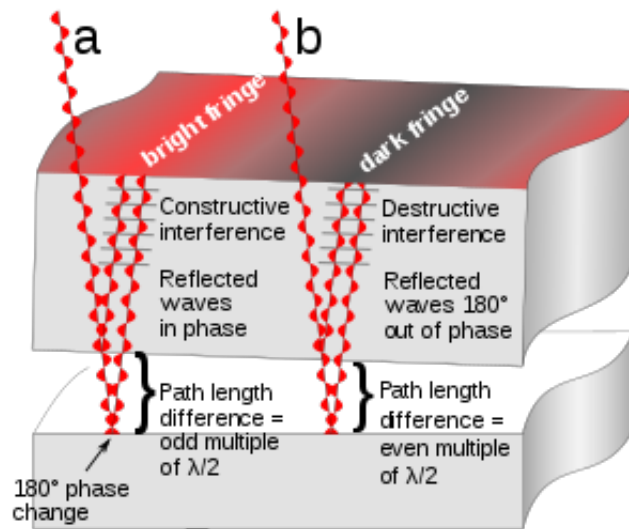


FIGURE 3.8: Schematic showing how optical interference fringes are created by an optical flat [112].

assuming a collimated monochromatic light source, we can calculate the height of the membrane separation from the device substrate - using the wavelength of the light, and the number of interference fringes counted from the central contacted point between the diamond and silica substrate. Height values, d , were calculated for each maxima and minima point of the interference fringes as $d = n \frac{\lambda}{4}$, where n is an integer number. Additionally, points at the fringe full-width-half-maxima were used to calculate height values equal to $m \frac{\lambda}{8}$, where m is an odd integer number. This data can be seen in Figure 3.9, which also shows an approximate height morphology using a smoothly varying function fitted to the known points - the black vertical lines denote the positions of the Si waveguides. The calculated height profile shows a central contacted region within the racetrack with the height of the membrane located directly above the waveguides varying with the asymmetry of the bond. The height of the membrane then reaches a maximum over a position that may not correspond to the position of the waveguides as it was demonstrated in the SEM measurement of Figure 3.9. In that case, of a diamond membrane bonded across a bus waveguide, deformation only occurs

across one axis. In the case of the racetrack resonator the diamond is required to deform over two axes limiting the local gradient with complex dependencies on membrane thickness and the locations of surrounding surface-contacted regions. These results show that the diamond-silicon interface will have a complex variation in their proximity and that it is unlikely that the material stack is exactly that of the simulated material stack of Section 3.1.2. Optically probing the hybrid device however will allow for the calculation of group index by the methodology described in Section 3.1.1 which can then be compared with simulations to find an averaged device geometry that matches.

3.3.2 Optical probe measurements

The optical interaction, between the interfaced materials, was also investigated to determine the technique's viability for integrated optical applications. An end-fire rig, so named for its injection style, was used to couple light onto the chip, i.e. from a lensed single-mode fibre into the end facet of a bus waveguide for a racetrack resonator. The light was collected through a focusing lens and polariser into a photodetector and an IR camera shown schematically in Figure 3.10. The transmission spectra were taken for the three cases as previously detailed (Si-HSQ, Si-HSQ-Diamond, and Si-Diamond) and then fitted using the technique described in Section 3.1.1.

The three spectra have been normalised and are logarithmically plotted in Figure 3.11. From comparing the three measurement sets, a clear difference in extinction ratio and wavelength spacing of the peaks can be seen. The difference in spacing, an effect of differing dispersive properties, is quantified by calculation of the group index, plotted in Figure 3.12. The measured data is compared with the simulated group indices obtained through FDE modelling - calibrated to the as-fabricated Si devices and shown as dashed lines in the plot. The simulated data for both the silicon device alone, and the hybrid diamond device when bonded

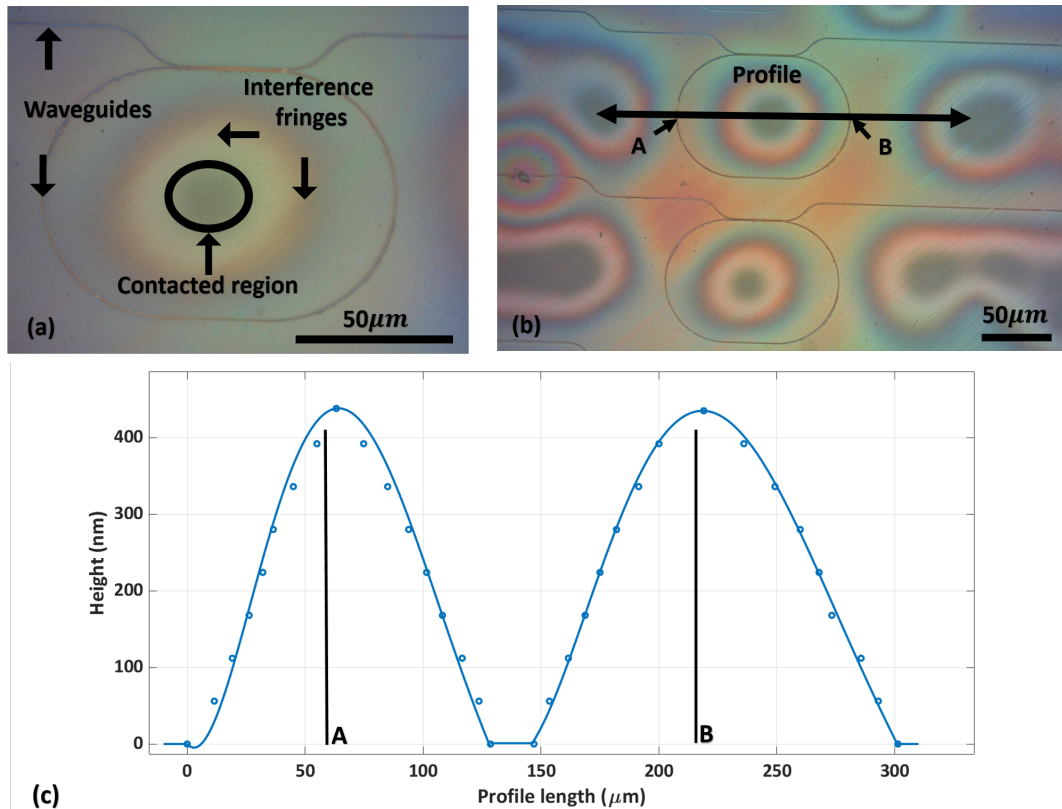


FIGURE 3.9: a) An optical image of a diamond membrane bonded over a Si resonator device showing interference fringes, a contacted region, and waveguides. b) Optical image showing the line profile on which fringe analysis was conducted to calculate the height profile over the Si device, where A and B point to either end of the waveguide resonator. c) A height profile calculated from the fringe intensity over the line profile as shown in b) with the black lines signifying the waveguide positions of the racetrack labelled again as A and B.

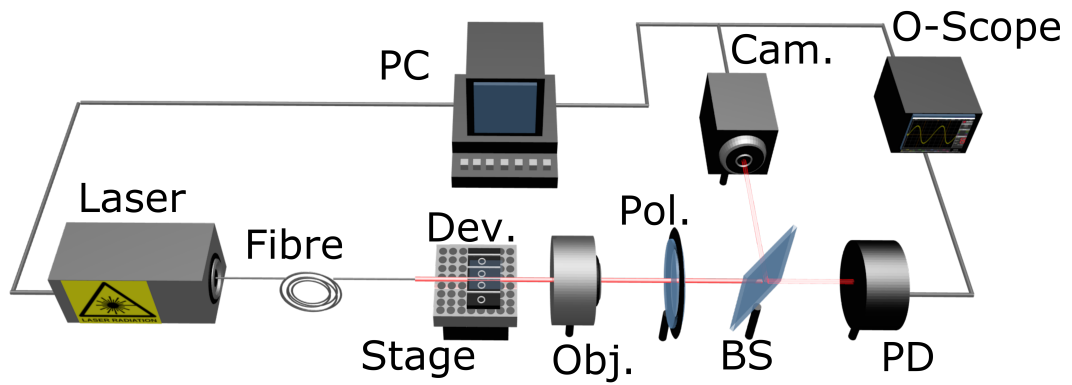


FIGURE 3.10: A schematic of the end-fire rig used to optically measure the silicon devices before and after the bonding of thin diamond membranes. A tunable laser through some polarisation maintaining fibre is coupled to the end facet of a device and the emissions collected from the exit facet using an objective. The collected light is focused through a polariser onto a photodetector and infrared camera via a beam splitter.

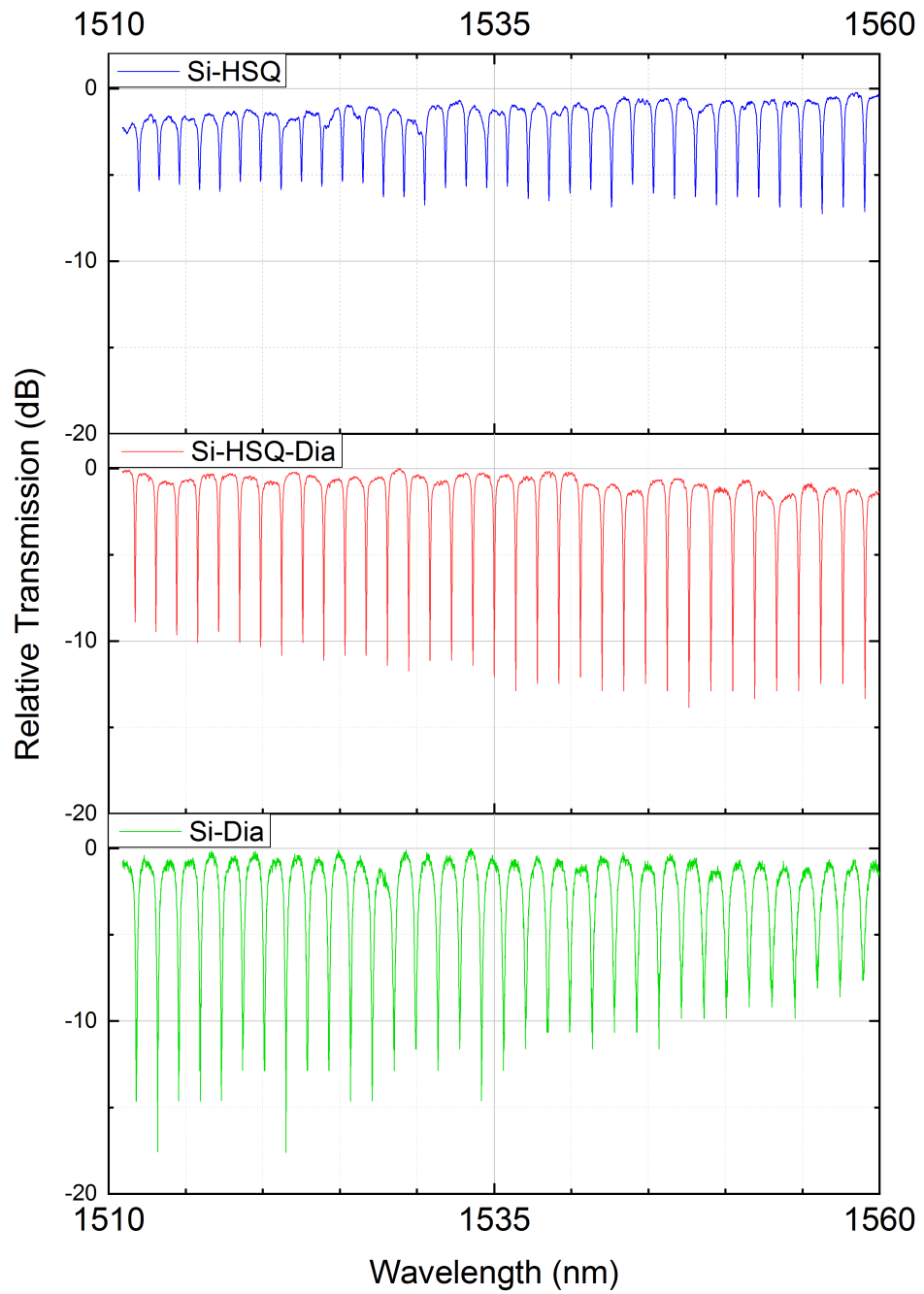


FIGURE 3.11: The normalised transmission spectra for a) the as-fabricated Si device and when bonded with the diamond pre- b) and post- c) removal of the HSQ mask cap.

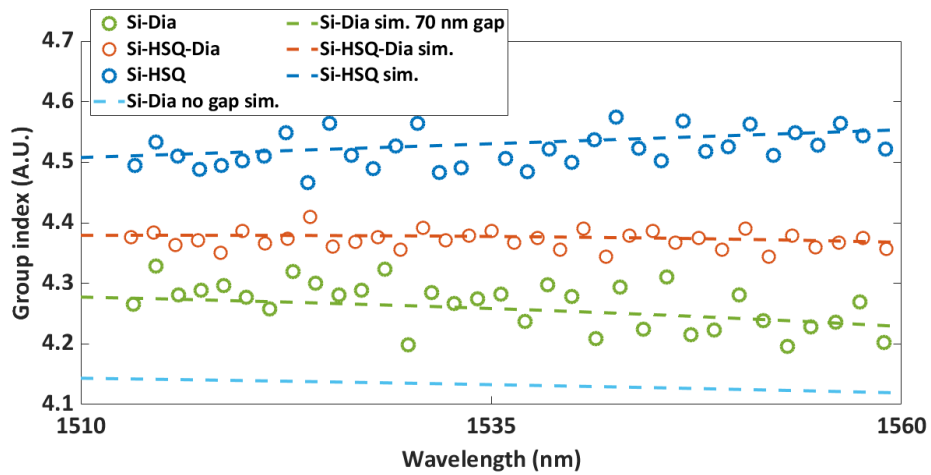


FIGURE 3.12: Extracted (circles), and simulated (dashed lines) group index values for the Si ring resonator alone, and when bonded with the $1 \mu\text{m}$ diamond membrane with and without an HSQ cap. The measured results show a group index shift and gradient in agreement with the simulated values.

atop the HSQ cap, show good agreement. Their measured group indices can be seen to follow the predicted reduction of value and gradient. The measurements for the bonded diamond device with HSQ removed, also follow the predicted decrease in group index and gradient, but the measured data is not in close agreement with the simulations. It is likely that there is a varying level of contact around the racetrack geometry which is in agreement with the optical analysis of interference fringes presented earlier in Section 3.3.1. The deformation of the diamond membrane over the resonator device, which has a complex surrounding geometry as shown in Figure 3.9, has a contact point that is off-centre and interference fringes that are asymmetric. As a result of this, the diamond-silicon contact is not fully consistent around the resonator - equivalently this can be approximated with an average air gap between the diamond and silicon device underneath. Adjusting the FDE simulations to an average air gap of 70 nm resulted in simulations that were now in good agreement with what was observed experimentally. Comparing with the hypothesised modal overlaps earlier in Section 3.1.2, a corresponding TE mode calculation - at a wavelength of $1.535 \mu\text{m}$

and 70 nm gap - is shown in Figure 3.13. The confinement values for this scenario are 70% for the silicon device and 6% in the diamond.

A second property of the resonator that allows investigation of the diamond-silicon interaction, is the power cross coupling coefficient (κ), a dimensionless value used to characterise the ratio of power coupled to the resonator from the bus waveguide and vice versa (detailed with Figure 3.3). The measurements of κ for the three cases are plotted in Figure 3.14. It can be seen

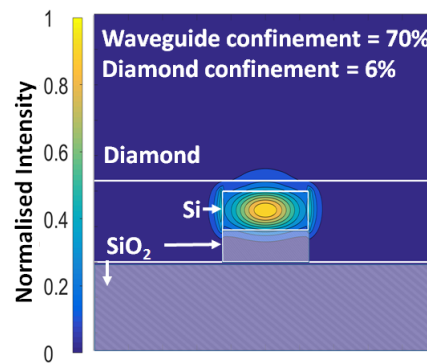


FIGURE 3.13: A cross-sectional mode simulation showing the TE modal power distribution at a wavelength of $1.535 \mu\text{m}$ for a diamond membrane 70 nm above a Si waveguide with no HSQ cap.

that when the diamond is bonded over the HSQ capped Si there is a drop in κ despite the corresponding modal overlap into the diamond - shown in Figure 3.4 - being negligible. This can be explained by the effective index of the two interfaced materials, the device now clad with diamond rather than air results in a reduced index difference vertically. This causes the mode to be drawn up into the HSQ cap, if only 1% into the diamond itself, and reduces the overlap into the shared substrate of the bus waveguide and resonator. This results in more of the mode being in a higher index difference region laterally where it is more confined and thus the observed drop in κ to the proximal resonator. For the diamond bonded without a HSQ cap present, κ increases relative to both the Si device alone and the Si-HSQ-Diamond case. There was also a wavelength dependent increase observed across the measured bandwidth. Both of these factors are explained by a larger

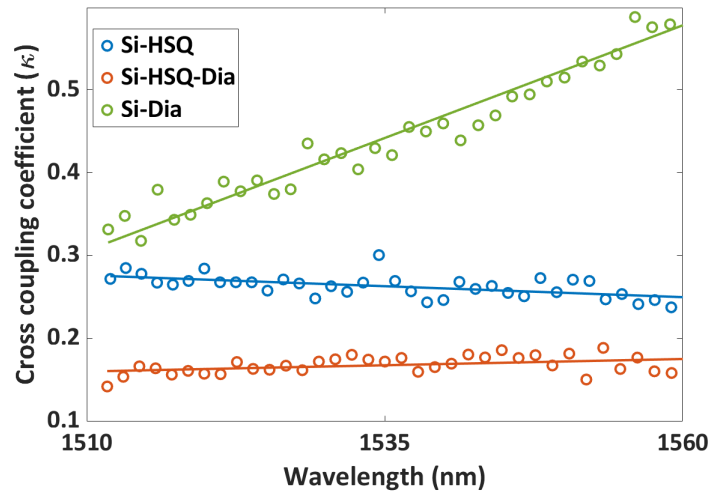


FIGURE 3.14: Cross coupling coefficients for the cases of, as fabricated Si device, and bonded to a diamond membrane with and without the HSQ cap used to pattern the device.

mode overlap between the Si and the diamond membrane. Firstly, the lateral effective index difference is decreased in this region enabling more coupling. Secondly, longer wavelengths overlap more into the diamond and facilitate an increased power transfer between the waveguide and resonator.

These results demonstrate that a free standing diamond membrane can be bonded in close enough proximity in the absence of a HSQ cladding layer that light interaction can occur between the two. This interaction on such a platform such as silicon, transparent at telecommunication wavelengths, might then be used to make use of diamond's non-linear properties, e.g. Raman shifting the light to new wavelengths.

3.3.3 Added losses

The amount of loss introduced to the system was investigated - qualitatively through observing the top scatter profile of the resonator using an IR camera, and quantitatively by looking at the loaded Q-factor of the system. The IR camera was positioned above the resonator device attached to an optical microscope and the

vertically scattered light was measured which can be seen in Figure 3.15. It can be

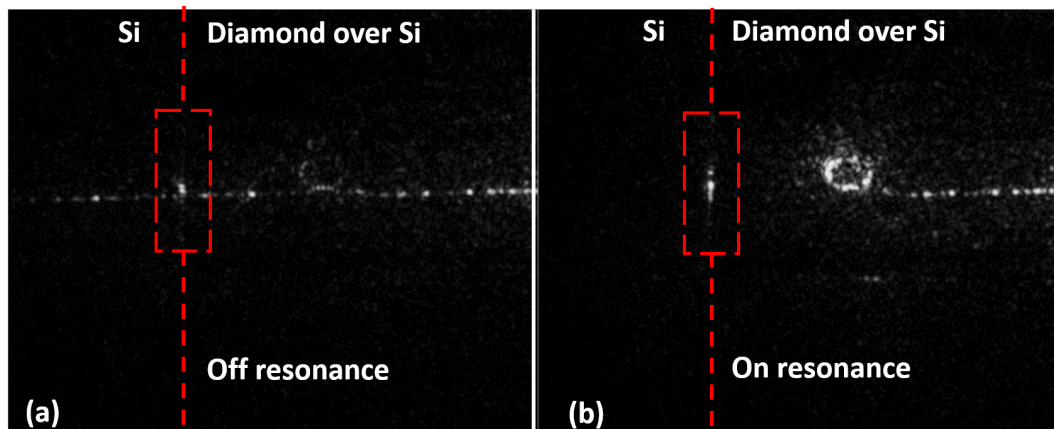


FIGURE 3.15: a) A top scattering image of a $1\mu\text{m}$ diamond membrane bonded to a Si ring resonator off resonance. The red dashed line marks where the edge of the diamond is, and the red box highlights the scattering at this edge. b) The resonator was tuned into resonance, and again with the red lines and box highlighting the edge of the diamond and scattering respectively.

seen that the amount of light vertically scattering from the waveguide alone is not discernibly different from when it is underneath the diamond membrane suggesting that the hybrid device had low added propagation losses. When the laser is tuned into resonance with the racetrack cavity however there is a large reduction in propagating light through the bus waveguide that allows a more clear view of the point source loss at the diamond edge. To quantify the added distributed losses the curve fitting method of transmission spectra (as detailed earlier in the chapter) was used and it was found that the added distributed losses for the full chip including the hybrid Si-Diamond device were 10 dB/cm. Finally, loaded Q-factors for the three cases, which are a measure of how lossy the racetracks are - including an effect of the power-cross coupling coefficient, are shown in Figure 3.16. They were found to have mean values of 22.3 k, 30.8 k, and 10.8 k for the Si, Si-HSQ-Diamond, Si-Diamond respectively. The wavelength dependent loaded Q-factor is dominated by the inverse relationship with κ for

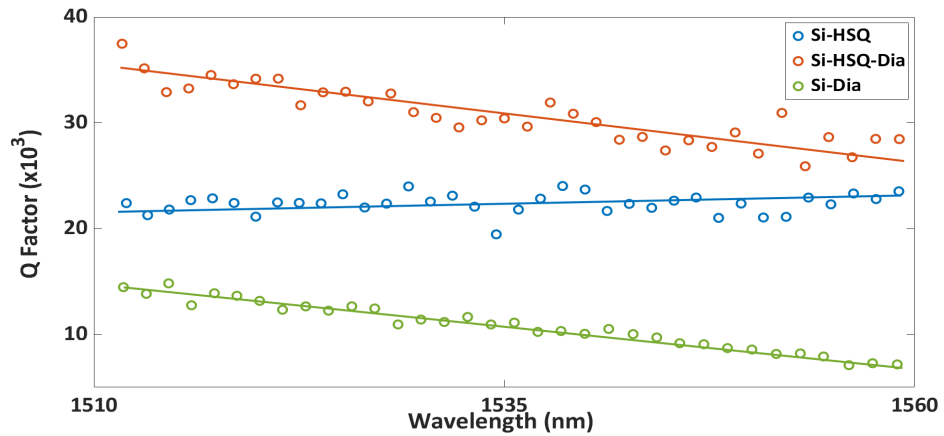


FIGURE 3.16: Loaded Q-Factor values for the cases of a silicon device alone, and bonded with diamond with and without the HSQ cap used to pattern the device. The solid lines show the general trend of the data.

each case.

3.4 Discussion and Conclusion

It has been shown that thin, free-standing SC diamond membranes, can be integrated with photonic devices fabricated from more mature platforms by capillary-assisted intermolecular bonding. The mechanical and optical qualities of the interface were investigated using SEM, optical interference calculations, and transmission spectra before and after the diamond was bonded. It was shown by FDE that the power overlap into the diamond was as low as 6%, which limits applications such as disk resonator Raman lasing (higher threshold powers) or Purcell enhancement of defect centres which scale with the spatial overlap to the cavity mode electric field maximum[113, 114]. This would require defect centres to be very close to the diamond surface where termination will greatly affect the spin properties [115]. This limitation can be lessened by fabricating higher Q-factor cavities, which lose light less quickly, and thus allow for greater interaction with even a small percentage of field overlap. Another means of improvement can be

achieved by switching to another material platform, such as silicon nitride for example, which is also transparent over the visible [116] and has a lower refractive index than diamond of ~ 2 . This would result in the cavity mode being drawn preferentially towards the higher index diamond material and give a much larger field overlap. Finally, patterning of the diamond material into resonator structures itself, before integration with other platforms, would result in the cavity mode's electric field maximum and the defect centre being very well overlapped.

For the hybrid devices in this chapter however, an optical interaction with the diamond membrane that is predictable and improvable was demonstrated. Group index measurements were conducted and compared with simulated values, finding good agreement. A low added loss of 10 dB/cm was achieved (only one order of magnitude larger than reported values from Loncar et al. but with more scope for scalability) and a Q-factor of around 10 k for the hybrid Si-Diamond resonator was found. By choosing relevant host substrate materials, and improving on the quality factors of resonator structures, this integration technique could be used for a wide range of applications spanning several wavelength ranges.

Chapter 4

Fabrication and micro-assembly of monolithic diamond optical resonators coupled to silicon-on-insulator waveguides

In this chapter a fabrication process for high quality-factor, transfer-printable, monolithic diamond devices is presented. In demonstration of this, both a tessellated-square platelet and diamond disk resonator array are fabricated, heterogeneously integrated, and characterised. Firstly, the motivation will be discussed by summarising the findings of Chapter 3, and then will continue on to discuss the fabrication process. The tessellated squares are characterised to demonstrate controllable selection of thickness when fabricating devices from a wedged diamond membrane. The optical characterisation of a diamond disk resonator printed onto HSQ clad SOI waveguides for use in non-linear optical applications is shown with average loaded Q-factors of $\sim 3.4 \times 10^4$ and intrinsic Q-factors of $\sim 9.6 \times 10^4$.

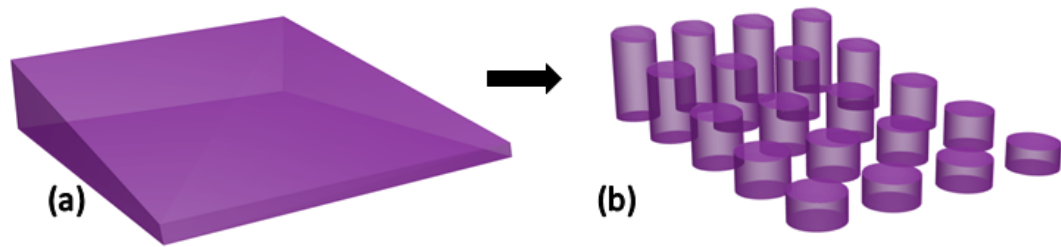


FIGURE 4.1: a) A 3D schematic showing an example of what a wedged diamond membrane might look like & b) how devices of tailored thicknesses could be fabricated from such a membrane.

4.1 Motivation

As presented in Chapter 3, thin diamond membranes can be fabricated and integrated with more established photonic platforms using capillary-assisted bonding. Diamond's desirable optical properties can thus be utilised in large area photonic circuitry - providing a solution to the limited size of optical quality diamond. Bonding large areas of diamond with any such targeted substrate however is dependent on several difficult to control factors. The wedged thickness of the membrane for example, leads to preferential bonding on the thinnest side of the chip. This is due to the the diamond deforming more easily [89, 111] over the optical devices it is to be integrated with, as well as over any remaining surface contaminant that wasn't removed during cleaning. A second repeatability issue arises due to the large overall area of the diamond - bonding several mm^2 over a series of target devices at once. This leads to unpredictable positions and numbers of bonded sites - the non-bonded material deforming in complex topologies.

It is shown that these challenges can be addressed to improve integration by first patterning the diamond. Through fabrication of smaller monolithic devices from the membrane, the wedged thickness can be utilised as a desirable attribute giving controllable selection of device thickness, as depicted in Figure 4.1. The thickness variation across a device can thus be relatively small, as a consequence of the device size itself. This is an important consideration for planar optical

devices where the mode profiles should be relatively unperturbed from one side of the device to another. Explicitly stated, it would be undesirable for a single mode supporting device to drop in thickness below the cut-off point of that mode; nor would it be desirable for it to increase in size such that it becomes multi-mode supporting. An additional benefit to fabricating smaller diamond devices is that they allow for heterogeneous integration on, or near, individual silicon devices requiring little to no deformation of the diamond that occurred in the previous chapter. Another improvement on this prior work, is that the mode will propagate fully within the diamond - the large overlap improving efficiency in Raman or colour centre enhancing applications for example. Precise fabrication is imperative for ultra-low propagation losses considering this new scheme. This integration technique also presents a means by which diamond can be interfaced with planar contact in a systematically repeatable manner.

4.2 Tessellated diamond membrane fabrication for thickness characterisation

4.2.1 Device design and transfer printing

To begin the design process for diamond optical devices, characterisation of the typical wedged thickness is required. It was thus planned to fabricate an array of tessellated squares to directly measure such variations over typical device sizes. The tessellated square array was designed to have $49 \times 49 \mu\text{m}^2$ platelets with a pitch of $50 \mu\text{m}$. Positioning of the array was orthogonal to the diamond's cleave axes to maximise device number from a single chip - this was however non-orthogonal to the direction of greatest thickness variation. A schematic depicting this for clarity is shown in Figure 4.2. The pick-up and placement of diamond platelets, as well as other devices to be discussed, was achieved through

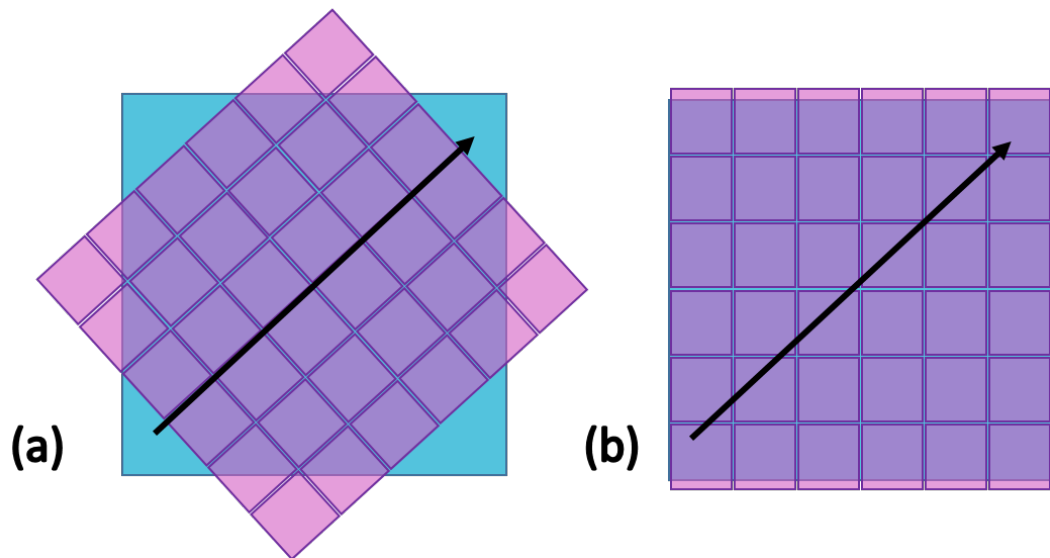


FIGURE 4.2: a) A schematic showing an example mask pattern aligned with the direction of greatest thickness variation, shown by a black arrow. b) A mask pattern aligned with the cleave axes of a diamond piece for maximising device number.

micro-transfer printing. The same technique has been used in the transfer printing of micro-LEDs [117], nanowires [118]; solar cells and DBR mirrors [119]; photodetector arrays printed on silicon transmitters [17]; and also disk resonators fabricated from AlGaAs [120]. Elastomeric polymer stamps with controllable shapes and dimensions are fabricated using polydimethylsiloxane (PDMS), specifically the product Sylgard 184, cured over lithographically designed moulds - the design tailored to suit the devices being printed. For the diamond platelets and disk resonators in this work, a stamp design was chosen with a raised plinth including pyramidal features extending from each corner and its centre, as shown in Figure 4.3. This design of stamp is fabricated by first depositing a piece of <100> orientated silicon with a SiO₂ mask and then coating it with S1805 photoresist. Four square vias are then patterned corresponding to each corner of the stamp using UV light through a commercially sourced photomask. Standard RIE silica etch recipes are used to transfer the holes into the mask layer. The sample is then submerged in potassium hydroxide acid which preferentially

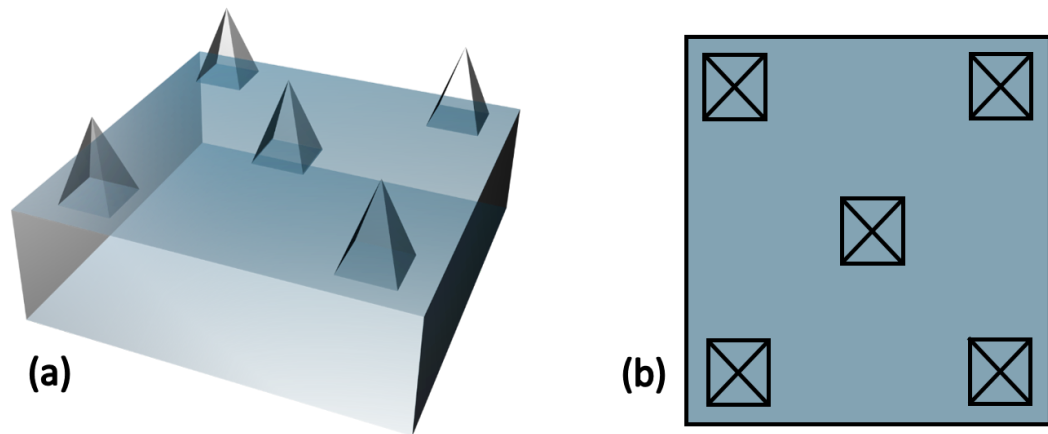


FIGURE 4.3: a) A 3D schematic of the PDMS stamp used in the printing of diamond platelets and disk resonators for this work, b) and also in 2D.

etches the $\langle 100 \rangle$ planes of the silicon and thus due to the much slower etch rate of the $\langle 111 \rangle$ plane, pyramidal holes are formed. Finally the sample is coated in thick SU-8 photoresist ($> 100 \mu\text{m}$) and one large via is opened with a pyramidal hole beneath each of its corners. This sample can then be used as a mould with which to pour the PDMS into - upon setting the stamp can be peeled from the mould and used for transfer printing.

Transfer printing is achieved by wax bonding the PDMS onto a glass coverslip which is in turn attached to a frame beneath an optical microscope. The donor and receiver chips to be used in the process are placed on a movable stage beneath the stamp and imaged through the coverslip and PDMS which are both transparent in the visible. The stamp is brought into contact with the devices (through raising the movable stage) with enough force that the roof of the PDMS collapses, i.e. the pyramids are compressed and the flat area of the stamp is fully in contact with the target membrane. The stamp is then brought away from the membrane which is now adhered to the elastomer. The defects on the stamp, without an applied force, decompress themselves resulting in a membrane which is adhered to the tips of the defects only. A target substrate is then brought underneath the stamp where

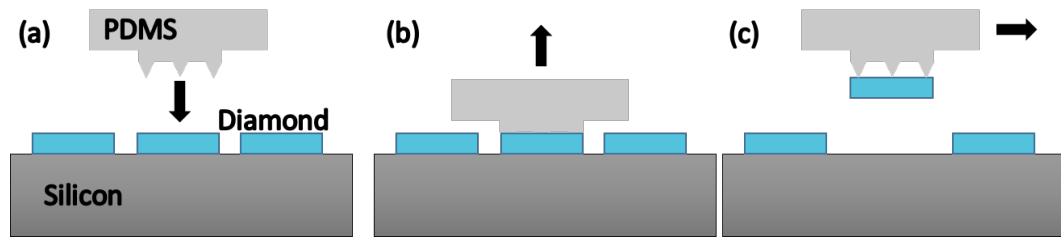


FIGURE 4.4: a) The stage is brought towards PDMS stamp, b) the pyramidal features are compressed with the device in full contact with the PDMS, c) the greater adhesion between stamp over substrate allows for removal of the diamond. Decompression of the stamp features allows printing elsewhere due to reduced contact area and thus adhesion to the PDMS.

the membrane is transferred due to a larger contact-area between the membrane and the substrate versus the membrane and pyramidal tips. A schematic of this process is shown in Figure 4.4. During a transfer printing it has been shown, that utilising a correlation alignment method, devices can be bonded over chosen planar waveguide structures with a sub-micrometre accuracy [121].

4.2.2 Fabrication and thickness characterisation of ultra-thin diamond platelets

The diamond is firstly thinned and prepared, as in the previous chapter, then transferred using a capillary-liquid assisted bonding method onto a silicon chip [78]. The diamond and silicon were coated with a 200 nm PECVD SiO₂ hard mask and then spin coated with S1805 photoresist. Using direct-write UV laser lithography, the resist can be patterned and transferred to the SiO₂ mask using a CHF₃ RIE. After removal of the photoresist using a 250°C O₂ stripping plasma, further transfer of the pattern from the SiO₂ to the diamond is achieved using a high platen power Ar-O₂ ICP etch. The etch rate of diamond in this chemistry was found to be ~170 nm/min with the SiO₂ etching at ~25 nm/min. The high selectivity in favour of the diamond reduces mask degradation, and the high platen power results in an anisotropic etch - both features culminating in good

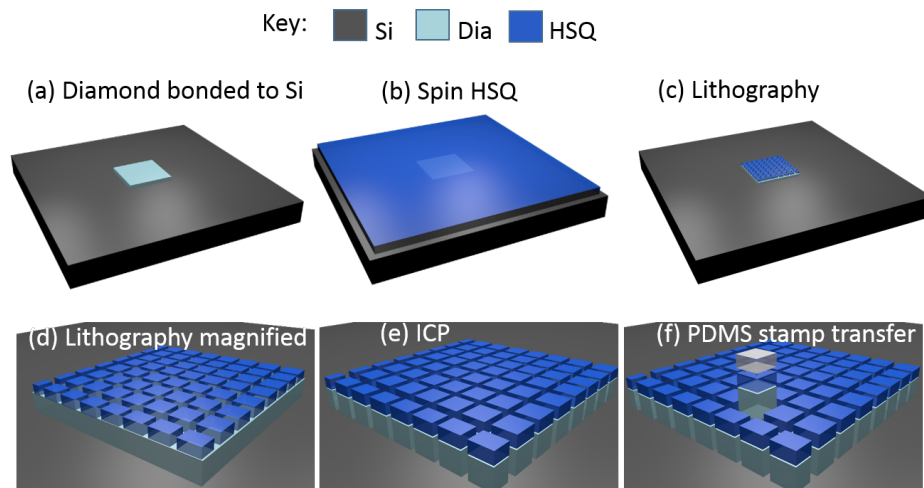


FIGURE 4.5: A schematic showing the process flow of fabricating tessellated square diamond membranes.

transfer of patterned features and low sidewall roughness. The process flow is shown schematically in Figure 4.5. The thickness was monitored using VSI and once etched below $2 \mu\text{m}$ the diamond was patterned using photolithography into an array of tessellated square platelets. The silica mask used to pattern the diamond was removed using the previously mentioned CHF_3 RIE; then the whole chip was globally thinned using Ar-Cl_2 for maintaining smooth surfaces until the thinnest edge began to recede. Several of the resulting platelets were transferred from their host substrate to a new silicon chip with a large enough pitch to comfortably measure the height of each corner using AFM. The difference between each platelets highest and lowest corners is used to determine an average change in thickness per $69.3 \mu\text{m}$. A tilted-view SEM of 4 transferred platelets as well as plots of each of their height profiles are shown in Figure 4.6

The average difference in thickness was found to be $\sim 230 \text{ nm}$. It is also notable that the smallest thickness that was measured had a value of $\sim 10 \text{ nm}$, showing that ultra-thin membranes can be integrated and manipulated by this technique with little damage. This gives a thickness difference across the entire 2 mm^2 chip of $9.4 \mu\text{m}$ which agrees with VSI measurements taken prior to the final global etch.

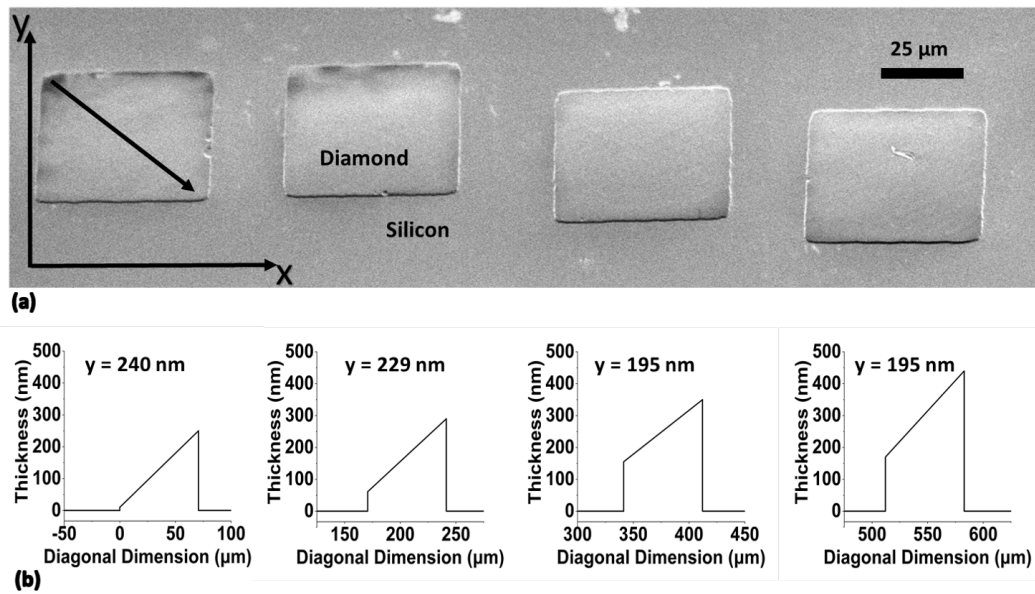


FIGURE 4.6: a) A 45 deg tilted-view, SEM micrograph, of 4 membranes that were printed for AFM measurements shown in bottom figure - black arrow across membrane indicates the direction of height profiles. b) Height profiles of the 4 printed membranes shown in the SEM image with thickness differences (y) labelled on each.

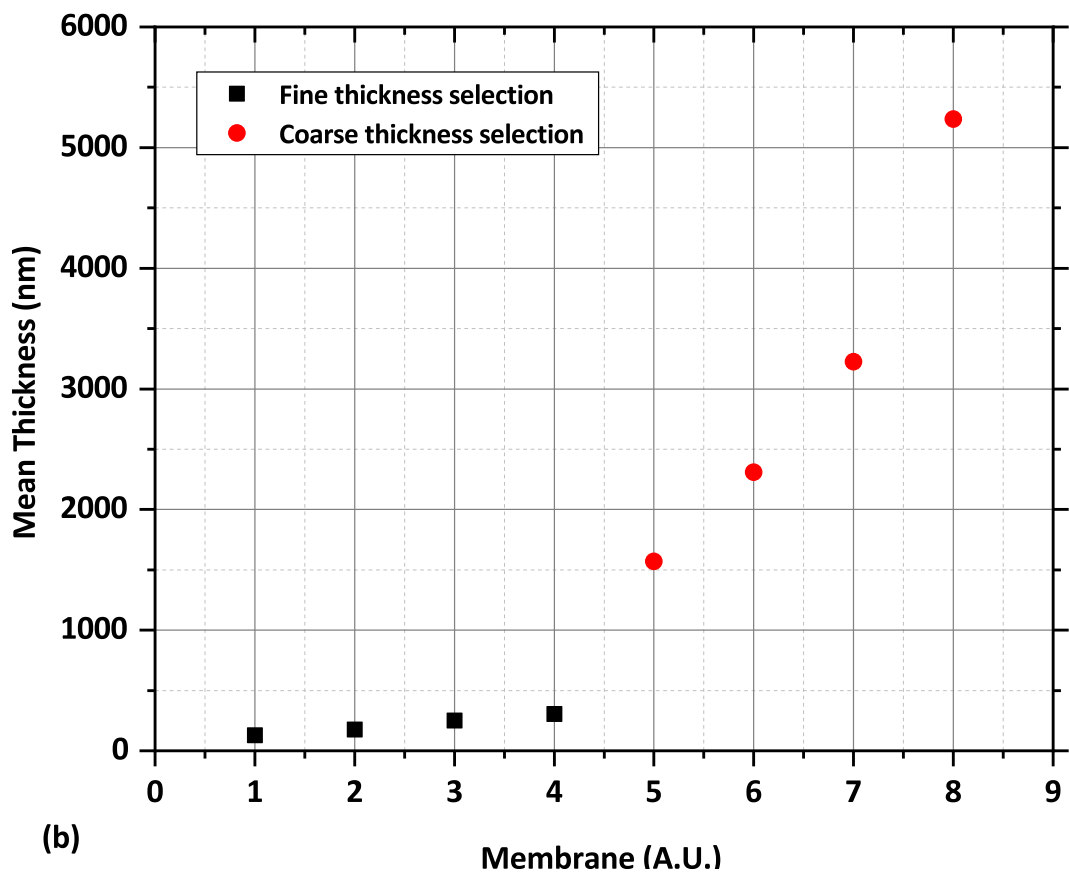
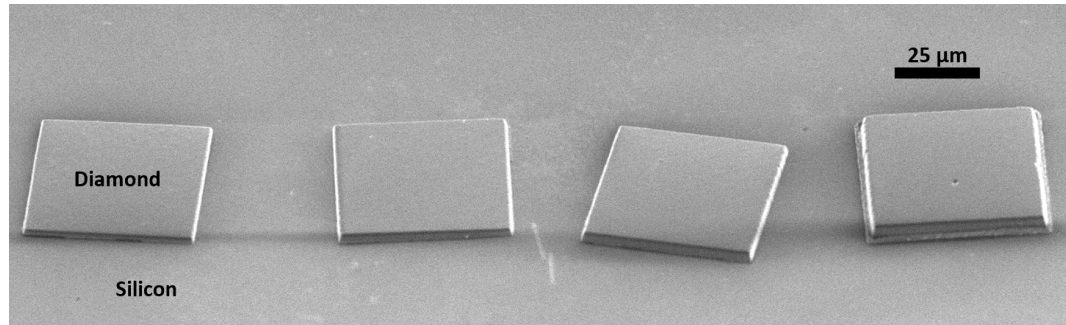
Nominally, variations in diamond thickness for diamond grown by CVD which has been laser cut and mechanically polished, ranges from $\sim 1 \mu\text{m}$ to $10 \mu\text{m}$. As such, it is thought that this is close to the worst case example of thickness variation. Despite this, over device geometries of a few 10s of micrometres, the variation would still allow for targeting a single-mode-only supporting structure. A device designed for telecommunication wavelengths for example, at the upper end of thickness variation would only have the next nearest higher-order mode solutions in a high loss regime, close to cut-off.

Coarse and fine selection of device thickness was demonstrated by selecting over the diamond area. An SEM of 4 printed membranes, with up to a thickness of $5 \mu\text{m}$, is shown in Figure 4.7. So too is a plot depicting the range of device thicknesses that were successfully printed. Depending on the refractive index, or geometry of the intended integration substrate, diamond devices of vastly varying thickness might be required. Here we have demonstrated that devices of various thicknesses and low local-thickness variation can be fabricated from a wedged diamond piece, and systematically printed for hybrid material applications. It is also possible to maximise the number of devices within a target thickness range, by printing those at specifications first and then globally thinning the remaining devices to bring them into targeted dimensions.

4.3 Diamond disk resonators heterogeneously integrated with a SOI platform

4.3.1 Device design, fabrication and motivation

Monolithic diamond disk resonators were designed to have a radius of $12.5 \mu\text{m}$ to ensure a larger ($> 10 \text{ nm}$) free spectral range - to aid in the analysis of subsequent transmission measurements. A target thickness for these devices was chosen to be



(b)

FIGURE 4.7: a) A 45 deg tilted-view, SEM micrograph, of 4 thicker diamond membranes printed for thickness characterisation. b) A plot showing the fine and coarse thickness selection from an array of diamond tessellated platelets.

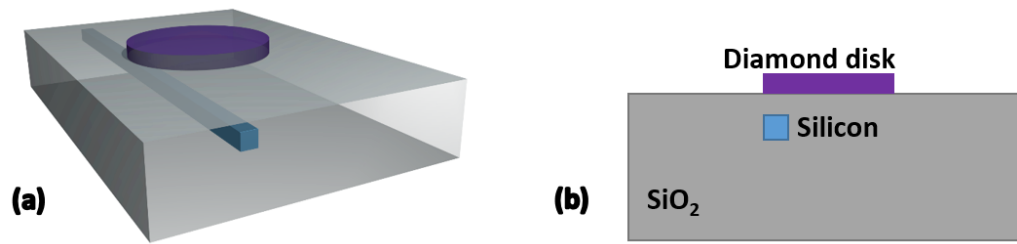


FIGURE 4.8: a) A 3D schematic of a transfer printed diamond device on a SOI waveguide platform b) as well as a 2D representation for clarity.

$< 2 \mu\text{m}$, as before to give confidence in the robustness of the chip whilst handling and lithographically patterning throughout the remaining process. The diamond was thinned and transferred as before but patterned using an HSQ e-beam resist, which itself can act as a diamond hard mask, for higher resolution patterning of smooth sidewalls. The ICP etch recipes and printing procedure were the same as detailed for the tessellated square platelets. A targeted integration platform of silicon-on-insulator was chosen, which would be of interest for optical non-linear applications. The material stack, as depicted in Figure 4.8, was for a diamond disk transfer printed onto a SOI waveguide. The silicon waveguide has a standard single mode geometry of $500 \times 220 \text{ nm}^2$ and is clad with approximately 250 nm of silica-like HSQ.

By this process, monolithic diamond devices can be fabricated and heterogeneously integrated on-demand - with application-driven platforms and full modal overlap within the diamond. This offers, beyond the state-of-the-art, the combination of desirable material platform properties whilst maintaining high mode interaction in the diamond itself - increasing efficiency of non-linear processes. Monolithic micrometre devices also overcome the bond-interface complications of integrating wide mm-scale diamond membranes shown in the previous chapter.

4.3.2 One- and two- dimensional mode solving for design of diamond resonators

One-dimensional mode solutions were numerically calculated and used to determine values of thickness for diamond at which higher order vertical modes would no longer be supported. The two-dimensional mode simulations were then used to find the first three orders of radial modes within the diamond with their effective index tracked over several wavelengths. From this, the free spectral range of resonant modes could be estimated and compared with measured data. Finally the confinement of powers from the whispering gallery modes that overlapped into an area occupied by a silicon waveguide for various lateral positions was calculated. These numbers are used to draw a relative estimation between the extinction ratios of subsequent transmission measurements and the modes that might be coupled to.

The one-dimensional mode solutions in Figure 4.9, show that for an injection wavelength of 1550 nm, the higher order modes cut-off below a diamond thickness of $\sim 1 \mu\text{m}$. The dashed line in Figure 4.9 shows a target thickness that maintains device robustness with only a few higher order vertical mode solutions remaining. The shaded box accounts for the average wedged thickness of available diamond over the typical device sizes of a few tens of micrometres. For disk resonators a second consideration is that of the whispering gallery modes along the lateral dimension. Depending on the position of a heterogeneously integrated diamond disk relative to an underlying waveguide, such as in the scenario depicted by Figure 4.8, different lateral modes will be coupled to more strongly. Two dimensional mode solutions are found for for a diamond disk at a target thickness of 1800 nm and 25 μm in radius, shown in Figure 4.10. It can be seen that the power overlap into the waveguide region for various lateral positions follows a predictable pattern, and as mentioned can be compared to the

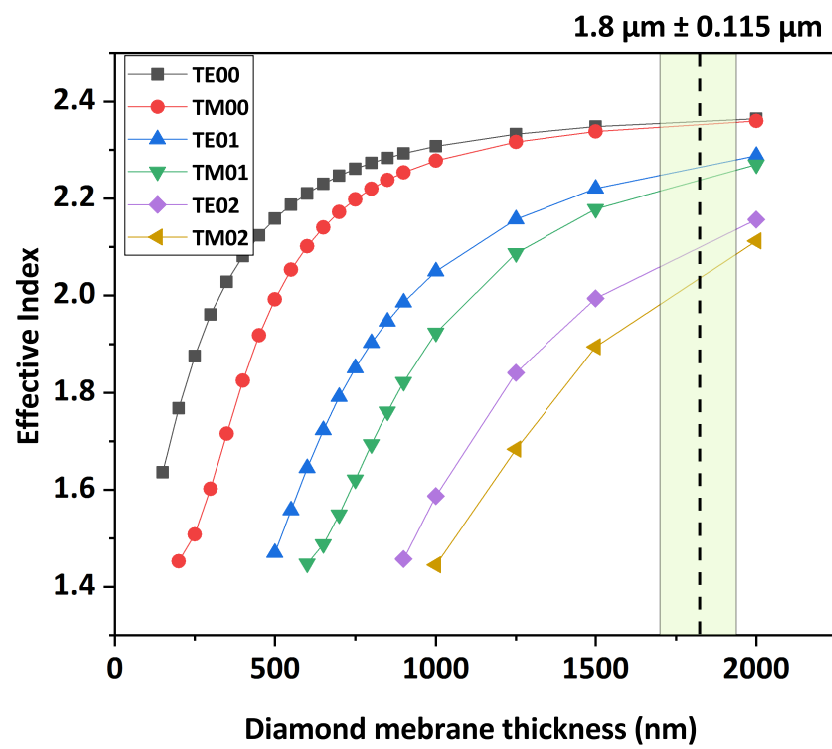


FIGURE 4.9: One dimensional mode solutions, numerically calculated, for a diamond membrane of different thickness values, bonded on a SiO₂ lower cladding. The dashed line at 1800 nm shows the target thickness, with the shaded box showing the variation in thickness due to material wedge.

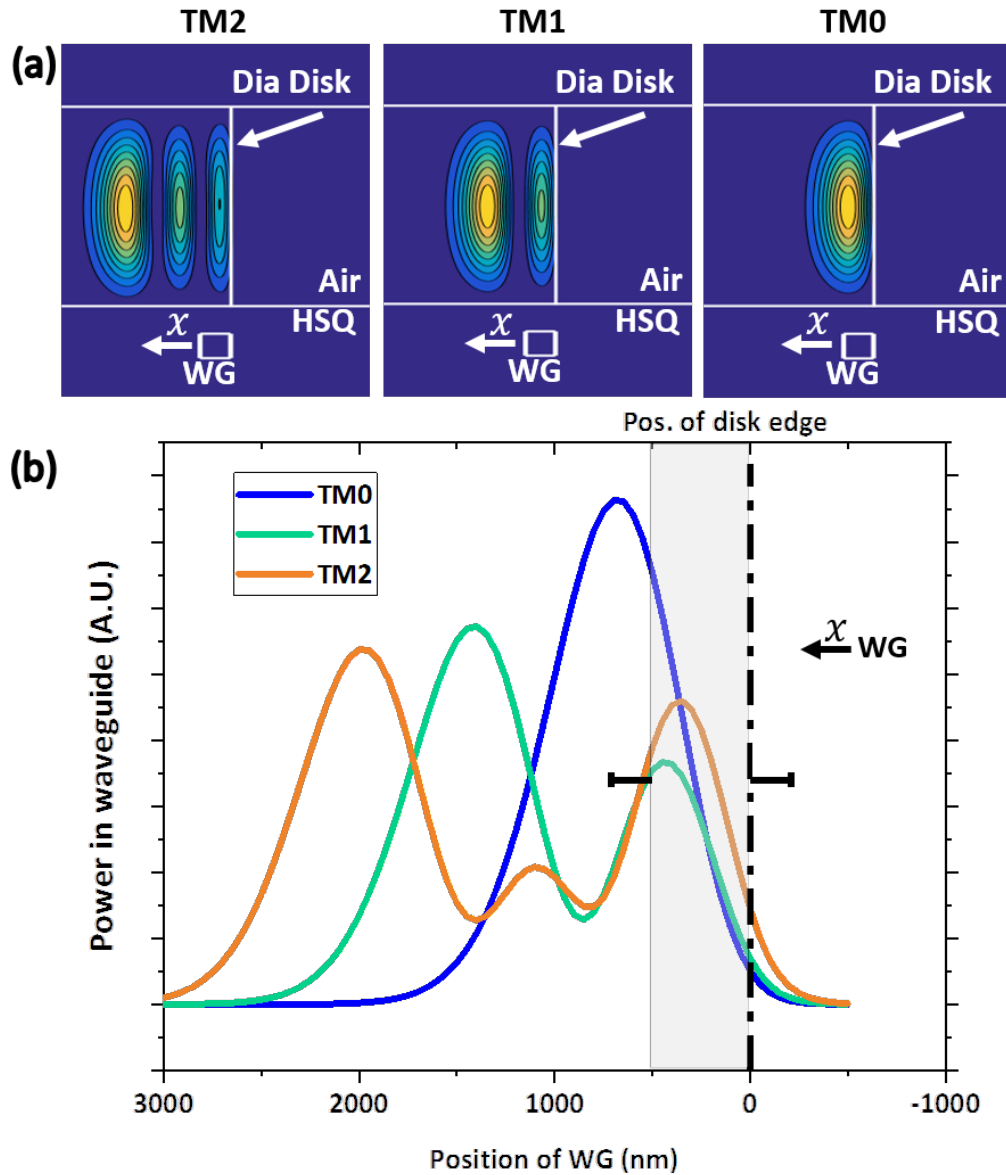


FIGURE 4.10: a) The power distributions of the first three whispering gallery modes of a diamond disk resonator with 1800 nm thickness on an insulator substrate. b) A plot of the percentage of power present in the location of a waveguide as a function of lateral position offset, x , from the disk edge.

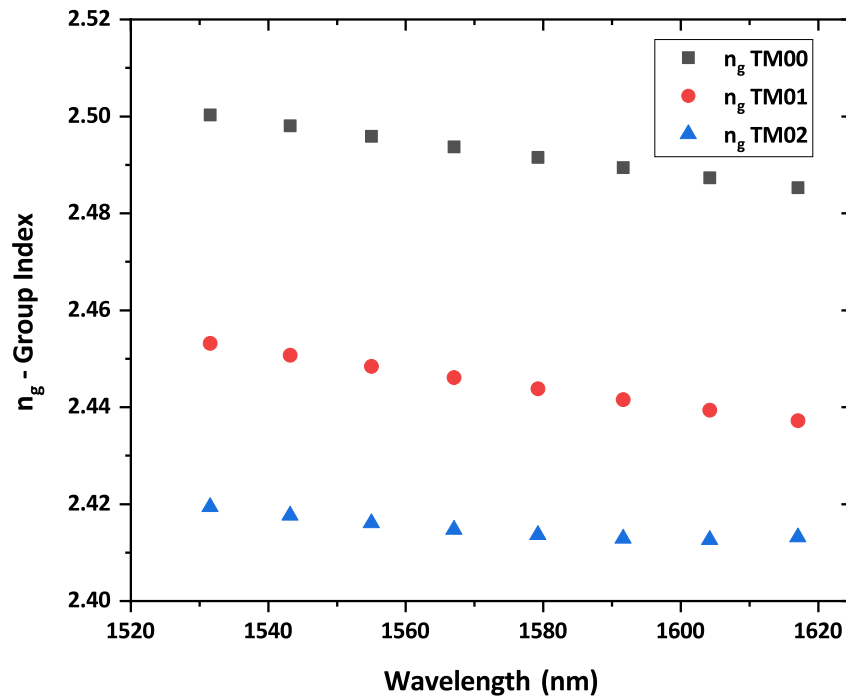


FIGURE 4.11: The group index values for the first three order TM modes calculated from effective index simulations across a wavelength range of 1530-1620.

extinction ratios of measured resonances. Thicker disk structures, such as this, however have more complex solutions with higher order modes exhibiting more than one lobe in the vertical axis. This will result in several different modes, not calculated here, that have increasing or decreasing overlap into the waveguide for different lateral positions. It was expected, and is indeed reflected in the transmission spectrum, that there would be several resonant peaks with varying extinctions and free spectral ranges.

The group index of each mode was calculated, by finding the effective index solution of that mode across a wavelength range of 1530 nm to 1620 nm and are plotted in Figure 4.11. From this group index a free spectral range is calculated for each mode, which was estimated at between 11 and 15 nm across the wavelength

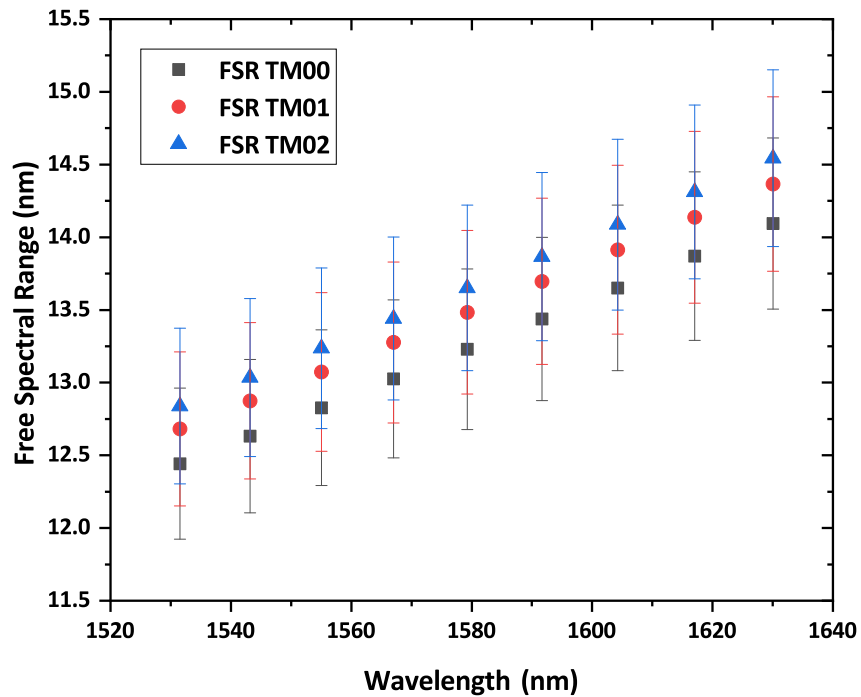


FIGURE 4.12: The free spectral range values for the first three order TM modes calculated from group index values across a wavelength range of 1530-1620.

range, shown in Figure 4.12. By comparing these results to transmission measurements of the actual devices with the same parameters, as is discussed in the results section, families of modes can be estimated to better quantify data. Using the simulations, transmission measurements of the device can be predicted and/or better analysed.

4.3.3 Optical transmission measurements of a hybrid diamond-silicon resonator

Diamond disk resonators of approximately $12.5 \mu\text{m}$ were fabricated and integrated onto SOI waveguides - as shown in Figure 4.13. The disks have been printed over the top of the HSQ clad silicon devices with the waveguide aligned

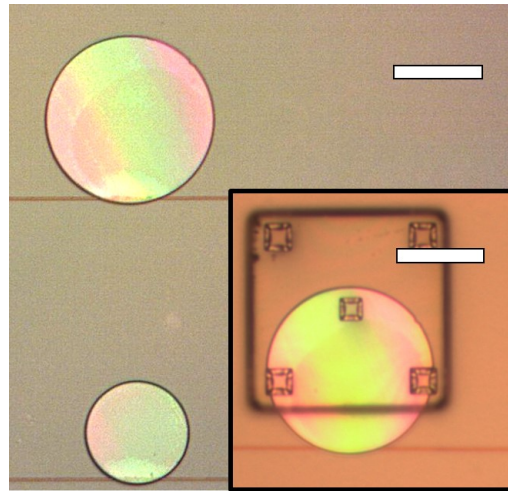


FIGURE 4.13: 45 and 25 μm radius diamond disks printed onto silicon waveguides. Inset: A diamond disk being printed using a PDMS stamp onto a HSQ clad Si waveguide. Scale bars are 90 μm .

to the diamond edge. Characterisation of the devices was achieved using a lensed fibre, end-fire rig, and the resulting transmission spectra analysed. The analysis was done by fitting each resonance to the analytical expression for an all-pass resonator device as is detailed in Chapter 3. The TM transmission spectrum for the disk is shown in Figure 4.14 where several resonances, corresponding to different whispering gallery modes of the disk, can be seen. From the fits, parameters such as the Q factors, extinction ratios, distributed losses, and power cross coupling coefficients could be calculated for each. Free spectral ranges were then estimated for three mode families. Each group was identified by looking for similarities in the aforementioned parameters and the estimates on free spectral ranges from the previous simulations - it can be seen that the three groups identified fall within the range estimated. Of the transmission spectrum itself, it is also notable that there are several large 10-15 dB extinctions which is typical of a near critically coupled system.

Average loaded Q-factors of $> 3.4 \times 10^4$ were found - with a representative example of these fittings plotted in Figure 4.15 a. Several Q-factors were also

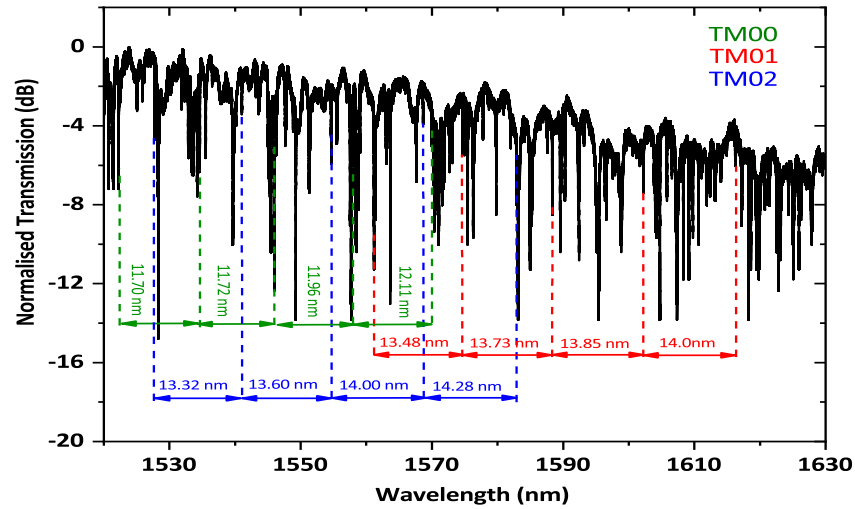


FIGURE 4.14: A normalised intensity transmission sweep from 1520 - 1630 nm at $100 \mu\text{W}$ for a hybrid diamond-silicon resonator device assembled through transfer printing. Three sets of modes are identified and their free spectral ranges labelled.

higher than this value and one of the high Q-factor resonances is plotted in Figure 4.15 b, $Q = \sim 8 \times 10^4$. These values are in line with other diamond resonator devices that have been reported, such as those fabricated on SiO_2 [79] or with GaP[52].

The power cross coupling coefficient and distributed propagation losses, that were extracted from these fits, are also plotted against Q-factor in Figure 4.16 to show the range of the device modes. It can be seen, as expected, that the modes with higher Q-factors have the lowest losses with values down to the $< 2 \text{ dBcm}^{-1}$ range - which is on-par with state of the art silicon-on-insulator devices[122]. Power cross coupling is also lower for the higher Q-factor resonances, leading to high extinctions. This is as expected for modes with low loss, as low interaction with the surface roughness would suggest a reduction in κ . The intrinsic Q factors were also calculated for each of the resonances in Figure 4.14 and it was found that there was an average value of 9.6×10^4 and a best quality resonance of 5.0×10^5 .

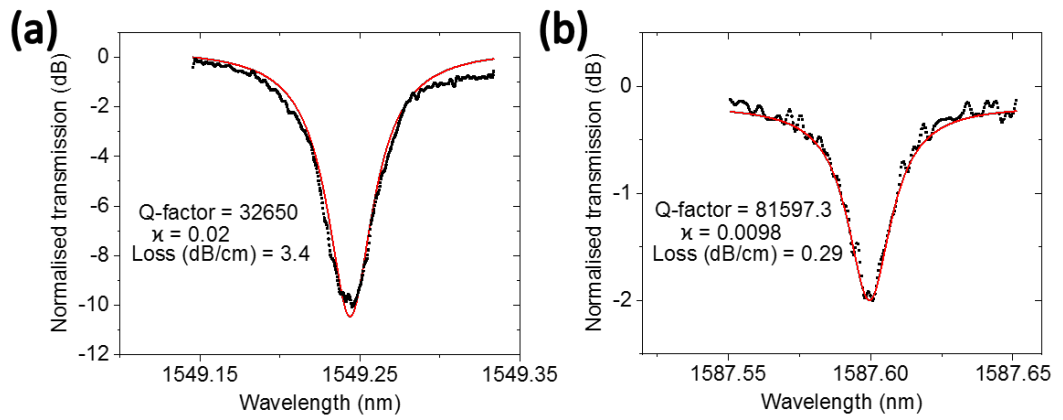


FIGURE 4.15: a) A representative resonance centered around 1549.25 nm with a calculated Q-factor of $\sim 3.2 \times 10^4$. b) A stand out resonance centered around 1587.60 nm with a high Q-factor of $\sim 8.2 \times 10^4$.

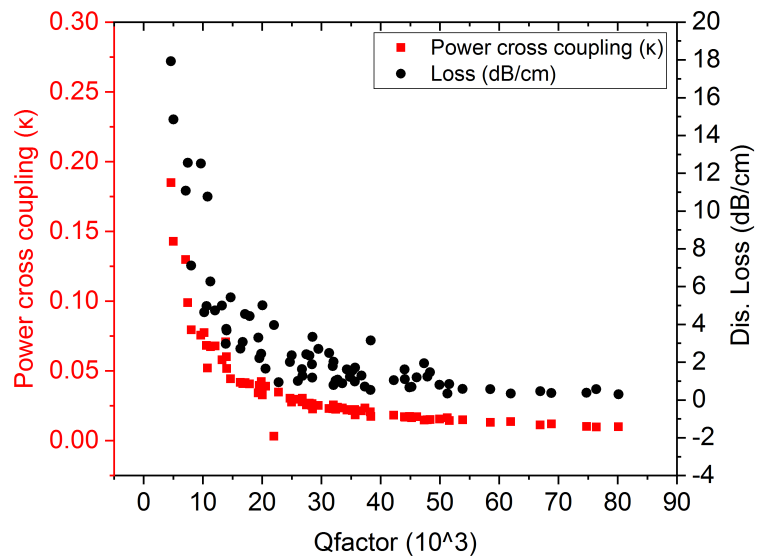


FIGURE 4.16: Power cross coupling coefficients (red) and distributed losses (black) are plotted versus Q-factor.

4.4 Conclusion

In conclusion, techniques have been developed that enable the fabrication and transfer printing of diamond devices down to 10s of nanometres thickness for heterogeneous integration. Diamond tessellated square arrays and disk resonator cavities were fabricated with wedged thickness mitigated over small device dimensions. These device sizes can be larger for diamond that has a smaller thickness gradient or has had the gradient reduced by, for example, polishing a single crystal diamond that is protruding from a polycrystalline diamond frame with higher mechanical wear resistance[103]. On-demand integration of diamond devices has been demonstrated, which can be applied to versatile, application-driven platforms. Diamond disk resonators that were fabricated and integrated with silicon waveguide devices showing intrinsic quality factors, for modes fully overlapping with the diamond, on the order of 9.6×10^4 - which is promising for diamond non-linear optics, as well as defect emission enhancement and collection. The measured resonances had losses in the low single digits of dBcm⁻¹ which is on par with other state-of-the-art diamond devices[62].

Chapter 5

Thermally tuneable diamond micro-disk resonators

5.1 Introduction

Micro-resonators are an attractive component in integrated optics due to potentially dense integration and their high quality factors, as shown in the previous chapter. They can also be used as building blocks for several different optical devices, such as wavelength filters - for wavelength-division-multiplexers [123] - all-optical switches[124]; optical delay lines[125]; biosensors [126], and more. The ability to tune a resonator's response enables its use as an active element for future optical communication [127], defect-emission enhancement, or wavelength selectivity for Raman lasing. One tuning approach, is to alter the device's effective index and thus the modal propagation constant, which in turn shifts the resonant wavelengths of the ring. Several static tuning approaches can achieve this, such as by thermal oxidation[128], or condensation of xenon gas [129, 130]. There are however a number of different dynamic methods by which the effective index can be changed, such as by electro-optical, micro-mechanical, or thermo-optical tuning - attractive due to the potential reversibility of the changes. Diamond, like other highly symmetric crystal structures, does not exhibit linear

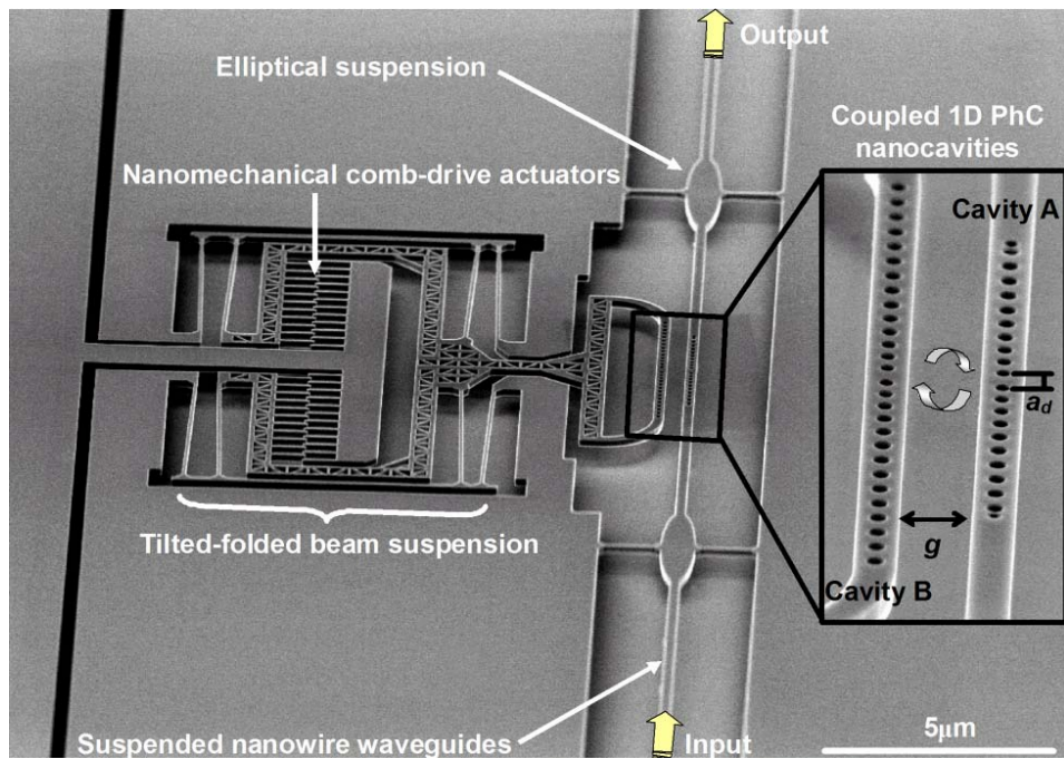


FIGURE 5.1: A micro-electro-mechanical device used for the tuning of resonant wavelengths [134].

electro-optic effects [131, 132] but does have a relatively high non-linear electro-optic (Kerr) effect [15] - this however still requires relatively high optical intensities to change the refractive index by a very small amount. Micro-electro-mechanical systems (MEMS) have been used to tune resonant wavelengths by a much larger magnitude of 10's of nm in diamond films with no significant deterioration in Q-factors [133]. An example of such a micro-electro-mechanical device is shown in Figure 5.1. The challenges associated with using these structures however, include a complicated fabrication process and devices that need to be protected from vibrations [135]. Finally, tuning by heat is something that can easily be achieved by scaling the amount of power injected to an on-chip device. The thermo-optic coefficient of diamond however is much lower than the regularly used platform of silicon - $\sim 10^{-6}$ [14] compared with

$\sim 10^{-4}$ [136] - making it more robust to optical change as a function of temperature change.

In this chapter a hybrid diamond resonator device was micro-assembled, as in the previous chapter, and its resonances were tuned using optically induced thermal energy. It is shown that a relatively large amount of heat is generated, even due to small mW powers, which is likely due to absorption from substitutional nitrogen in the diamond. This results in higher increases of temperature that are demonstrated to give up to 450 pm shifts in resonant wavelength of the 25 μm diameter disk. This value was limited by the available injection power, but with engineering of the cavity free spectral range, broadband selection of resonant wavelengths could be possible with shifts of this size. It is also shown, that the heat build-up within the diamond does not dissipate readily to the surrounding chip, likely due to the insulating HSQ cladding layer on the SOI waveguides - potentially enabling device by device tuning.

5.2 Background and Theory

5.2.1 Optical bistability

Optical bistability is of great interest in integrated optics due to its potential in all-optical logic gates, memories, and switches. Current research gives attention to investigation of different material configurations and systems, with improved non-linearities [137]; decreased component sizes for integration density, switching times, operating powers, and temperature control [138].

For a system to be called optically bistable it must have two potentially stable intensity output states for the same intensity input value. This is clearly a non-linear system as the transmitted intensity is not just a multiplicative constant times the input value - this is depicted in Figure 5.2. Assuring the non-linear transmission is bistable requires feedback, i.e. the previous state of the system

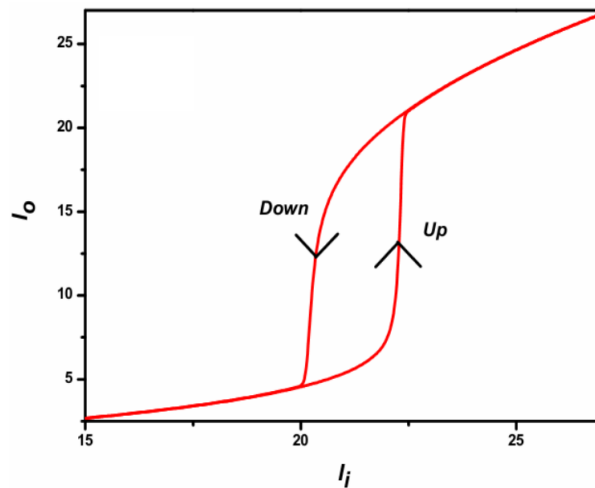


FIGURE 5.2: Hysteresis curve showing, feedback-dependent, multivalued intensity output for a range of intensity inputs [137].

determines what the measured output will be. For example, using Figure 5.2 as reference, if you ramp up the input intensity from nothing you have the “up” branch. If you begin from a higher intensity and lower the input you have the “down” branch. The non-linear transmission is multivalued, or bistable, and can be cycled completely and repeatedly through variation of the input intensity. Bistability can be classified into two systems, absorptive or dispersive, and can be intrinsic or hybrid. That is, feedback occurs either due to intensity dependent absorption or change in refractive index and both mechanisms may occur simultaneously. The system is said to have intrinsic bistability if the process is all-optical, and a hybrid one if there is an optical and electrical interaction with the material - through detector monitoring for example. The focus of this work is on an intrinsic, all-optical effect.

5.2.2 Power enhancement in a micro-ring resonator

Non-linear optical effects can be induced at reduced threshold powers through the use of resonator structures. For example the intensity within a ring or disk resonator can be comparably much higher than that of a bus waveguide alone.

The travelling wave within the cavity interferes constructively with the input wave whilst at resonance and so the amplitude increases. Neglecting non-linear loss processes like two photon absorption, a reasonable assumption for a diamond device guiding in the NIR, the field enhancement is given as the ratio of field circulating inside the disk (E_d) to the input field (E_i):

$$FE = \left| \frac{E_d}{E_i} \right| = \frac{k}{1 - at} \quad (5.1)$$

The terms of this expression were defined in Chapter 3 but for reference are repeated here: k is the amplitude cross coupling coefficient, t is the amplitude self coupling coefficient, a is the single-pass amplitude transmission defined in terms of the power attenuation coefficient, $\exp(-\alpha L/2)$, and finally L is the length of the disk round trip. The higher the field enhancement, the higher the intensity build up within the disk and the lower the input power required to induce non-linear optical effects. Power enhancement is a relevant consideration when estimating the relative magnitudes of effective index response to input power, as discussed in the next subsection.

5.2.3 Power dependent shift in refractive index

The power-dependent effective index response of a cavity's resonant mode can be calculated by first fitting the peaks resonant in that cavity, as in Chapter 3. Initially, a transmission measurement at highly attenuated powers is used to give a "cold-cavity" response - with no visible asymmetries in the resonances. By peak fitting this data to the analytical model for an all-pass ring resonator the parameters used for calculation of the field enhancement are obtained as defined in Equation 5.1, i.e. the attenuation coefficient, and the amplitude self and cross-coupling coefficients. The change in effective index for a given injection power can then be estimated by

the following equation:

$$\Delta n_{eff} = PE \times P_{in} \times \frac{\delta n}{\delta P} \quad (5.2)$$

where PE is the power enhancement due to build up of light in the resonator. The maximum power enhancement is the square of the FE defined in Section 5.2.2. The effective power enhancement actually experienced at each wavelength, used in Equation 5.2, is the potential maximum multiplied by the percentage of injected power that was coupled into the ring - calculated from the normalised transmission sweep. P_{in} is the calculated injection power on-chip, which has been approximated at a 3 dB increase from what is measured on the detector of the setup used. Finally, $\delta n / \delta P$ is an estimate in the change of effective index per Watt of optical power in the resonator.

For each peak of a transmission measurement, the cold cavity parameters can be extracted from a fit and the maximum power enhancement calculated. Several other transmission measurements at increasing powers, intended to induce non-linear responses, could then be fitted with the aid of these parameters. The build up of power in the resonator increases the temperature of the disk and changes the effective index, which in turn changes the propagation constant of the electric field and red-shifts the resonant peak. As an input wavelength is tuned into resonance the power in the cavity would increase and thus the effective power enhancement would increase also, inducing a greater red-shift. This continues until the wavelength is tuned beyond the maximum detuning possible from that injection power. At this stage the injected power would start to tune out of the resonance so the power drops, undoing the shift in the position of the resonance. This effect is what gives rise to the asymmetric peaks of a transmission sweep showing non-linear optical properties. A depiction of this is shown in Figure 5.3. It can be seen, that due to the power increasing as the pump is tuned into the resonance, the temperature also increases. A small (δ) or large (Δ) increase

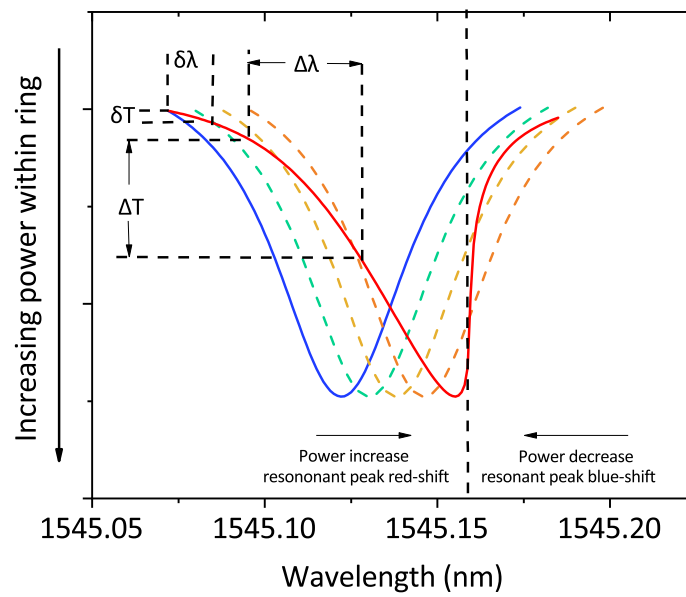


FIGURE 5.3: A resonance position shifting as an increasing percentage of the injection power is coupled into the disk. The solid blue and red lines are the cold-cavity and maximally detuned resonant peak respectively. The dashed lines depict a non-disturbing, low-power probe measurement of the peak at different red-shifted positions.

of temperature (T), results in a small or large shift in wavelength (λ) respectively. An estimate of $\delta n/\delta P$ is used to calculate what the effective index would be at each wavelength and combined with the cold cavity coefficients, the electric field transmission is recalculated. It is from these measurements that a value of $\delta n/\delta P$, the power-dependent effective index response of a mode at that power, is found that gives the best fit to the asymmetrically shifted peak.

For each mode it is found that the $\delta n/\delta P$ remains roughly constant irrespective of injection power, suggesting a linear mechanism by which optical power converts into heat. As diamond is transparent in the UV - NIR it is likely that this process is due to point defects that introduce electronic and vibrational transitions into its large bandgap. A common impurity in diamond which can give rise to broadband absorption over these wavelengths is single substitutional nitrogen [139]. Absorption coefficients at 1064 nm have been shown to be 10^{-3} - 10^{-4} cm^{-1} for diamond with 20 ppb nitrogen and 10^{-1} - 10^{-2} cm^{-1} for 100 ppb [139, 140]. The diamond sourced for this work is quoted to have < 1 ppm nitrogen content and was measured over 1520 - 1630 nm. Assuming the chip in this work has 100 ppb nitrogen content, it can be seen from Figure 5.4 that the absorption should be of the same magnitude at the wavelength range used in the reported measurements. A second heating mechanism is also thought to contribute through absorption at the non-passivated dangling bonds around the disk edge. To elaborate, surface states usually terminate a periodic lattice and can have localised energies that are within the bandgap of a bulk semiconductor. By this means light that is nominally guided can be instead absorbed through exciting valence band electrons.

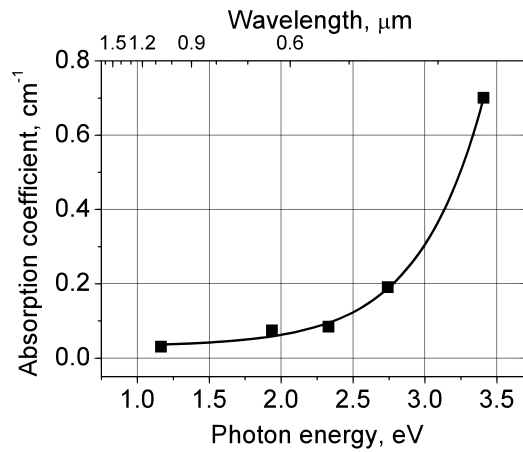


FIGURE 5.4: Absorption in diamond as a function of wavelength [140].

5.3 Results

5.3.1 Low power thermal tuning

The power dependent change in refractive index for a resonance of the hybrid diamond-SOI cavity was calculated by taking measurements for a range of on-chip injection powers, covering approximately $10 \mu\text{W}$ to $90 \mu\text{W}$. The transmission sweeps of the peak and the fitted responses, calculated using the methods detailed in Section 5.2.2, are shown in Figure 5.5. It can be seen that the fit is in good agreement with the measured data and the calculated change in refractive index per watt to achieve this was $8 \times 10^{-3} \text{W}^{-1}$. To quantify the values of the fabricated hybrid device, the results were compared with others in the literature. A resonator device used by Lipson et al., used to quantify the optical bistability on a silicon chip, was chosen as a reference [141]. It was found that their device exhibited a 200 pm/mW shift in peak position, corresponding to what would be a 16.5 pm shift at the maximum on-chip injected power used in this work. It can be seen from Figure 5.5 that the hybrid device fabricated here had a larger shift of 45 pm . To further quantify this disparity, the change in temperature from known thermo-optic coefficients can be calculated. Silicon has a

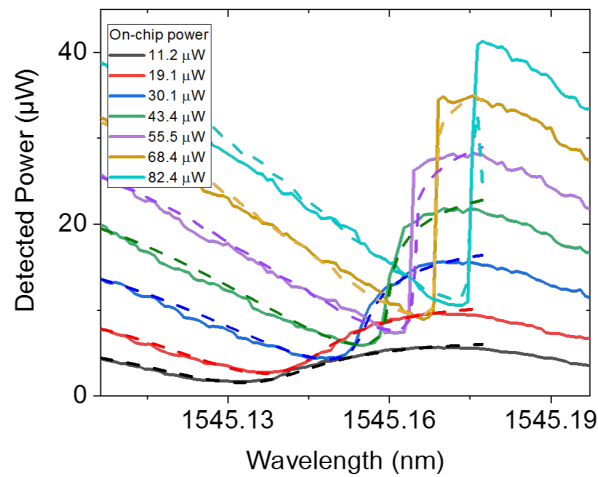


FIGURE 5.5: Power dependent transmission spectrum showing a resonance centred around 1545.13 nm red shifted with increasing powers up to 45 pm. The dashed lines are fits to the data with an estimated input power-dependent shift in effective index of $8 \times 10^{-3} \text{W}^{-1}$.

thermo-optic coefficient of $\sim 2 \times 10^{-4} \text{K}^{-1}$ [136], with diamond having a value orders of magnitude smaller at $3.2 \times 10^{-6} \text{K}^{-1}$ [14]. Using these values and the calculated effective index change of the presented mode, an increase in diamond temperature of 26.8 °C for 82 μW on-chip power was found. The silicon device would have had a change of 1.5 degrees for the rate of effective index change Lipson et al. reported [142, 141]. A larger increase in temperature might be explained by the posited absorption mechanisms. The silicon device was reported to have mainly linear absorption attributed to non-passivated sidewalls. Diamond as well as having its own non-passivated sidewalls, as explained in Section 5.2.3, has absorption due to single substitutional nitrogen. Finally, the diamond integration involves intermolecular bonding compared with the intramolecular bond of the SOI, which could impede conduction of heat out of the diamond - indeed this is confirmed in Section 5.3.2.

The mechanics discussed are however complex and analysis of a second peak is presented to demonstrate this. The peak was chosen for its similar Q-factor and

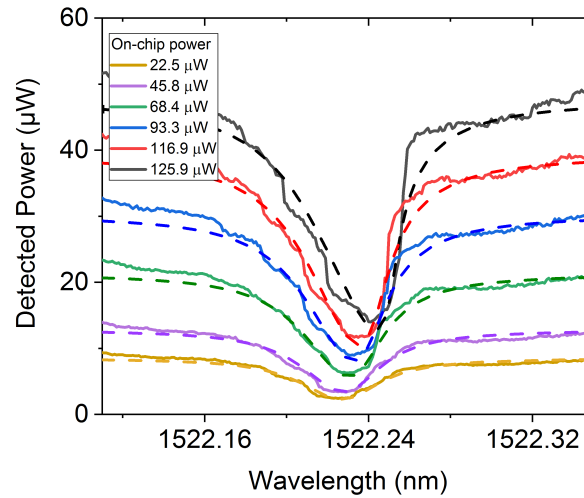


FIGURE 5.6: Power dependent transmission spectrum showing minimal shift in a resonant peak centred at 1522.23 nm, 10 pm. The dashed lines are fits to the data with an estimated input power-dependent shift in effective index of $2.2 \times 10^{-3} \text{W}^{-1}$.

extinction ratio to the first peak investigated, 38k, with the findings shown in Figure 5.6. It can be seen that the effective index shift is much less prominent with a shift in wavelength of only ~ 10 pm for similar powers. The fits were achieved using an input power-dependent effective index shift of $2.2 \times 10^{-3} \text{W}^{-1}$, ~ 4 times smaller than the previous peak. To confirm a correlation between $\delta n / \delta P$ and the absorption mechanisms claimed, they and the distributed losses, which are proportional to absorption, are plotted in Figure 5.7. This is potentially an interesting utility, where applications requiring more thermal stability can be engineered to intentionally couple with the lower loss modes. Relatively larger loss modes (still less than 6 dB/cm), that absorb more light can then be used for active thermal tuning.

The next section looks to separable control of thermal tuning and measurement of the devices, for use in applications with active control and stability requirements - such as high power on-chip Raman lasing at specific wavelengths.

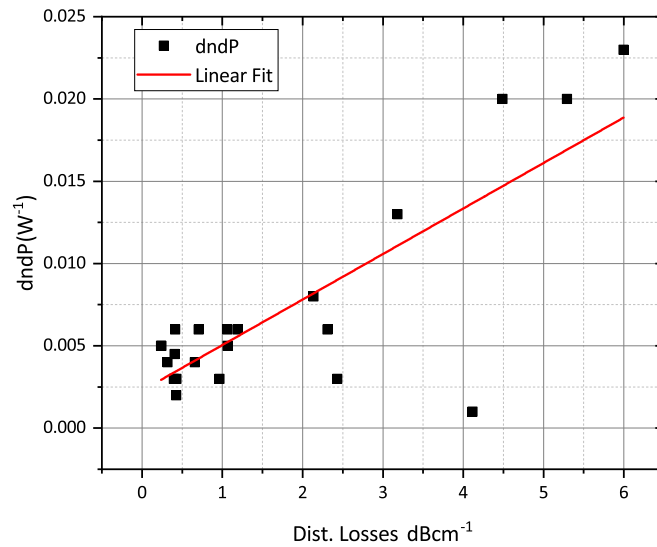


FIGURE 5.7: The coefficient $\delta n/\delta P$ is plotted against distributed losses for each peak showing a correlation between increase in loss and increase in absorption, thus effective index shift.

5.3.2 Demonstration of separable thermal tuning and cold cavity transmission sweeps

It is necessary to demonstrate mutual exclusivity of tuning and measurement for useful applications in integrated optics. In the following section, using the same device as in Section 5.3.1, the resonant peaks are shifted using one high power laser and then measured using a low power “probe” laser. The setup was as follows: a pump laser directed through an Erbium Doped Fibre Amplifier (EDFA) is coupled onto chip through the maximum port of a 90:10 splitter and tuned into a single resonance until maximally detuned. A low power probe laser is then coupled on-chip through the remaining port of the splitter and swept across the wavelength range of 1540 - 1590 nm. The setup is shown schematically in Figure 5.8. Firstly the amplified laser is tuned into resonance with the device for a peak wavelength separated from the intended measurement peak. When maximally detuned the low power probe laser is scanned across the peak of interest and the data collected through an OSA. This is done for a series of pump powers and compared with the

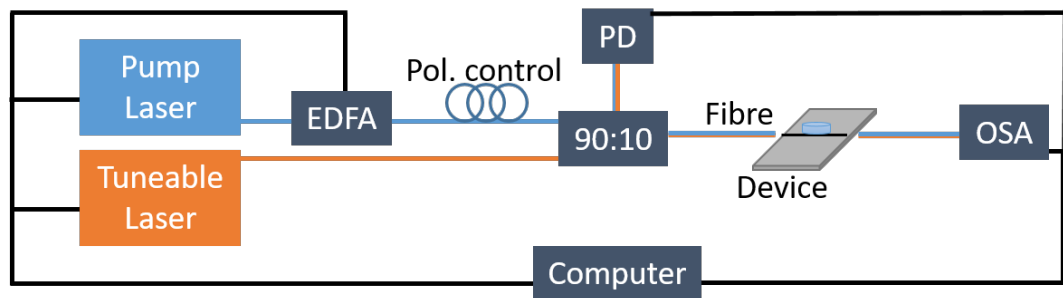


FIGURE 5.8: The optical setup used for the measurement of power dependent refractive index change.

case of no pump laser, i.e. the cold-cavity response. From this, the induced shift of the resonant peaks is observed with the results plotted in Figure 5.9. It can be seen that shifts of over 450 pm have been demonstrated for the maximum pump power capable of the setup. There is also a linear response and these measurements were repeatable over several days demonstrating stability in the tuning. The inset shows the probe laser measurement of a single peak that has been shifted retaining characteristic parameters that define the resonance. As disks have several mode solutions and the micro-assembly techniques developed here involve, but are not limited to, vertical coupling: resonances can be picked for their different thermal properties. Larger mode profiles for less intensity build-up for applications that require thermal stability, or small mode profiles with high intensity build-up for thermal tuning of peaks with separable control.

Thermal camera measurements were also taken to monitor the effect that a high increase in diamond temperature had on the surrounding device. An example of such an image is shown in Figure 5.10. Four diamond disks are labelled with red arrows and it can be seen that these present as dark circles on a rather emissive background. As a result of diamond's relatively low emissivity, measuring the temperature of the diamond was not possible directly. Taking multiple thermal images at varying powers coupled into the disks it was thought that a change in the background temperature might be detected. The difference of

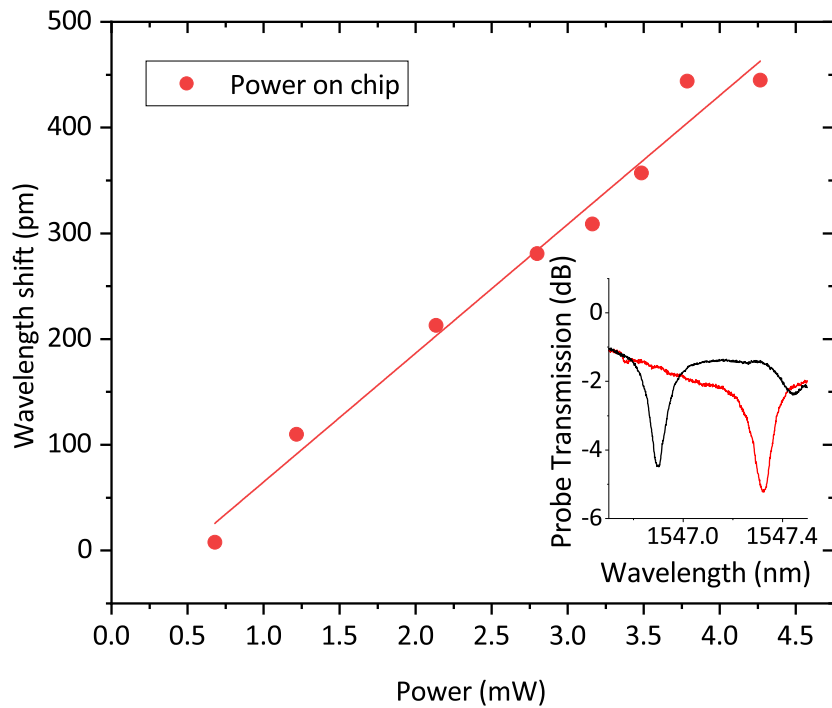


FIGURE 5.9: Probe measured wavelength shift of a resonance centred at ~ 1545 nm for different pump powers at 1563 resonance. Inset: Probe measurement of the shifted peak showing an undisturbed profile - background noise has changed slightly due to non-polarisation-maintaining amplification.

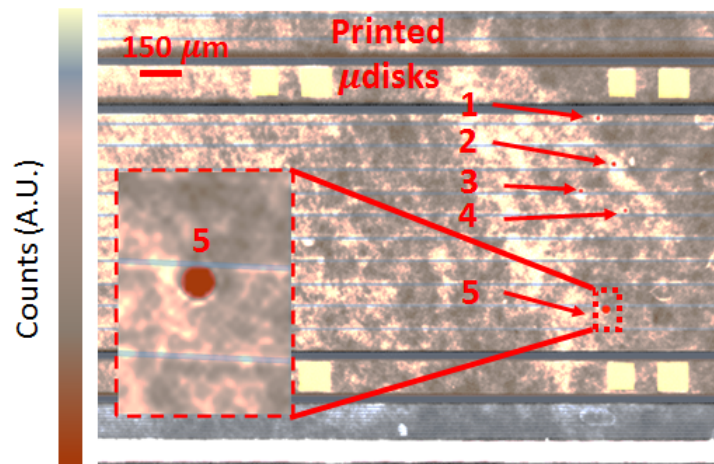


FIGURE 5.10: A false colour image taken using a thermal camera of the SOI device chip integrated with diamond disks. Red arrows point to 4 disks that were printed onto the chip.

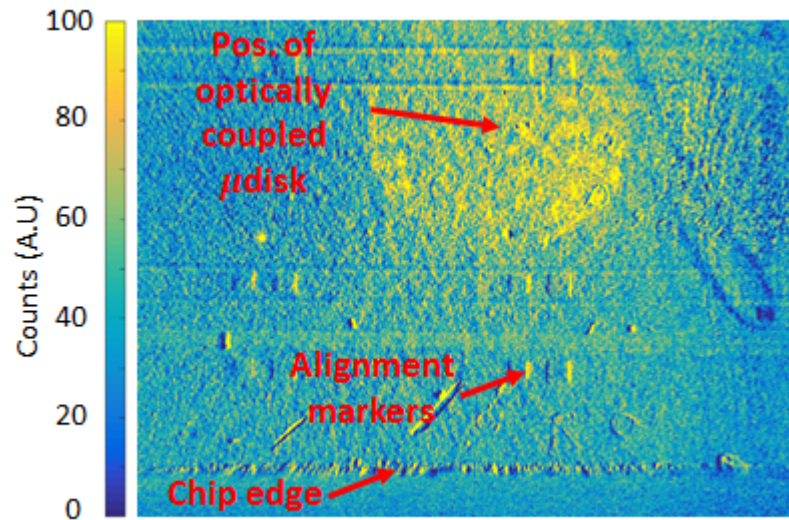


FIGURE 5.11: An intensity difference image between two thermal camera measurements at zero injected power and the highest on-chip power achieved - approximated at 4mW.

intensity counts between two thermal images is displayed in Figure 5.11. It can be seen that there is a clear heat difference centred around disk 3, where all of these measurements were taken. This difference was on the low 10s of counts at the highest on-chip powers however and so a quantitative measure of heat transfer could not be made. Qualitatively however, it is clear that despite high increases in diamond temperature, there is a very low transfer of the heat to the surrounding chip. This further establishes the hypothesised build up of heat within the diamond due to a thermally insulating barrier at the bond interface. It is of great interest that these devices can be separately tuned with relatively low powers inducing high thermal shifts in peak, whilst having very low effects on the surrounding chip. This would allow for densely populated chips with active components that can be separately tuned for application specificity. It is also possible that external heaters could be attached to the monolithic devices allowing for an optically independent shift and stabilisation process.

5.4 Conclusion

Active thermal tuning of a hybrid diamond-SOI device was demonstrated with large wavelength shifts of resonant peaks. Separable control was also reported allowing hybrid diamond devices to be seriously considered for many on-chip applications that can make use of the enviable list of diamond properties. The insulating interface demonstrated very little transfer of heat to the surrounding chip with increases in temperature of nearly 30 °C, showing little increase in the counts of a thermal camera. These rises in temperature corresponded to a ~0.5 nm shift in peak position. Resonant wavelength shifts of this magnitude combined with the presented insulation lends itself to an external heat source being applied on individual resonators for actively tuning and maintaining stable resonances across a several devices and wavelengths. This is useful for applications where high power scaling might be required, in Raman lasing for example.

Chapter 6

Conclusion and Outlook

6.1 Conclusion

The work presented in this thesis has focused on the heterogeneous integration of optical grade diamond with non-native substrates, suitable for wide ranging applications. Diamond is a material with broadband transparency, great thermal stability, large Raman gain and shift, and also hosts several promising spin centre defects for quantum information processing. The main objective was to develop a process by which diamond could be used for integrated optical applications - overcoming challenges associated with its geometrical restrictions. Fabrication and handling techniques were developed for ultra-thin, free-standing diamond membranes and their integration - demonstrated here with established SOI platforms. Monolithic diamond resonator structures were fabricated and transfer printed, exhibiting high intrinsic Q-factors as large as 5.0×10^5 . Dynamic tuning of peak wavelengths by almost 0.5 nm was achieved through optically induced thermal changes. The techniques developed in this thesis are believed to have advanced the state-of-the-art by addressing not only the material wedge [52, 53, 143, 55], the mode interaction with the diamond [64, 63, 15, 79], and the scalability of possible devices [34, 67], but all three.

Chapter 1 gave an introduction to the material properties of diamond, with a

focus on why they are desirable for integrated optical applications. A brief introduction of waveguiding theory, relevant to the optical devices developed in this work, was detailed. Synthesis techniques used in the fabrication of high optical-quality diamond chips were explained and the challenges with using such samples for integrated optics was outlined. A short review of current works was also given, which have addressed the challenges similarly tackled by this work. The novelty of this approach is highlighted, which reports monolithic structures robust to transfer and micro-assembly of hybrid material devices. The structures fully support optical modes within, increasing light interaction and process-efficiency, the diamond thickness variation is mitigated over small device sizes. Finally, the topics detailed in the chapters to follow were outlined.

In the second chapter a process for fabrication, handling, and characterisation, of ultra thin diamond membranes with low surface roughness was reported. Sub-micrometre thickness membranes were fabricated, and techniques for the characterisation of typical thickness wedges, and surface roughness, were both discussed. The lower thickness side of the diamond was comfortably within the vertical criterion for single mode only support at telecommunication wavelengths. Low surface roughness values were also achieved with a value of 0.4 nm r.m.s. over $10 \mu\text{m}^2$ - which promoted a large surface area of contact between the diamond and target substrate of the subsequent chapters bonding.

Chapter 3 demonstrates the integration of diamond membranes through capillary-assisted bonding with a silicon-on-insulator platform. This hybrid device was designed to demonstrate and characterise optical interaction between an underlying waveguide and the diamond. The fabrication of the diamond membrane was then briefly detailed, as it was discussed fully in Chapter 2. Handling and integration of the membrane, with silicon resonator devices, were then detailed and the separation at the interface investigated. SEMs found that $1 \mu\text{m}$ membranes deforming over a single axis achieved intimate contact, but optical

interference fringes showed that bonding over complex features - those requiring deformation in 2 axes - gave a non-uniform separation. An analysis of how the optical properties of the hybrid device differed from the nominal attributes of the silicon device alone was conducted. These were compared with what modal simulations predicted for each case and it was found that group index changes were in line with what simulations predicted. That is, for a diamond membrane bonded to silicon and with an average separation of 70 nm. Loaded hybrid device Q-factors for this device were calculated to be approximately 1.1×10^4 .

In the next chapter the complexities of integrating a mm^2 membrane, such as non-uniformity in the bonding, are addressed by fabricating monolithic diamond devices for individual transfer. Tessellated square membranes were printed, and their thickness was measured using AFM, to characterise and demonstrate the versatile, application-driven device geometries that can be fabricated from a single wedged chip of diamond. Disk resonators were also fabricated and transfer printed onto a SOI platform that could be used for non-linear applications such as four wave mixing or on-chip Raman lasing. Intrinsic Q-factors of these hybrid devices were shown to be 9.6×10^4 on average with a maximum resonance found to be $\sim 5.0 \times 10^5$. By this approach the light will guide fully within the diamond and increase the interaction by orders of magnitude compared with the evanescent approach of Chapter 3. This will act to massively decrease the threshold injection powers required for Raman lasing for example.

Dynamic thermal tuning of a micro-assembled diamond-on-silicon device was demonstrated with large 100s pm shifts in resonant wavelength peaks. Control of the tuning was achieved by increasing the probe power and also separable control was presented using a pump beam. The mutually exclusive tuning and measurement results reported, allow for these hybrid diamond devices to be seriously considered for many on-chip applications that can then make use of diamond's optical properties. The interface between the diamond device and the

integration platform was demonstrated to greatly impede the transfer of heat, with increases in diamond temperature of ~ 30 °C showing little increase in the surrounding area's temperature. Shifts of close to 0.5 nm in resonant wavelength were demonstrated for the on-chip powers achievable. Tuning of this magnitude, combined with the presented thermal insulation, would enable an external heat source to be applied onto individual resonators to achieve active tuning and resonance stability across a several devices and wavelengths. This is useful for applications where high power scaling might be required, in Raman lasing for example, where external heat sources could be varied to maintain peak position when increased optical powers would nominally induce a shift of their own.

6.2 Future Work

6.2.1 Hybridisation with visible-light transparent platforms for quantum applications

The techniques developed in the completion of this PhD are independent of material platform. In future, integration of diamond devices could and should be applied to different non-native substrates. For example, GaN is a material which is transparent in the visible wavelength range that might be used as a bus for efficiently collecting colour centre emissions from a diamond disk. Gallium Nitride has exhibited a linear electro-optic coefficient in the same order of magnitude as GaAs, or AlN which could also be used for tuning of resonances in place of external heaters, a further possibility [144, 145]. Suppression of phonon assisted sidebands and enhancement of zero phonon line transmission with nitrogen vacancy centre emissions is necessary to improve greatly the useful light output for quantum applications. Ring resonators are ideally placed for this enhancement and by the methods detailed in this thesis, the light would already

be on-chip with capability of directing and processing elsewhere with ultra-low loss.

6.2.2 Photoluminescent measurement automation, alignment, and scalability

For many applications involving atom-like emitters and integrated optics, accurate knowledge of their positions are required. If for example, a ring resonator was to be fabricated from a diamond chip containing native nitrogen vacancies, the ring would need to be accurately aligned to prevent either etching away or missing the resonant enhancement from being placed in the cavity. It would thus greatly improve the capabilities of the department and future development of quantum information processing research to establish an automatic alignment and photoluminescence setup. Alignment markers can be patterned on a chip far separated for quantifying both lateral positions and rotation. Then with a confocally scanning excitation laser and photodetector setup, controlled with Labview, this could all be achieved.

Transfer printing also enables a direct scaling of the micro-assembly techniques presented in this thesis. The capability to print several diamond disks from an array in a single step onto pre-determined positions of an integration substrate can help realise fabrication of quantum information processing chips.

6.2.3 Efficient development of spin maintaining diamond etch processing

Tangentially, with the proposed relevance to nitrogen vacancy quantum computing, the methodologies detailed are ideally placed to investigate optimum fabrication routes for colour centre spin properties. The tessellated squares for example, detailed in Chapter 4, can be transferred allowing different material processing on the scale of 10 - 100s of samples per single diamond chip. Our

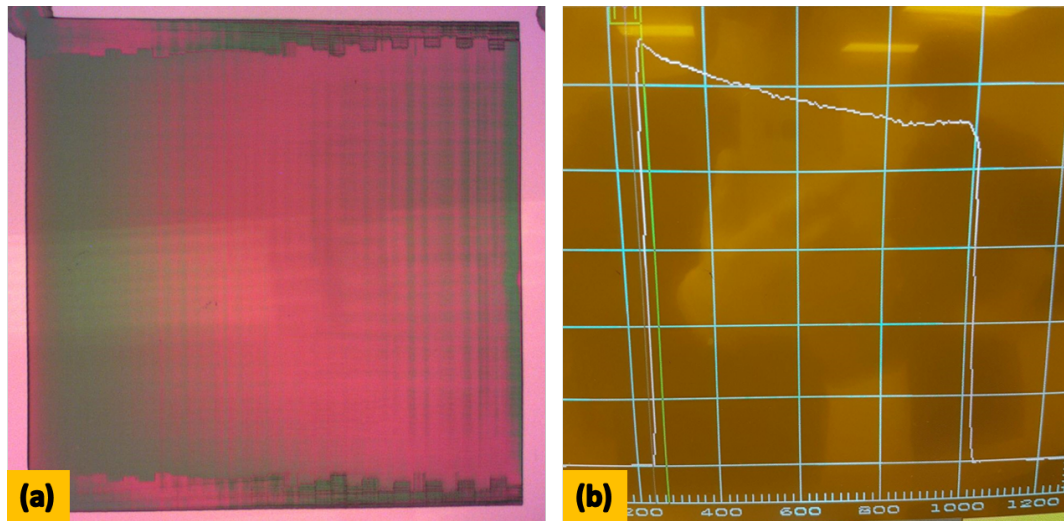


FIGURE 6.1: a) An optical microscope image of a grayscale patterned slope of photoresist. b) A dektak thickness measurement of the same photoresist.

collaborative work with Morley et al. [146] has shown that NVs can be three-dimensionally written using laser pulses and subsequent annealing. By treating several of the tessellated platelets differently and then utilising this process, spin properties could be quickly and quantifiably characterised relative to one another. The wedged thickness of diamond could also be used to determine an optimum depth of the defect balancing detrimental surface effects and maintaining a planar waveguiding cross-section.

6.2.4 Grayscale photolithographic reduction of material wedge

With respect to wedged thickness a development of grayscale lithography started in this project could be brought to completion. Photoresist is exposed with a graduated level of exposure resulting in a graduated cross-linking response - after development a sloped resist mask is left. An example of this is shown in Figure 6.1. By aligning this slope inversely to the wedge gradient and accounting for etch selectivity a mask etch-through process could be used to reduce particularly large thickness differences. Etching completely through a mask will impose some

increase in surface roughness but provided it is not large this can be reduced again using the developed Ar-Cl₂ ICP-RIE etch.

6.2.5 Final remark

Diamond is a material with remarkable properties for use in optical applications and the works to develop this platform have been amazing. I believe this thesis builds on these works and provides a novel means to scalable integration of diamond towards wide ranging applications. I am excited to see how the field progresses in the years to come.

Bibliography

- [1] Igor Aharonovich, Andrew D. Greentree, and Steven Praver. “Diamond photonics”. In: *Nature Photonics* 5.7 (2011), pp. 397–405. ISSN: 1749-4885. DOI: [10 . 1038 / nphoton . 2011 . 54](https://doi.org/10.1038/nphoton.2011.54). URL: <http://dx.doi.org/10.1038/nphoton.2011.54>.
- [2] The Drum. *1948: De Beers 'A diamond is forever' campaign invents the modern day engagement ring*. 2016. URL: <https://www.thedrum.com/news/2016/03/31/1948-de-beers-diamond-forever-campaign-invents-the-modern-day-engagement-ring> (visited on 02/14/2019).
- [3] D Tabor. “The physical meaning of indentation and scratch hardness”. In: *British Journal of Applied Physics* 7.5 (1956), pp. 159–166. ISSN: 0508-3443. DOI: [10 . 1088 / 0508 - 3443 / 7 / 5 / 301](https://doi.org/10.1088/0508-3443/7/5/301). URL: <http://stacks.iop.org/0508-3443/7/i=5/a=301?key=crossref.bcc0e1df248fff2b89965a521a28db4e>.
- [4] KSQ Technologies Co. Ltd. *Matrix Body PDC Drill Bit , Diamond Oil Drill Bit*. URL: <http://www.rock-drillingtools.com/sale-10899528-6-81-2-9-1-2-12-1-4-matrix-body-pdc-drill-bit-diamond-oil-drill-bit.html> (visited on 02/13/2019).
- [5] Loyd James McKnight, Martin D. Dawson, and Stephane Calvez. “Diamond Raman waveguide lasers: Completely analytical design optimization incorporating scattering losses”. In: *IEEE Journal of Quantum Electronics* 47.8 (2011), pp. 1069–1077. ISSN: 00189197. DOI: [10 . 1109 / JQE . 2011 . 2152366](https://doi.org/10.1109/JQE.2011.2152366).

- [6] I Aharonovich et al. "Diamond-based single-photon emitters". In: *Reports on Progress in Physics* 74.7 (2011), p. 076501. ISSN: 0034-4885. DOI: [10.1088/0034-4885/74/7/076501](https://doi.org/10.1088/0034-4885/74/7/076501). URL: <http://stacks.iop.org/0034-4885/74/i=7/a=076501?key=crossref.de26298a109e3a23e095d261d1e2f211>.
- [7] Lanhua Wei et al. "Thermal conductivity of isotopically modified single crystal diamond". In: *Physical Review Letters* 70.24 (1993), pp. 3764–3767. ISSN: 00319007. DOI: [10.1103/PhysRevLett.70.3764](https://doi.org/10.1103/PhysRevLett.70.3764).
- [8] P. Bergonzo et al. "CVD diamond for radiation detection devices". In: *Diamond and Related Materials* 10.3-7 (2001), pp. 631–638. ISSN: 09259635. DOI: [10.1016/S0925-9635\(00\)00554-9](https://doi.org/10.1016/S0925-9635(00)00554-9).
- [9] M Seal. "Thermal and optical applications of thin film diamond". In: *Philosophical Transactions of the Royal Society of London. Series A: Physical and Engineering Sciences* 342.1664 (1993), pp. 313–322. ISSN: 0962-8428. DOI: [10.1098/rsta.1993.0024](https://doi.org/10.1098/rsta.1993.0024). URL: <http://www.royalsocietypublishing.org/doi/10.1098/rsta.1993.0024>.
- [10] M. Seal. "Applications exploiting the extreme properties of diamonds". In: *Materials Science and Engineering: B* 11.1-4 (1992), pp. 167–171. ISSN: 09215107. DOI: [10.1016/0921-5107\(92\)90209-R](https://doi.org/10.1016/0921-5107(92)90209-R). URL: <http://linkinghub.elsevier.com/retrieve/pii/092151079290209R>.
- [11] B. B. Buckley et al. "Spin-Light Coherence for Single-Spin Measurement and Control in Diamond". In: *Science* 330.6008 (2010), pp. 1212–1215. ISSN: 0036-8075. DOI: [10.1126/science.1196436](https://doi.org/10.1126/science.1196436). URL: <http://www.sciencemag.org/cgi/doi/10.1126/science.1196436>.
- [12] Pawel Latawiec et al. "On-chip diamond Raman laser". In: *Optica* 2.11 (2015), p. 924. ISSN: 2334-2536. DOI: [10.1364/OPTICA.2.000924](https://doi.org/10.1364/OPTICA.2.000924). arXiv: [1509.00373](https://arxiv.org/abs/1509.00373). URL: <https://www.osapublishing.org/abstract.cfm?URI=optica-2-11-924>.

- [13] R. P. Mildren and A. Sabella. "Highly efficient diamond Raman laser". In: *Optics Letters* 34.18 (2009), p. 2811. ISSN: 0146-9592. DOI: [10.1364/ol.34.002811](https://doi.org/10.1364/ol.34.002811).
- [14] T Ruf et al. "Temperature dependence of the refractive index of diamond up to 925 K". In: *Physical Review B - Condensed Matter and Materials Physics* 62.24 (2000), pp. 578–581. DOI: [10.1103/PhysRevB.62.16578](https://doi.org/10.1103/PhysRevB.62.16578).
- [15] B J M Hausmann et al. "Integrated high-quality factor optical resonators in diamond." In: *Nano letters* 13.5 (2013), pp. 1898–902. ISSN: 1530-6992. DOI: [10.1021/nl3037454](https://doi.org/10.1021/nl3037454). URL: <http://www.ncbi.nlm.nih.gov/pubmed/23427820>.
- [16] Andrei Faraon et al. "Resonant enhancement of the zero-phonon emission from a color center in a diamond cavity". In: *Nature Photonics* 5.5 (2010), p. 5. ISSN: 1749-4885. DOI: [10.1038/nphoton.2011.52](https://doi.org/10.1038/nphoton.2011.52). arXiv: [1012.3815](https://arxiv.org/abs/1012.3815). URL: <http://arxiv.org/abs/1012.3815>.
- [17] Jing Zhang et al. "Silicon photonics fiber-to-the-home transceiver array based on transfer-printing-based integration of III-V photodetectors". In: *Optics Express* 25.13 (2017), p. 14290. ISSN: 1094-4087. DOI: [10.1364/OE.25.014290](https://doi.org/10.1364/OE.25.014290). URL: <https://www.osapublishing.org/abstract.cfm?URI=oe-25-13-14290>.
- [18] K. M C Fu et al. "Coupling of nitrogen-vacancy centers in diamond to a GaP waveguide". In: *Applied Physics Letters* 93.23 (2008), pp. 29–32. ISSN: 00036951. DOI: [10.1063/1.3045950](https://doi.org/10.1063/1.3045950). arXiv: [0811.0328](https://arxiv.org/abs/0811.0328).
- [19] Elke Neu et al. "Single photon emission from silicon-vacancy colour centres in chemical vapour deposition nano-diamonds on iridium". In: *New Journal of Physics* 13.2 (2011), p. 025012. ISSN: 1367-2630. DOI: [10.1088/1367-2630/13/2/025012](https://doi.org/10.1088/1367-2630/13/2/025012). arXiv: [1008.4736](https://arxiv.org/abs/1008.4736). URL: <http://stacks.iop.org/1367-2630/13/i=2/a=025012?key=crossref.0265718449d162fd8b5c4479487e12b2>.

- [20] Jr. Wentorf, R. H. and H. P. Bovenkerk. "On the Origin of Natural Diamonds." In: *The Astrophysical Journal* 134 (1961), p. 995. ISSN: 0004-637X. DOI: 10.1086/147227. URL: <http://adsabs.harvard.edu/doi/10.1086/147227>.
- [21] W. Dan Hausel. Edward I. Erlich. *Diamond deposits : origin, exploration, and history of discovery*. Littleton, CO : Society for Mining, Metallurgy, and Exploration, 2002. ISBN: 0873352130. URL: <https://trove.nla.gov.au/work/32370194?q{\&}versionId=46612362>.
- [22] Hobart M. King. *How Do Diamonds Form?* 2005. URL: <https://geology.com/articles/diamonds-from-coal/> (visited on 03/06/2019).
- [23] International Diamond Laboratories. *hpht - high pressure high temperature*. 2009. URL: https://web.archive.org/web/20090501065610/http://www.diamondlab.org/80-hpht{_}synthesis.html.
- [24] Y.A. Sorb, F.P. Bundy, and R.C. DeVries. "Diamond: High-Pressure Synthesis". In: *Reference Module in Materials Science and Materials Engineering* October (2016), pp. 0–8. DOI: 10.1016/B978-0-12-803581-8.03772-3. URL: <http://linkinghub.elsevier.com/retrieve/pii/B9780128035818037723>.
- [25] Y.A. Sorb, F.P. Bundy, and R.C. DeVries. "Diamond: High-Pressure Synthesis". In: *Reference Module in Materials Science and Materials Engineering* October (2016), pp. 0–8. DOI: 10.1016/B978-0-12-803581-8.03772-3. URL: <http://linkinghub.elsevier.com/retrieve/pii/B9780128035818037723>.
- [26] Sergio Ferro. "Synthesis of diamond". In: *Journal of Materials Chemistry* 12.10 (2002), pp. 2843–2855. ISSN: 09599428. DOI: 10.1039/b204143j. URL: <http://xlink.rsc.org/?DOI=b204143j>.

- [27] Mike N R Ashfold et al. "Thin film diamond by chemical vapour deposition methods". In: *Chemical Society Reviews* 23.1 (1994), p. 21. ISSN: 0306-0012. DOI: 10.1039/cs9942300021. URL: <http://xlink.rsc.org/?DOI=cs9942300021>.
- [28] J. E. Butler et al. "Understanding the chemical vapor deposition of diamond: Recent progress". In: *Journal of Physics Condensed Matter* 21.36 (2009). ISSN: 09538984. DOI: 10.1088/0953-8984/21/36/364201.
- [29] Qi Liang et al. "Large area single-crystal diamond synthesis by 915 mhz microwave plasma-assisted chemical vapor deposition". In: *Crystal Growth and Design* 14.7 (2014), pp. 3234–3238. ISSN: 15287505. DOI: 10.1021/cg500693d.
- [30] Igor Aharonovich et al. "Homoepitaxial growth of single crystal diamond membranes for quantum information processing". In: *Advanced Materials* 24.10 (2012). ISSN: 09359648. DOI: 10.1002/adma.201103932. arXiv: 1109.5634.
- [31] Yu A. Mankelevich and P. W. May. "New insights into the mechanism of CVD diamond growth: Single crystal diamond in MW PECVD reactors". In: *Diamond and Related Materials* 17.7-10 (2008), pp. 1021–1028. ISSN: 09259635. DOI: 10.1016/j.diamond.2008.03.022. arXiv: 1504.02011.
- [32] Awadesh Mallik. "Microwave Plasma CVD Grown Single Crystal Diamonds – A Review". In: *Journal of Coating Science and Technology* 3.2 (2016), pp. 75–99. ISSN: 23693355. DOI: 10.6000/2369-3355.2016.03.02.4. URL: <http://www.lifescienceglobal.com/journals/journal-of-coating-science-and-technology/volume-3-number-2/115-abstract/jcst/2460-abstract-microwave-plasma-cvd-grown-single-crystal-diamonds-a-review>.

- [33] Matthias Schreck et al. "Large-area high-quality single crystal diamond". In: *MRS Bulletin* 39.06 (2014), pp. 504–510. ISSN: 0883-7694. DOI: [10.1557/mrs.2014.96](https://doi.org/10.1557/mrs.2014.96). URL: http://www.journals.cambridge.org/abstract{_}S0883769414000967.
- [34] Afaq Habib Piracha et al. "Scalable fabrication of high-quality, ultra-thin single crystal diamond membrane windows". In: *Nanoscale* 8.12 (2016), pp. 6860–6865. ISSN: 2040-3364. DOI: [10.1039/C5NR08348F](https://doi.org/10.1039/C5NR08348F). URL: <http://pubs.rsc.org/en/content/articlehtml/2016/nr/c5nr08348f><http://xlink.rsc.org/?DOI=C5NR08348F>.
- [35] Andrew P. Magyar et al. "Fabrication of thin, luminescent, single-crystal diamond membranes". In: *Applied Physics Letters* 99.8 (2011), pp. 1–4. ISSN: 00036951. DOI: [10.1063/1.3628463](https://doi.org/10.1063/1.3628463). arXiv: [1108.0738](https://arxiv.org/abs/1108.0738).
- [36] Evan L.H. Thomas et al. "Chemical mechanical polishing of thin film diamond". In: *Carbon* 68 (2014), pp. 473–479. ISSN: 00086223. DOI: [10.1016/j.carbon.2013.11.023](https://doi.org/10.1016/j.carbon.2013.11.023). arXiv: [1308.1239](https://arxiv.org/abs/1308.1239). URL: <http://dx.doi.org/10.1016/j.carbon.2013.11.023>.
- [37] Evan L H Thomas et al. "Silica based polishing of {100} and {111} single crystal diamond". In: *Science and Technology of Advanced Materials* 15.3 (2014), p. 035013. ISSN: 1468-6996. DOI: [10.1088/1468-6996/15/3/035013](https://doi.org/10.1088/1468-6996/15/3/035013). arXiv: [1402.3446](https://arxiv.org/abs/1402.3446). URL: <http://www.tandfonline.com/doi/full/10.1088/1468-6996/15/3/035013>.
- [38] Sean Reilly et al. "Monolithic diamond Raman laser". In: *Optics Letters* 40.6 (2015), p. 930. ISSN: 0146-9592. DOI: [10.1364/OL.40.000930](https://doi.org/10.1364/OL.40.000930). URL: <http://ol.osa.org/abstract.cfm?URI=ol-40-6-930>.
- [39] Philip R Dolan et al. "Femtoliter tunable optical cavity arrays." In: *Optics letters* 35.21 (2010), pp. 3556–3558. ISSN: 0146-9592. DOI: [10.1364/OL.35.003556](https://doi.org/10.1364/OL.35.003556).

- [40] P. R. Dolan et al. "Robust, tunable, and high purity triggered single photon source at room temperature using a nitrogen-vacancy defect in diamond in an open microcavity". In: *Optics Express* 26.6 (2018), p. 7056. ISSN: 1094-4087. DOI: [10.1364/OE.26.007056](https://doi.org/10.1364/OE.26.007056). URL: <https://www.osapublishing.org/abstract.cfm?URI=oe-26-6-7056>.
- [41] Zhaoming Zhu and Thomas Brown. "Full-vectorial finite-difference analysis of microstructured optical fibers". In: *Opt. Express* 10.17 (2002), pp. 853–864.
- [42] V.S. Ilchenko and A.B. Matsko. "Optical resonators with whispering-gallery modes-part II: applications". In: *IEEE Journal of Selected Topics in Quantum Electronics* 12.1 (2006), pp. 15–32. ISSN: 1077-260X. DOI: [10.1109/JSTQE.2005.862943](https://doi.org/10.1109/JSTQE.2005.862943). URL: <http://ieeexplore.ieee.org/document/1588879/>.
- [43] H. Paul Urbach et al. "Characterization of Integrated Optical Strain Sensors Based on Silicon Waveguides". In: *IEEE Journal of Selected Topics in Quantum Electronics* 20.4 (2013), pp. 101–110. ISSN: 1077-260X. DOI: [10.1109/jstqe.2013.2289992](https://doi.org/10.1109/jstqe.2013.2289992).
- [44] A. Ksendzov and Y. Lin. "Integrated optics ring-resonator sensors for protein detection". In: *Optics Letters* 30.24 (2005), p. 3344. ISSN: 0146-9592. DOI: [10.1364/OL.30.003344](https://doi.org/10.1364/OL.30.003344). URL: <https://www.osapublishing.org/abstract.cfm?URI=ol-30-24-3344>.
- [45] Nanxi Li et al. "C-band swept wavelength erbium-doped fiber laser with a high-Q tunable interior-ridge silicon microring cavity". In: *Optics Express* 24.20 (2016), p. 22741. ISSN: 1094-4087. DOI: [10.1364/OE.24.022741](https://doi.org/10.1364/OE.24.022741). URL: <https://www.osapublishing.org/abstract.cfm?URI=oe-24-20-22741>.
- [46] P. Mullner and Rainer Hainberger. "Structural Optimization of Silicon-On-Insulator Slot Waveguides". In: *IEEE Photonics Technology Letters* 18.24 (2006), pp. 2557–2559. ISSN: 1041-1135. DOI:

- 10 . 1109 / LPT . 2006 . 886974. URL:
<http://ieeexplore.ieee.org/document/4016123/>.
- [47] Yanfeng Zhang et al. "Large cross-section edge-coupled diamond waveguides". In: *Diamond and Related Materials* 20.4 (2011), pp. 564–567. ISSN: 09259635. DOI: 10 . 1016 / j . diamond . 2011 . 03 . 002. URL:
<http://dx.doi.org/10.1016/j.diamond.2011.03.002>.
- [48] M. Schreck et al. "Diamond nucleation on iridium buffer layers and subsequent textured growth: A route for the realization of single-crystal diamond films". In: *Applied Physics Letters* 78.2 (2001), pp. 192–194. ISSN: 00036951. DOI: 10.1063/1.1337648.
- [49] B. Stritzker et al. "A route to diamond wafers by epitaxial deposition on silicon via iridium/yttria-stabilized zirconia buffer layers". In: *Applied Physics Letters* 84.22 (2004), pp. 4541–4543. ISSN: 0003-6951. DOI: 10.1063/1.1758780.
- [50] Hideaki Yamada et al. "Fabrication and fundamental characterizations of tiled clones of single-crystal diamond with 1-inch size". In: *Diamond and Related Materials* 24 (2012), pp. 29–33. ISSN: 09259635. DOI: 10 . 1016 / j . diamond . 2011 . 09 . 007. URL:
<http://dx.doi.org/10.1016/j.diamond.2011.09.007>.
- [51] Robert G. Hunsperger. *Integrated Optics: Theory and Technology*. Vol. 33. Springer Series in Optical Sciences. Berlin, Heidelberg: Springer Berlin Heidelberg, 1984, pp. 1–5. ISBN: 978-3-662-13567-9. DOI: 10 . 1007 / 978 - 3 - 662 - 13565 - 5. URL:
<http://link.springer.com/10.1007/978-3-662-13565-5>.
- [52] Michael Gould et al. "Large-scale GaP-on-diamond integrated photonics platform for NV center-based quantum information". In: *Journal of the Optical Society of America B* 33.3 (2016), B35. ISSN: 0740-3224. DOI:

- 10 . 1364 / JOSAB . 33 . 000B35. URL: <https://www.osapublishing.org/abstract.cfm?URI=josab-33-3-B35>.
- [53] Michael Gould et al. “Efficient Extraction of Zero-Phonon-Line Photons from Single Nitrogen-Vacancy Centers in an Integrated GaP-on-Diamond Platform”. In: *Physical Review Applied* 6.1 (2016), pp. 2–7. ISSN: 23317019. DOI: [10.1103/PhysRevApplied.6.011001](https://doi.org/10.1103/PhysRevApplied.6.011001). arXiv: [1606.01826](https://arxiv.org/abs/1606.01826).
- [54] Paul E. Barclay et al. “Hybrid nanocavity resonant enhancement of color center emission in diamond”. In: *Physical Review X* 1.1 (2011), pp. 1–7. ISSN: 21603308. DOI: [10.1103/PhysRevX.1.011007](https://doi.org/10.1103/PhysRevX.1.011007). arXiv: [1105.5137](https://arxiv.org/abs/1105.5137).
- [55] Paul E. Barclay et al. “Chip-based microcavities coupled to nitrogen-vacancy centers in single crystal diamond”. In: *Applied Physics Letters* 95.19 (2009), pp. 93–96. ISSN: 00036951. DOI: [10.1063/1.3262948](https://doi.org/10.1063/1.3262948). arXiv: [arXiv:0908.2148v1](https://arxiv.org/abs/0908.2148v1).
- [56] Nicole Thomas et al. “Waveguide-integrated single-crystalline GaP resonators on diamond”. In: *Optics Express* 22.11 (2014), p. 13555. ISSN: 1094-4087. DOI: [10.1364/OE.22.013555](https://doi.org/10.1364/OE.22.013555). URL: <http://www.opticsinfobase.org/abstract.cfm?URI=oe-22-11-13555>.
- [57] Kay D. Jahnke et al. “All-Optical Initialization, Readout, and Coherent Preparation of Single Silicon-Vacancy Spins in Diamond”. In: *Physical Review Letters* 113.26 (2014), pp. 1–5. ISSN: 0031-9007. DOI: [10.1103/physrevlett.113.263602](https://doi.org/10.1103/physrevlett.113.263602).
- [58] Bernhard Grotz et al. “Charge state manipulation of qubits in diamond”. In: *Nature Communications* 3.1 (2012), p. 729. ISSN: 2041-1723. DOI: [10.1038/ncomms1729](https://doi.org/10.1038/ncomms1729). URL: <http://www.nature.com/articles/ncomms1729>.
- [59] Shanying Cui and Evelyn L. Hu. “Effect of fluorinated diamond surface on charge state of nitrogen-vacancy centers”. In: (2013), pp. 1–11. arXiv: [1304.1407](https://arxiv.org/abs/1304.1407). URL: <http://arxiv.org/abs/1304.1407>.

- [60] B. K. Ofori-Okai et al. "Spin properties of very shallow nitrogen vacancy defects in diamond". In: *Physical Review B - Condensed Matter and Materials Physics* 86.8 (2012), pp. 1–5. ISSN: 10980121. DOI: [10.1103/PhysRevB.86.081406](https://doi.org/10.1103/PhysRevB.86.081406).
- [61] Toyofumi Ishikawa et al. "Optical and Spin Coherence Properties of Nitrogen-Vacancy Centers Placed in a 100 nm Thick Isotopically Purified Diamond Layer". In: *Nano Letters* 12.4 (2012), pp. 2083–2087. ISSN: 1530-6984. DOI: [10.1021/nl300350r](https://doi.org/10.1021/nl300350r). URL: <http://pubs.acs.org/doi/10.1021/nl300350r>.
- [62] B. J. M. Hausmann et al. "Diamond nonlinear photonics". In: *Nature Photonics* 8.5 (2014), pp. 369–374. ISSN: 1749-4885. DOI: [10.1038/nphoton.2014.72](https://doi.org/10.1038/nphoton.2014.72). URL: <http://dx.doi.org/10.1038/nphoton.2014.72>
<http://www.nature.com/doi/10.1038/nphoton.2014.72>
<http://www.nature.com/articles/nphoton.2014.72>.
- [63] Pawel Latawiec et al. "On-chip diamond Raman laser". In: *Optica* 2.11 (2015), p. 924. ISSN: 2334-2536. DOI: [10.1364/OPTICA.2.000924](https://doi.org/10.1364/OPTICA.2.000924). arXiv: [1509.00373](https://arxiv.org/abs/1509.00373). URL: <https://www.osapublishing.org/abstract.cfm?URI=optica-2-11-924>.
- [64] Pawel Latawiec et al. "Integrated diamond Raman laser pumped in the near-visible". In: *Optics Letters* 43.2 (2018), p. 318. ISSN: 0146-9592. DOI: [10.1364/OL.43.000318](https://doi.org/10.1364/OL.43.000318). arXiv: [1712.04385](https://arxiv.org/abs/1712.04385). URL: <http://arxiv.org/abs/1712.04385>
<https://doi.org/10.1364/OL.43.000318>
<https://www.osapublishing.org/abstract.cfm?URI=ol-43-2-318>.
- [65] Birgit J M Hausmann et al. "Integrated diamond networks for quantum nanophotonics." In: *Nano letters* 12.3 (2012), pp. 1578–82. ISSN: 1530-6992.

- DOI: 10.1021/nl204449n. URL: <http://www.ncbi.nlm.nih.gov/pubmed/22339606>.
- [66] Michael J. Burek et al. "Fiber-Coupled Diamond Quantum Nanophotonic Interface". In: *Physical Review Applied* 8.2 (2017), p. 024026. ISSN: 2331-7019. DOI: 10.1103/PhysRevApplied.8.024026. arXiv: 1612.05285. URL: <https://link.aps.org/doi/10.1103/PhysRevApplied.8.024026>.
- [67] Afaq H. Piracha et al. "Scalable Fabrication of Integrated Nanophotonic Circuits on Arrays of Thin Single Crystal Diamond Membrane Windows". In: *Nano Letters* 16.5 (2016), pp. 3341–3347. ISSN: 1530-6984. DOI: 10.1021/acs.nanolett.6b00974. URL: <http://pubs.acs.org/doi/10.1021/acs.nanolett.6b00974>.
- [68] Jonathan C. Lee et al. "Fabrication of thin diamond membranes for photonic applications". In: *Diamond and Related Materials* 33 (2013), pp. 45–48. ISSN: 09259635. DOI: 10.1016/j.diamond.2012.12.008. arXiv: 1210.0125. URL: <http://dx.doi.org/10.1016/j.diamond.2012.12.008>.
- [69] Jingyuan Linda Zhang et al. "Strongly Cavity-Enhanced Spontaneous Emission from Silicon-Vacancy Centers in Diamond". In: *Nano Letters* 18.2 (2018), pp. 1360–1365. ISSN: 1530-6984. DOI: 10.1021/acs.nanolett.7b05075. arXiv: 1708.05771. URL: <http://pubs.acs.org/doi/10.1021/acs.nanolett.7b05075>.
- [70] Thomas M. Babinec et al. "A diamond nanowire single-photon source". In: *Nature Nanotechnology* 5.3 (2010), pp. 195–199. ISSN: 17483395. DOI: 10.1038/nnano.2010.6. arXiv: 0908.0233.
- [71] E Neu et al. "Photonic nano-structures on (111)-oriented diamond". In: *Applied Physics Letters* 104.15 (2014), p. 4. DOI: 10.1063/1.4871580.
- [72] Haig A. Atikian et al. "Freestanding nanostructures via reactive ion beam angled etching". In: *APL Photonics* 2.5 (2017), p. 051301. ISSN: 2378-0967. DOI:

- 10.1063/1.4982603. URL: <http://aip.scitation.org/doi/10.1063/1.4982603>.
- [73] Sara Mouradian et al. "Rectangular photonic crystal nanobeam cavities in bulk diamond". In: *Applied Physics Letters* 111.2 (2017). ISSN: 00036951. DOI: 10.1063/1.4992118. arXiv: 1704.07918.
- [74] Noel H. Wan, Sara Mouradian, and Dirk Englund. "Two-dimensional photonic crystal slab nanocavities on bulk single-crystal diamond". In: *Applied Physics Letters* 112.14 (2018). ISSN: 00036951. DOI: 10.1063/1.5021349. arXiv: 1801.01151.
- [75] T. M. Babinec et al. "Design and focused ion beam fabrication of single crystal diamond nanobeam cavities". In: *Journal of Vacuum Science & Technology B* 29.010601 (2010), pp. 1–6. ISSN: 10711023. DOI: 10.1116/1.3520638. arXiv: 1008.1431. URL: <http://arxiv.org/abs/1008.1431>.
- [76] Barbara A. Fairchild et al. "Fabrication of ultrathin single-crystal diamond membranes". In: *Advanced Materials* 20.24 (2008), pp. 4793–4798. ISSN: 09359648. DOI: 10.1002/adma.200801460. arXiv: arXiv:0809.2133.
- [77] N. R. Parikh et al. "Single-crystal diamond plate liftoff achieved by ion implantation and subsequent annealing". In: *Applied Physics Letters* 61.26 (1992), pp. 3124–3126. ISSN: 00036951. DOI: 10.1063/1.107981.
- [78] Paul Hill et al. "Thin film diamond membranes bonded on-demand with SOI ring resonators". In: *Diamond and Related Materials* 88 (2018), pp. 215–221. ISSN: 09259635. DOI: 10.1016/j.diamond.2018.07.020. URL: <https://linkinghub.elsevier.com/retrieve/pii/S0925963518301900>.
- [79] Birgit J M Hausmann et al. "Integrated diamond networks for quantum nanophotonics." In: *Nano letters* 12.3 (2012), pp. 1578–82. ISSN: 1530-6992.

- DOI: 10 . 1021 / n1204449n. URL:
<http://www.ncbi.nlm.nih.gov/pubmed/22339606>.
- [80] Afaq H. Piracha et al. "Scalable Fabrication of Integrated Nanophotonic Circuits on Arrays of Thin Single Crystal Diamond Membrane Windows". In: *Nano Letters* 16.5 (2016), pp. 3341–3347. ISSN: 15306992. DOI: 10.1021/acs.nanolett.6b00974.
- [81] P. Ovarthaiyapong et al. "High quality factor single-crystal diamond mechanical resonators". In: *Applied Physics Letters* 101.16 (2012). ISSN: 00036951. DOI: 10.1063/1.4760274. arXiv: 1206.4363.
- [82] Pawel Latawiec et al. "On-Chip Diamond Raman Laser". In: ().
- [83] Othman H. Y. Zalloum et al. "On femtosecond micromachining of HPHT single-crystal diamond with direct laser writing using tight focusing". In: *Optics Express* 18.12 (2010), p. 13122. ISSN: 1094-4087. DOI: 10.1364/OE.18.013122. URL: <https://www.osapublishing.org/oe/abstract.cfm?uri=oe-18-12-13122>.
- [84] Afaq Habib Piracha et al. "Scalable fabrication of high-quality, ultra-thin single crystal diamond membrane windows". In: *Nanoscale* 8.12 (2016), pp. 6860–6865. ISSN: 2040-3364. DOI: 10 . 1039 / C5NR08348F. URL: <http://xlink.rsc.org/?DOI=C5NR08348F>.
- [85] Fei Gao et al. "Low-Loss Millimeter-Length Waveguides and Grating Couplers in Single-Crystal Diamond". In: *Journal of Lightwave Technology* 34.23 (2016), pp. 5576–5582. ISSN: 0733-8724. DOI: 10 . 1109 / JLT . 2016 . 2622620. URL: <http://ieeexplore.ieee.org/document/7725557/>.
- [86] Oxford Instruments. *Inductively Coupled Plasma Etching (ICP) - Oxford Instruments*. URL:

- <https://plasma.oxinst.com/campaigns/technology/icp-etching>
(visited on 11/19/2018).
- [87] C. L. Lee et al. "Etching and micro-optics fabrication in diamond using chlorine-based inductively-coupled plasma". In: *Diamond and Related Materials* 17.7-10 (2008), pp. 1292–1296. ISSN: 09259635. DOI: [10.1016/j.diamond.2008.01.011](https://doi.org/10.1016/j.diamond.2008.01.011).
- [88] C. L. Lee, M. D. Dawson, and E. Gu. "Diamond double-sided micro-lenses and reflection gratings". In: *Optical Materials* 32.9 (2010), pp. 1123–1129. ISSN: 09253467. DOI: [10.1016/j.optmat.2010.03.013](https://doi.org/10.1016/j.optmat.2010.03.013). URL: <http://dx.doi.org/10.1016/j.optmat.2010.03.013>.
- [89] Fabio L. Leite et al. *Theoretical models for surface forces and adhesion and their measurement using atomic force microscopy*. Vol. 13. 10. 2012, pp. 12773–12856. ISBN: 5501532295902. DOI: [10.3390/ijms131012773](https://doi.org/10.3390/ijms131012773).
- [90] Veeco Instruments. "WYKO NT1100 Setup Guide". In: April (2007).
- [91] Centre of Micronanotechnology. *CMI - Center of MicroNanoTechnology*. 2010. URL: https://cmi.epfl.ch/metrology/Wyko{_}NT1100.php (visited on 10/10/2018).
- [92] A. Bruker Wise. "Measuring transparent films with Optical profilers". In: URL: https://nanobioelectronics.weebly.com/uploads/3/8/8/6/38862535/measuring{_}transparent{_}films{_}with{_}bruker{_}optical{_}profilers{_}-{_}may{_}17{_}2016.pdf.
- [93] Akiko Harasaki and James C. Wyant. "Fringe modulation skewing effect in white-light vertical scanning interferometry". In: *Applied Optics* 39.13 (2000), p. 2101. ISSN: 0003-6935. DOI: [10.1364/AO.39.002101](https://doi.org/10.1364/AO.39.002101). URL: <https://www.osapublishing.org/abstract.cfm?URI=ao-39-13-2101>.

- [94] Akiko Harasaki, Joanna Schmit, and James C. Wyant. "Improved vertical-scanning interferometry". In: *Applied Optics* 39.13 (2000), p. 2107. ISSN: 01406736. DOI: [10 . 1016 / S0140 - 6736\(00 \) 56925 - 6](https://doi.org/10.1016/S0140-6736(00)56925-6). URL: <https://www.osapublishing.org/abstract.cfm?URI=ao-39-13-2107>.
- [95] F. P. Payne and J. P R Lacey. "A theoretical analysis of scattering loss from planar optical waveguides". In: *Optical and Quantum Electronics* 26.10 (1994), pp. 977–986. ISSN: 03068919. DOI: [10.1007/BF00708339](https://doi.org/10.1007/BF00708339).
- [96] Binke Huang, Juan Chen, and Wanshun Jiang. "Effects of Surface Roughness on TE Modes in Rectangular Waveguide". In: *Journal of Infrared, Millimeter, and Terahertz Waves* 30.7 (2009), pp. 717–726. ISSN: 1866-6892. DOI: [10.1007/s10762-009-9488-4](https://doi.org/10.1007/s10762-009-9488-4). URL: <http://link.springer.com/10.1007/s10762-009-9488-4>.
- [97] Tymon Barwicz and Hermann A. Haus. "Three-dimensional analysis of scattering losses due to sidewall roughness in microphotonic waveguides". In: *Journal of Lightwave Technology* 23.9 (2005), pp. 2719–2732. ISSN: 07338724. DOI: [10.1109/JLT.2005.850816](https://doi.org/10.1109/JLT.2005.850816).
- [98] K. Kendall. "Adhesion: Molecules and Mechanics". In: *Science* 263.5154 (1994), pp. 1720–1725. ISSN: 0036-8075. DOI: [10 . 1126 / science . 263 . 5154 . 1720](https://doi.org/10.1126/science.263.5154.1720). URL: <http://www.sciencemag.org/cgi/doi/10.1126/science.263.5154.1720>.
- [99] V Adrian Parsegian. *Van der Waals Forces*. January. Cambridge: Cambridge University Press, 2005. ISBN: 9780511614606. DOI: [10 . 1017 / CB09780511614606](https://doi.org/10.1017/CB09780511614606). URL: <http://ebooks.cambridge.org/ref/id/CB09780511614606>.
- [100] Jacob N. Israelachvili. *Intermolecular and Surface Forces: Third Edition*. 2011, pp. 1–676. ISBN: 9780123919274. DOI: [10 . 1016 / C2011 - 0 - 05119 - 0](https://doi.org/10.1016/C2011-0-05119-0). arXiv: [arXiv:1011.1669v3](https://arxiv.org/abs/1011.1669v3).

- [101] Hydrogen Bond, Van Der Waals, and Der Waals. "Intermolecular and Surface Forces 2.1.1 Overview: Types of Surface Forces". In: (), pp. 1–18.
- [102] Gregorio W. *File:AFM schematic (EN).svg*. 2011. URL: [https://commons.wikimedia.org/wiki/File:AFM{_}schematic{_}\(EN\).svg](https://commons.wikimedia.org/wiki/File:AFM{_}schematic{_}(EN).svg).
- [103] Ye Tao and Christian Degen. "Facile fabrication of single-crystal-diamond nanostructures with ultrahigh aspect ratio". In: *Advanced Materials* 25.29 (2013), pp. 3962–3967. ISSN: 09359648. DOI: [10.1002/adma.201301343](https://doi.org/10.1002/adma.201301343).
- [104] Alp Sipahigil et al. "An integrated diamond nanophotonics platform for quantum-optical networks". In: *Science* 354.6314 (2016), pp. 847–850. ISSN: 0036-8075. DOI: [10.1126/science.aah6875](https://doi.org/10.1126/science.aah6875). arXiv: [1608.05147](https://arxiv.org/abs/1608.05147). URL: https://www.osapublishing.org/abstract.cfm?URI=CLEO{_}QELS-2017-FTh3H. [4http://www.sciencemag.org/lookup/doi/10.1126/science.aah6875](http://www.sciencemag.org/lookup/doi/10.1126/science.aah6875).
- [105] Luozhou Li et al. "Efficient photon collection from a nitrogen vacancy center in a circular bullseye grating". In: *Nano Letters* 15.3 (2015), pp. 1493–1497. ISSN: 15306992. DOI: [10.1021/nl503451j](https://doi.org/10.1021/nl503451j). arXiv: [1409.3068](https://arxiv.org/abs/1409.3068).
- [106] Michael J. Burek et al. "Free-standing mechanical and photonic nanostructures in single-crystal diamond". In: *Nano Letters* 12.12 (2012), pp. 6084–6089. ISSN: 15306984. DOI: [10.1021/nl302541e](https://doi.org/10.1021/nl302541e).
- [107] Charalambos Klitis et al. "High-extinction-ratio TE/TM selective Bragg grating filters on silicon-on-insulator". In: *Optics Letters* 42.15 (2017), p. 3040. ISSN: 0146-9592. DOI: [10.1364/OL.42.003040](https://doi.org/10.1364/OL.42.003040). URL: <https://www.osapublishing.org/abstract.cfm?URI=ol-42-15-3040>.
- [108] W. Bogaerts et al. "Silicon microring resonators". In: *Laser & Photonics Reviews* 6.1 (2012), pp. 47–73. ISSN: 18638880. DOI: [10.1002/lpor.201100017](https://doi.org/10.1002/lpor.201100017). arXiv: [arXiv : 1208.0765v1](https://arxiv.org/abs/1208.0765v1). URL: <http://doi.wiley.com/10.1002/lpor.201100017>.

- [109] Michael J. Strain et al. "Tunable Q-factor silicon microring resonators for ultra-low power parametric processes". In: *Optics Letters* 40.7 (2015), p. 1274. ISSN: 0146-9592. DOI: 10.1364/OL.40.001274. URL: <https://www.osapublishing.org/abstract.cfm?URI=ol-40-7-1274>.
- [110] Lumerical Inc. *MODE Solutions*. URL: <http://www.lumerical.com/tcad-products/mode/>.
- [111] Valentin L Popov. "Contact mechanics and friction". In: *Metal Machining*. Elsevier, 2000, pp. 363–374. ISBN: 978-3-662-53080-1. DOI: 10.1016/B978-0-08-052402-3.50015-0. arXiv: arXiv:1011.1669v3. URL: <http://linkinghub.elsevier.com/retrieve/pii/B9780080524023500150>.
- [112] Wikipedia. *Newton's rings*. 2019. URL: https://en.wikipedia.org/wiki/Newton's_rings (visited on 03/11/2019).
- [113] Sam Johnson, Philip R Dolan, and Jason M Smith. "Diamond photonics for distributed quantum networks". In: *Progress in Quantum Electronics* 55 (2017), pp. 129–165. ISSN: 00796727. DOI: 10.1016/j.pquantelec.2017.05.003. URL: <https://linkinghub.elsevier.com/retrieve/pii/S0079672717300162>.
- [114] Michael Gould et al. "Large-scale GaP-on-diamond integrated photonics platform for NV center-based quantum information". In: *Journal of the Optical Society of America B* 33.3 (2016), B35. ISSN: 0740-3224. DOI: 10.1364/JOSAB.33.000B35. URL: <https://www.osapublishing.org/abstract.cfm?URI=josab-33-3-B35>.
- [115] M. V. Hauf et al. "Chemical control of the charge state of nitrogen-vacancy centers in diamond". In: *Physical Review B* 83.8 (2011), p. 081304. ISSN: 1098-0121. DOI: 10.1103/PhysRevB.83.081304. URL: <https://link.aps.org/doi/10.1103/PhysRevB.83.081304>.

- [116] Michael Barth et al. "Modification of visible spontaneous emission with silicon nitride photonic crystal nanocavities". In: *Optics Express* 15.25 (2007), p. 17231. ISSN: 1094-4087. DOI: 10.1364/OE.15.017231. URL: <http://www.opticsexpress.org/abstract.cfm?URI=oe-15-25-17231>
<http://www.opticsinfobase.org/abstract.cfm?URI=oe-15-25-17231>
<https://www.osapublishing.org/oe/abstract.cfm?uri=oe-15-25-17231>
- [117] K Rae et al. "InGaN micro-LEDs integrated onto an ultra-thin, colloidal quantum dot functionalized glass platform". In: *Optics Express* 25.16 (2017), pp. 19179–19184. ISSN: 1094-4087. DOI: 10.15129/28b1e9db-91f4-4787-9ef3-522401895239.
- [118] Dimitars Jevtics et al. "Integration of Semiconductor Nanowire Lasers with Polymeric Waveguide Devices on a Mechanically Flexible Substrate". In: *Nano Letters* 17.10 (2017), pp. 5990–5994. ISSN: 15306992. DOI: 10.1021/acs.nanolett.7b02178.
- [119] Jongseung Yoon et al. "Heterogeneously Integrated Optoelectronic Devices Enabled by Micro-Transfer Printing". In: *Advanced Optical Materials* 3.10 (2015), pp. 1313–1335. ISSN: 21951071. DOI: 10.1002/adom.201500365.
- [120] B. Guilhabert et al. "Hybrid integration of an evanescently coupled AlGaAs microdisk resonator with a silicon waveguide by nanoscale-accuracy transfer printing". In: *Optics Letters* 43.20 (2018), p. 4883. ISSN: 0146-9592. DOI: 10.1364/OL.43.004883. URL: <https://www.osapublishing.org/abstract.cfm?URI=ol-43-20-4883>.

- [121] John McPhillimy et al. "High accuracy transfer printing of single-mode membrane silicon photonic devices". In: *Optics Express* 26.13 (2018), pp. 297–300. ISSN: 10944087. DOI: [10.1364/OE.26.016679](https://doi.org/10.1364/OE.26.016679).
- [122] Jan Niehusmann et al. "Ultrahigh-quality-factor silicon-on-insulator microring resonator". In: *Optics Letters* 29.24 (2004), p. 2861. ISSN: 0146-9592. DOI: [10.1364/OL.29.002861](https://doi.org/10.1364/OL.29.002861). URL: <https://www.osapublishing.org/abstract.cfm?URI=ol-29-24-2861>.
- [123] B. E. Little et al. "Very high-order microring resonator filters the WDM applications". In: *IEEE Photonics Technology Letters* 16.10 (2004), pp. 2263–2265. ISSN: 10411135. DOI: [10.1109/LPT.2004.834525](https://doi.org/10.1109/LPT.2004.834525).
- [124] V. Van et al. "All-optical nonlinear switching in GaAs-AlGaAs microring resonators". In: *IEEE Photonics Technology Letters* 14.1 (2002), pp. 74–76. ISSN: 1041-1135. DOI: [10.1109/68.974166](https://doi.org/10.1109/68.974166). URL: <http://ieeexplore.ieee.org/document/974166/>.
- [125] Joyce K. Poon et al. "Transmission and group delay of microring coupled-resonator optical waveguides". In: *Optics Letters* 31.4 (2006), p. 456. ISSN: 0146-9592. DOI: [10.1364/ol.31.000456](https://doi.org/10.1364/ol.31.000456).
- [126] Katrien De Vos et al. "Silicon-on-Insulator microring resonator for sensitive and label-free biosensing". In: *Optics Express* 15.12 (2007), p. 7610. ISSN: 1094-4087. DOI: [10.1364/OE.15.007610](https://doi.org/10.1364/OE.15.007610). arXiv: [arXiv:1011.1669v3](https://arxiv.org/abs/1011.1669v3). URL: <https://www.osapublishing.org/oe/abstract.cfm?uri=oe-15-12-7610>.
- [127] S.M. Chakkalakkal Abdulla et al. "Mechanical tuning of optical race-track ring resonators". In: *Procedia Engineering* 5.October 2015 (2010), pp. 424–427. ISSN: 18777058. DOI: [10.1016/j.proeng.2010.09.137](https://doi.org/10.1016/j.proeng.2010.09.137). URL: <http://dx.doi.org/10.1016/j.proeng.2010.09.137><https://linkinghub.elsevier.com/retrieve/pii/S1877705810006843>.

- [128] Janine Riedrich-Möller et al. "One- and two-dimensional photonic crystal microcavities in single crystal diamond". In: *Nature Nanotechnology* 7.1 (2011), pp. 69–74. ISSN: 1748-3387. DOI: [10.1038/nnano.2011.190](https://doi.org/10.1038/nnano.2011.190). arXiv: [1109.4595](https://arxiv.org/abs/1109.4595). URL: <http://www.ncbi.nlm.nih.gov/pubmed/22081214>.
- [129] B. J M Hausmann et al. "Coupling of NV centers to photonic crystal nanobeams in diamond". In: *Nano Letters* 13.12 (2013), pp. 5791–5796. ISSN: 15306984. DOI: [10.1021/nl402174g](https://doi.org/10.1021/nl402174g).
- [130] S. Mosor et al. "Scanning a photonic crystal slab nanocavity by condensation of xenon". In: *Applied Physics Letters* 87.14 (2005), p. 141105. ISSN: 0003-6951. DOI: [10.1063/1.2076435](https://doi.org/10.1063/1.2076435). URL: <http://aip.scitation.org/doi/10.1063/1.2076435>.
- [131] Milos Nedeljkovic, Richard Soref, and Goran Z. Mashanovich. "Predictions of free-carrier electroabsorption and electrorefraction in germanium". In: *IEEE Photonics Journal* 7.3 (2015), pp. 1–14. ISSN: 19430655. DOI: [10.1109/JPHOT.2015.2419217](https://doi.org/10.1109/JPHOT.2015.2419217).
- [132] Charlie Ironside. "Linear electro-optic effect, electroabsorption and electrorefraction". In: *Semiconductor Integrated Optics for Switching Light*. IOP Publishing, 2017. ISBN: 9781681745213. DOI: [10.1088/978-1-6817-4521-3ch2](https://doi.org/10.1088/978-1-6817-4521-3ch2). URL: <http://iopscience.iop.org/book/978-1-6817-4521-3/chapter/bk978-1-6817-4521-3ch2>.
- [133] Parag B. Deotare et al. "Coupled photonic crystal nanobeam cavities". In: *Applied Physics Letters* 95.3 (2009). ISSN: 00036951. DOI: [10.1063/1.3176442](https://doi.org/10.1063/1.3176442).
- [134] Fook Siong Chau et al. "Dynamic tuning of an optical resonator through MEMS-driven coupled photonic crystal nanocavities". In: *Optics Letters* 35.15 (2010), p. 2517. ISSN: 0146-9592. DOI: [10.1364/ol.35.002517](https://doi.org/10.1364/ol.35.002517).

- [135] F. Mohd-Yasin, D. J. Nagel, and C. E. Korman. "Noise in MEMS". In: *Measurement Science and Technology* 21.1 (2010), p. 012001. ISSN: 0957-0233. DOI: [10 . 1088 / 0957 - 0233 / 21 / 1 / 012001](https://doi.org/10.1088/0957-0233/21/1/012001). URL: <http://stacks.iop.org/0957-0233/21/i=1/a=012001?key=crossref.4b085f5ce744d7f10d787b941dbb2be1>.
- [136] Bradley J Frey, Douglas B Leviton, and Timothy J Madison. "Temperature-dependent refractive index of silicon and germanium". In: ed. by Eli Atad-Ettedgui, Joseph Antebi, and Dietrich Lemke. 2006, 62732J. DOI: [10 . 1117 / 12 . 672850](https://doi.org/10.1117/12.672850). URL: [http : / / proceedings . spiedigitallibrary.org/proceeding.aspx?doi=10.1117/12.672850](http://proceedings.spiedigitallibrary.org/proceeding.aspx?doi=10.1117/12.672850).
- [137] Karlo David Alves Sabóia et al. "Optical Bistability in an Acousto-Optic Tunable Filter (AOTF) Operating with Short Optical Pulses". In: *Journal of Electromagnetic Analysis and Applications* 04.03 (2012), pp. 112–117. ISSN: 1942-0730. DOI: [10.4236/jemaa.2012.43015](https://doi.org/10.4236/jemaa.2012.43015).
- [138] Hyat M. Gibbs. *Optical Bistability*. Ed. by Paul F. Liao and Paul Kelley. 1st. Academic Press Inc., 1985, pp. 1–5. ISBN: 0-12-281940-3.
- [139] Ian Friel et al. "Development of high quality single crystal diamond for novel laser applications". In: *Optics and Photonics for Counterterrorism and Crime Fighting VI and Optical Materials in Defence Systems Technology VII* 7838 (2010), p. 783819. DOI: [10.1117/12.864981](https://doi.org/10.1117/12.864981).
- [140] Vasili G. Savitski, Sean Reilly, and Alan J. Kemp. "Steady-state raman gain in diamond as a function of pump wavelength". In: *IEEE Journal of Quantum Electronics* 49.2 (2013), pp. 218–223. ISSN: 00189197. DOI: [10.1109/JQE.2012.2237505](https://doi.org/10.1109/JQE.2012.2237505).
- [141] Vilson R. Almeida and Michal Lipson. "Optical bistability on a silicon chip". In: *Optics Letters* 29.20 (2004), p. 2387. ISSN: 0146-9592. DOI: [10.1364/ol.29.002387](https://doi.org/10.1364/ol.29.002387).

- [142] Vilson R. Almeida et al. "All-optical control of light on a silicon chip". In: *Nature* 431.7012 (2004), pp. 1081–1084. ISSN: 00280836. DOI: [10.1038/nature02921](https://doi.org/10.1038/nature02921).
- [143] K. M C Fu et al. "Coupling of nitrogen-vacancy centers in diamond to a GaP waveguide". In: *Applied Physics Letters* 93.23 (2008), pp. 3–5. ISSN: 00036951. DOI: [10.1063/1.3045950](https://doi.org/10.1063/1.3045950). arXiv: [0811.0328](https://arxiv.org/abs/0811.0328).
- [144] R. W. Purnamaningsih et al. "Design of GaN based optical modulator with mach-zehnder interferometer structure". In: *WSEAS Transactions on Communications* 13 (2014), pp. 229–233. ISSN: 22242864.
- [145] X.-C. Long et al. "GaN linear electro-optic effect". In: *Applied Physics Letters* 67.10 (1995), pp. 1349–1351. ISSN: 0003-6951. DOI: [10.1063/1.115547](https://doi.org/10.1063/1.115547). URL: <http://aip.scitation.org/doi/10.1063/1.115547>.
- [146] C. J. Stephen et al. "Three-dimensional solid-state qubit arrays with long-lived spin coherence". In: (2018), pp. 2–9. arXiv: [1807.03643](https://arxiv.org/abs/1807.03643). URL: <http://arxiv.org/abs/1807.03643>.

List of Publications

July 2018

Three-dimensional solid-state qubit arrays with long-lived spin coherence

Working paper

Micro-assembly of hybrid diamond-Si resonator devices

Int. Photonics Research, Silicon, & Nano-Photonics - Zurich, Switzerland

Hybridisation of diamond with silicon photonic resonators

De Beers Diamond Conference

Sept 2018

Thin film diamond membranes bonded on-demand with SOI ring resonators

Diamond and Related Materials

April 2019

Thermally tuneable integrated diamond micro-disk resonators by micro-assembly

Symposium Latsis 2019: Diamond Photonics - EPFL, Lausanne, Switzerland